Stacking it up:

Exploring the limits of ultra-high resolution atomic force microscopy

Cover design by Jelmer Feenstra, 3D-view made from a constant height AFM image of a TOAT molecule on Cu(111).

ISBN: 978-94-6295-678-0

Stacking it up:

Exploring the limits of ultra-high resolution atomic force microscopy

Opstapelen:

Verkenning van de grenzen van ultra hoge resolutie atomaire kracht microscopie

(met samenvatting in het Nederlands)

Proefschrift

ter verkrijging van de graad van doctor aan de Universiteit Utrecht op gezag van de rector magnificus, prof.dr. G.J. van der Zwaan, ingevolge het besluit van het college voor promoties in het openbaar te verdedigen op woensdag 13 september 2017 des middags te 12.45 uur door

Nadine Jacoba van der Heijden

geboren op 9 juli 1989 te Delft

Promotor: Prof. dr. D.A.M. Vanmaekelbergh

Copromotor: Dr. I. Swart

Dit proefschrift werd (mede) mogelijk gemaakt met financiële steun van de Nederlandse Organisatie voor Wetenschappelijk Onderzoek (ECHO-Stip nr.717.013.003).

Table of contents

1. Introduction **9**
1.1 Introduction 10
1.2 Outline of this thesis 10
1.3 References 11

2. Imaging the chemical structure of molecules at low temperatures with non-contact atomic force microscopy **13**
2.1 Introduction 14
2.2 Physical principles of atomic force microscopy 17
2.3 Imaging single molecules and chemical reactions 23
2.4 Tip termination 28
2.5 Discussion on interpretation 34
2.6 Adding a third dimension 41
2.7 References 45

3. Intermolecular contrast in AFM images without intermolecular bonds **51**
3.1 Introduction 52
3.2 Experimental method 53
3.3 Experimental results and DFT simulations 53
3.4 Contrast in regions between molecules 55
3.5 Molecular mechanics simulations 55
3.6 Height dependence of apparent bonds 58
3.7 Conclusion 60
3.8 References 60

4. Mapping the electrostatic force field of single molecules from high-resolution scanning probe images **65**
4.1 Introduction 66
4.2 General considerations 67
4.3 Methods 73
4.4 Results 79
4.5 Discussion 83
4.6 Conclusion 84
4.7 References 85

5. Recognizing nitrogen dopant atoms in graphene using AFM **91**
5.1 Introduction 92
5.2 Methods 93
5.3 Results and discussion 95
5.4 Conclusion 107
5.5 References 108

6. Characteristic contrast in Δf_{min} maps of organic molecules using AFM **113**
6.1 Introduction 114
6.2 Methods 115
6.3 Results and discussion 118
6.4 Conclusion 128
6.5 References 129

7. Adsorption geometry of single molecules on Cu(111) resolved with submolecular resolution using AFM **133**
7.1 Introduction 134
7.2 Methods 135
7.3 Results and discussion 136
7.4 Conclusion 141
7.5 References 141

Appendix **145**
Samenvatting in het Nederlands 146
Gearfetting yn it Frysk 149
List of presentations 152
List of publications 153
About the author 154
Acknowledgements 155

1

Introduction

abstract

This chapter will briefly introduce the theme of this thesis and highlight the topics of the following chapters.

based on

written for this thesis (2017)

1.1 Introduction

Atomic force microscopy (AFM) is a technique wherein an atomically sharp needle raster scans across a surface, detecting forces between it and the sample. In state-of-the-art AFM experiments the measured forces are typically on the order of pico-Newtons, and the lateral resolution is on the order of pico-meters. This enables sub-molecular resolution imaging of single molecules and atomic resolution on surfaces.[1–4] The push for smaller and smaller electronic devices as well as the need for better catalysts for the chemical industry necessitates a better understanding of molecules and surfaces on the atomic scale. AFM is uniquely equipped to face these challenges and this thesis provides new insights in the scope of questions that AFM can help answer.

The title of this thesis *'Stacking it up: Exploring the limits of ultra-high resolution atomic force microscopy'* mentions stacks because three-dimensional data can be referred to as a data-stack, and in this thesis the impact of 3D data is exploited in every chapter.

This thesis describes our efforts to explore the limits of the technique and to extend the boundaries of what can be measured.

1.2 Outline of this thesis

A short summary of each chapter is given below.

Chapter 2 gives a detailed background on the development and theory behind high resolution AFM. It focusses primarily on molecules on atomically flat surfaces and highlights recent accomplishments as well as current topics of debate.

Chapter 3 is about intermolecular features in AFM images of organic molecules. In the literature, these have been ascribed to intermolecular bonds,[5] In this chapter it is demonstrated that intermolecular contrast cannot be directly interpreted as intermolecular bonds.

Chapter 4 of this thesis will go into more detail about the origin of image distortions and the influence of electrostatic charges on the apparent position and size of features. In addition it outlines a method for measuring the electrostatic field over a molecule with sub-molecular resolution.

Chapter 5 shows that the position of the nitrogen dopant atoms in grapheme can be determined using AFM. Specifically, the frequency shift–distance curves $\Delta f(z)$ acquired above a nitrogen atom are significantly different from the curves measured over a carbon atom.

Chapter 6 illustrates how the technique of analyzing and comparing $\Delta f_{min}(x,y)$ and $z_{min}(x,y)$ maps from chapter 5 can be applied to single molecules to establish chemical recognition of organic molecules.

Chapter 7 delves into the geometry of molecule adsorption at a flat substrate, information that can be obtained from high-resolution AFM with pico-meter accuracy, also using $z_{min}(x,y)$ maps. In addition, the influence of adsorption on the dipole moment of a molecules is investigated.

1.3 References

[1] G. Binnig, C. F. Quate, Atomic Force Microscope. *Phys. Rev. Lett.* **56**, 930–933 (1986).
[2] G. Binnig, C. Gerber, T. R. Albrecht, C. F. Quate, Atomic Resolution with Atomic Force Microscope. *Europhys. Lett.* **3**, 1281–1286 (1987).
[3] F. J. Giessibl, Atomic resolution on Si(111)-(7×7) by noncontact atomic force microscopy with a force sensor based on a quartz tuning fork. *Appl. Phys. Lett.* **76**, 1470–1472 (2000).
[4] L. Gross, F. Mohn, N. Moll, P. Liljeroth, G. Meyer, The Chemical Structure of a Molecule Resolved by Atomic Force Microscopy. *Science.* **325**, 1110–1114 (2009).
[5] J. Zhang, P. Chen, B. Yuan, W. Ji, Z. Cheng, X. Qiu, Real-Space Identification of Intermolecular Bonding with Atomic Force Microscopy. *Science.* **342**, 611–614 (2013).

2

Imaging the chemical structure of molecules at low temperatures with non-contact atomic force microscopy

abstract

In this chapter, the development and recent advances in the field of frequency modulated non-contact atomic force microscopy (AFM) of molecules on surfaces are reviewed. In addition, the applications of AFM in chemical science and the current challenges are discussed.

based on

written for this thesis (2017)

2.1 Introduction

In this chapter we will have a close look at atomic force microscopy (AFM). AFM is at the center of this thesis, therefore some history and theory is pertinent. Specifically this chapter will sketch the current status, capabilities and ongoing discussions surrounding AFM of single molecules. For a broad overview of AFM and related scanning probe advances more encompassing reviews are available.[1–5]

2.1.1 Scanning probe microscopy

Scanning probe microscopy (SPM) is a collective name for a variety of techniques that venture into the realm of the really tiny, not by classical magnification, but by scanning surfaces with a probe. This probe raster-scans over a surface, gathering information regarding force, electric charge, conductivity, or other physical quantity. To enhance the resolution of SPM images one has to increase the pixel density, or change the diameter or sensitivity of the probe. Properties that bind all SPM techniques together under the same name are: a (sharp) probe, a sample surface to be investigated, finely calibrated actuators to precisely move the probe, and vibration isolation from surroundings. Additionally: in most cases the magnitude of the observed quantity strongly depends on the distance between the probe and the surface.

Atomic force microscopy is a type of SPM technique; a small probe, or needle, scans across the surface of the sample under investigation. Like the name suggests, AFM is sensitive to the physical quantity 'force'. The details on the nature of the force and how minute forces between sample and needle can be detected with sub-molecular resolution is the topic of the rest of this chapter.

Another SPM technique that is mentioned often in this thesis is scanning tunneling microscopy (STM). STM and AFM can be performed with the same probe and sample, and simultaneously. By combining data from both techniques a more comprehensive picture of the system under investigation is obtained, as well as the ease and speed of STM make it a suitable companion to AFM.

2.1.2 Development of AFM

Atomic force microscopy was conceived by Binnig *et al.* in 1985.[6] The central idea on

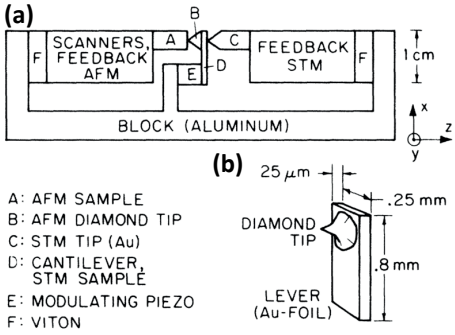

Figure 2.1 (a) Experimental setup of the first AFM by Binnig *et al.* The cantilever is not drawn to scale. **(b)** Dimensions of the cantilever. The STM and AFM piezoelectric drives are facing each other, sandwiching the diamond tip that is glued to the cantilever.[6]

how to detect a force between a sample and a probe is an extension to the STM, which Binnig *et al.* developed a few years earlier in 1982.[7] For their invention of the STM Binnig and Rohrer received the 1986 Nobel Prize in Physics.

The working principle of the STM, as an SPM technique, is to raster-scan a needle across a surface and measure the tunneling current between the sample and the tip of the needle. This tunneling current I is strongly dependent on the distance between tip and sample d: $I \propto e^{-2\kappa d}$, where κ is typically 1 $Å^{-1}$. Therefore the height of the tip can be recorded as a function of position, while an electronic feedback loop keeps the current constant. For high spatial resolution, both laterally and vertically, the movement of the tip needs to be controlled acately. Sub-atomic accuracy is not possible with mechanical motors, however by using piezo-electric actuators, Binnig *et al.* succeeded in building a probe table with actuators that could position and move the tip with sub-atomic precision, resulting in the first SPM.

Building on the idea of raster scanning a surface and combining this with the precision in height measurements resulting from STM measurements, Binnig *et al.* visualized a technique to measure ultra-small forces, on the order of 10^{-18} N. The idea of measuring forces by the displacement of a spring was already widely practiced, however with STM the dimensions of the detectable displacements decreased immensely, enabling the detection of ultra-small forces.

Thus the first AFM consisted of a cantilever that acted as a spring, with a small tip attached to its end-point, and an STM needle on top of the end of the cantilever to detect the displacement of the cantilever. The set-up, as described in the original paper, can

be seen in figure 2.1. After this initial successful demonstration of measuring forces, the methodology of AFM advanced, and its applications expanded.

New methods to detect the displacement of the cantilever were established. A laser beam is reflected on the top of the cantilever and the change in the position of the deflected laser spot on photo diodes is measured to indicate the displacement.[8,9] Another method to observe the deflection of the cantilever based on exploiting the piezo-electricity of a quartz crystal. Various designs exist that use a quartz cantilever, such as the KolibriSensor[10] and the qPlus sensor.[11] The qPlus sensor, which is used for the experiments in this thesis, is discussed in more detail later in this chapter.

The scanning techniques themselves have also continued to diversify and improve. Initially, AFM experiments were done in so-called contact mode. In this mode the deflection of a cantilever with a small spring constant k is recorded as a function of the lateral position.[6] Subsequently, dynamic modes were introduced. In dynamic AFM the cantilever is deliberately oscillated at a given frequency. Dynamic modes are divided in two branches; one where the amplitude of the oscillation is varied (amplitude modulation (AM) mode)[12] and a branch where the frequency of the oscillating cantilever is varied (frequency modulation (FM) mode).[13] The introduction of quartz cantilevers, which typically have a large spring constant k, enabled small amplitude oscillations. Small oscillation amplitudes are essential for high spatial resolution of short range forces.[11,14]

It is from this point onward that imaging molecules on surfaces with sub-molecular resolution was achieved.[15] This chapter will focus on describing further developments in this field of imaging single molecules with AFM. Starting by delving deeper into the physical mechanisms behind AFM, followed by a brief overview of possibilities in imaging single molecules and chemical reactions at the single molecule level. Subsequently we will discuss the various tip terminations that have been used, as well as their effect on the imaging contrast. Special attention will be given to imaging artifacts and the interpretation of images. Finally, the wide and increasing scope of the technique is illustrated by expanding into three dimensions.

2.2 Physical principles of atomic force microscopy

Measuring forces with springs at least dates back to Hooke's law from the 17th century. The mechanism of AFM can therefore be understood with classical mechanics, despite the fact that we are measuring forces, such as the Pauli repulsion, which originate in quantum mechanics. To first order, the response of a spring to a force is given by Hooke's law:

$$\vec{F} = k\vec{z} \tag{1}$$

where F is the force, k is the spring constant and z is the displacement.

In this section an overview of the physical principals is given to enable the reader to understand later discussions on interpretation and mechanisms behind AFM imaging. Other publications describe the principles of AFM and the derivations of the relations more thoroughly.[4,14,16–18]

2.2.1 Relations between force, frequency shift and energy

Starting with an intuitive understanding, the following paragraph will illustrate the relations between measurable quantities and physical and chemical properties.

Consider a tip oscillating with frequency f and amplitude A far away from any surface. When the needle is brought closer to the sample, any force between the tip and the sample will alter the oscillation cycle, thus the f, A and the phase θ might change. Since changes in frequencies can be determined with great accuracy, the detection limit for small forces is significantly decreased. In FM-AFM the amplitude is kept constant and the change in f, *i.e.* the frequency shift Δf, is measured.

By using a beam-shaped cantilever, which is stiff in the x- and y-direction and acts as a spring in the z-direction, we prevalently measure forces normal to the surface.

For an ideal spring the resonance frequency f_0 is given by

$$f_0 = \frac{1}{2\pi}\sqrt{\frac{k}{m}} \tag{2}$$

where k is the spring constant and m is the effective mass.

Consider the set-up depicted in figure 2.2, where a cantilever oscillates over a sample with amplitude A, at a height where the minimum tip-sample distance is d.

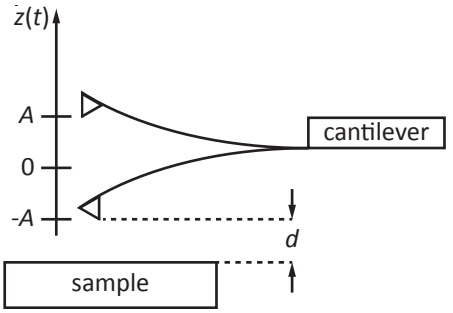

Figure 2.2 Schematic view of an oscillating cantilever at its upper and lower turnaround points. The minimum tip-sample distance is *d* and the amplitude is *A*.[4]

The oscillation of the cantilever can be expressed as

$$z(t) = A\ \cos(2\pi f t) \tag{3}$$

where z is the adapted height relative to the center of the oscillation and f is the oscillation frequency, $f = f_0$ at the resonance frequency. The equation of motion of this system is given by:

$$m\frac{d^2z}{dt^2} = -kz + F_{ts}(z) \tag{4}$$

The force between the tip and the sample (F_{ts}) appears in the equation of motion and can be interpreted as a frictional force. From equation (4) we can see that the oscillation frequency f will change such that $f = f_0 + \Delta f$. Giessibl[4] showed that for $|\Delta f| \ll f_0$ the frequency shift Δf is given by

$$\Delta f = -\frac{f_0}{kA^2}\langle F_{ts} z\rangle \tag{5}$$

where the brackets indicate the average over one oscillation cycle.

Now that we understand why and how the measured frequency shift (Δf) depends on the force between tip and sample (F_{ts}). Let's have a look at how to convert the measured quantity Δf back to force and even energy U.

Sader *et al.*[17] established a method to invert the expression for the relation between Δf and F_{ts}:

$$F(z) = 2k\int_z^\infty \left[\left(1 + \frac{A^{1/2}}{8\sqrt{\pi(t-z)}}\right)\frac{\Delta f(t)}{f_0} - \frac{A^{3/2}}{\sqrt{2(t-z)}}\frac{\Delta f(t)}{f_0}\frac{d}{dt}\right]dt \tag{6}$$

were t is an auxiliary variable in the same dimension as z. It enables the use of the entire $\Delta f(z)$ curve up to z to calculate $F(z)$. The use of t in this integral is inherent to

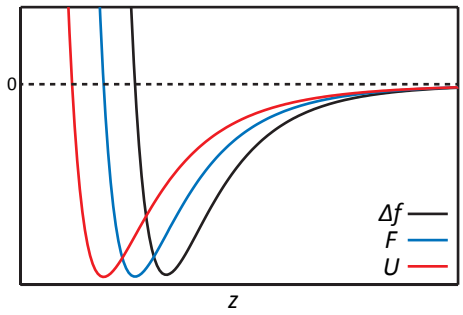

Figure 2.3 Qualitative relation between Δf (black), F (blue) and U (red) as a function of tip-sample distance z.

using the Riemann-Liouville integral.

By integration of $F(z)$ we find the potential energy U:

$$U(z) = 2k\int_z^\infty \frac{\Delta f(z)}{f_0}\left((t-z) + \frac{A^{1/2}}{4}\sqrt{\frac{t-z}{\pi}} + \frac{A^{3/2}}{\sqrt{2(t-z)}}\right)dt \tag{7}$$

A qualitative representation of the relation between Δf, F and U as a function of tip-sample distance z can be seen in figure 2.3. All graphs have the shape of a Lennard-Jones potential. This shape can be understood physically for all quantities.

The energy $U(z)$ represents the binding energy between the tip and the sample. At large distances, the interaction energy between tip and sample is zero. As the tip approaches the surface, the interaction increases until it reaches the minimum. If the distance is reduced even further, the electron clouds start to overlap and the energy strongly increases because of the Pauli exclusion principle.

At large distance there is no detectable force between the tip and the sample. When approaching the attractive van der Waals force appears, then when decreasing z, Pauli repulsion starts to contribute significantly, until it finally dominates $F(z)$ with a strong repulsion at small z.

Since Δf is proportional to the derivative of F it has the same shape again. Note that from U to F to Δf the curves move to larger z. In this thesis Δf will be the primary quantity used, as this is the quantity that can be measured directly. It should also be noted that for a reliable conversion between Δf, F and U, the amplitude A as well as the spring constant k of the tuning fork need to be known with some precision. Obtaining these values is experimentally challenging. However, for interpreting the images

and the underlying physical processes the conversion to F or U is not required. For comparison with theory (for example density functional theory (DFT) calculations) a conversion does have to be made between U and Δf.

2.2.2 The qPlus sensor

The amplitude A and spring constant k are two recurring variables in the translations between Δf and F. Considering we want to image molecules on surfaces with sub-molecular resolution it is reasonable to assume that the forces under investigation are primarily very short ranged such as the (difference in) Pauli repulsion over a molecule. To measure short range forces a small amplitude is preferable since a large part of the oscillation cycle can then be under influence of these short-range forces.[19] In addition, for measuring Pauli repulsion the tip needs to approach the sample at very small distances without irregularities in its oscillation cycle. Sudden snap-to-contact events to which experiments with small oscillation amplitudes are especially prone, prevent reliable FM-AFM measurements to be performed. The 'snap-to-contact' problem when using small amplitudes is alleviated by using very stiff cantilevers.

Due to its large spring constant, the so-called qPlus sensor provides a way to perform FM-AFM experiments with small amplitudes at small tip-sample distances. The qPlus sensor consists of a quartz tuning fork, of which one prong is attached to a holder and one prong is decorated with a tungsten or platinum iridium alloy needle that functions as a tip. An example of a qPlus sensor, as used for this thesis, can be seen in figure 2.4.

The quartz tuning fork has a spring constant k typically of 1800 N/m and a resonance frequency f_0 of 25 kHz when it is mounted to the holder.[20] The geometry of the tuning fork is such that the main resonance oscillation is in the z-direction and the amplitude can be tuned to be less than 1 Å.

The quality factor Q of the cantilever is defined as the energy stored in the oscillator divided by the energy needed to continue the oscillation at constant amplitude. Therefore Q is a measure for the amount of energy dissipated per oscillation cycle. For high Q (on the order of f_0) it is given by

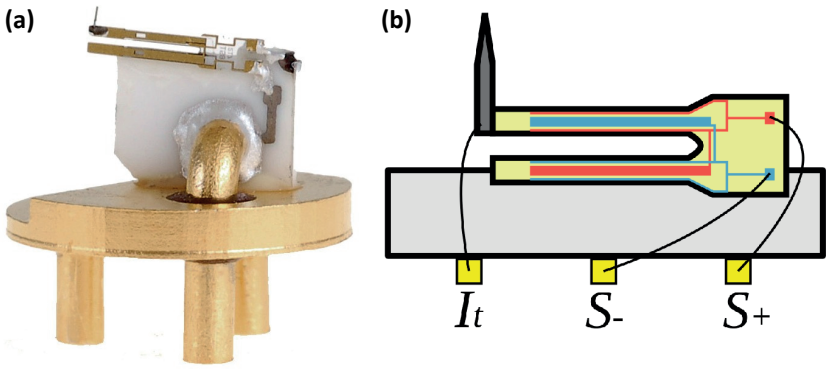

Figure 2.4 (a) Photo of a qPlus sensor. The gold-colored base has three legs to connect to electronic leads. The transparent quartz tuning fork at the top of the sensor can be seen mainly due to the golden electrodes running along the prongs. The needle that is used as the tip is glued to the upper prong. **(b)** Schematic representation of the quartz tuning fork, the electrodes that run along the prongs (blue and red) and the tunneling current wire, attached directly to the base of the needle.

$$Q = \frac{f_0}{f_{FWHM}} \tag{8}$$

Where f_{FWHM} is the full width half maximum of the resonant spectrum. At liquid helium temperature, in vacuum, Q for the qPlus sensors used in this thesis is typically higher than 20,000.

An additional advantage of using the qPlus sensor is that it enables all-electrical detection of the resonance frequency and amplitude. Quartz is a piezoelectric material, meaning that structural deformations, such as the prong oscillating when excited, cause a surface potential. This (change in) electric potential is measured by means of electrodes running along the sides and edges of the tuning fork (as depicted in figure 2.4b).

All electric detection along with measuring Δf instead of displacement directly make the qPlus sensor easy to operate and have a high precision. The all-electronic detection method, and the material of the needle (metal) also enable a smooth combination between STM and AFM within the same microscope, using the same sensor.

2.2.3 Regulation in practice

The all-electric detection of the frequency enables direct detection of the frequency shift. The tuning fork is excited by applying a small oscillating bias voltage to a piezo element in close proximity to the qPlus sensor. The signal from the tuning fork is amplified and then fed into a phase locked loop (PLL). The PLL compares the oscillation signal from the cantilever to a reference signal and outputs the phase and the frequency of the oscillation signal.

The frequency shift Δf is then obtained by simple subtraction of the resonance frequency of the cantilever at large tip-sample distance from the measured frequency:

$$\Delta f = f - f_0 \tag{9}$$

The Δf signal can then be recorded to obtain an AFM image or used as feedback signal in a z-regulator.

The outputted phase is used as input for the subsequent amplitude detection, proportional-integral regulator and phase shifter to maintain and regulate the constant set-point amplitude (A_s) of the oscillation. The full cycle is displayed schematically in figure 2.5(a).

The z-regulator is used to scan the sample at constant Δf. A set-point Δf is set and a branch is selected. The two branch options are the repulsive branch (left of the minimum for the blue curve in figure 2.5(b)) and the attractive branch (right of the minimum in the blue curve).

As an example; if the repulsive branch is selected and the z-regulator receives a Δf value that is lower than the set-point value Δf_{set} it will move the tip closer to the sample until the measured Δf corresponds to Δf_{set}. It is important to set the branch correctly, because if Δf is lower than Δf_{set} in the attractive branch, the z-regulator should increase the tip-sample distance instead, as shown in the insets of figure 2.5(b).

The non-monotonic relation between the signal (Δf) and the distance z causes complications when measuring molecules on surfaces. For example, when scanning at a Δf set-point in the attractive branch over a metal surface and a more positive Δf is measured at a certain position, the z-regulator will correctly decrease z until the set-

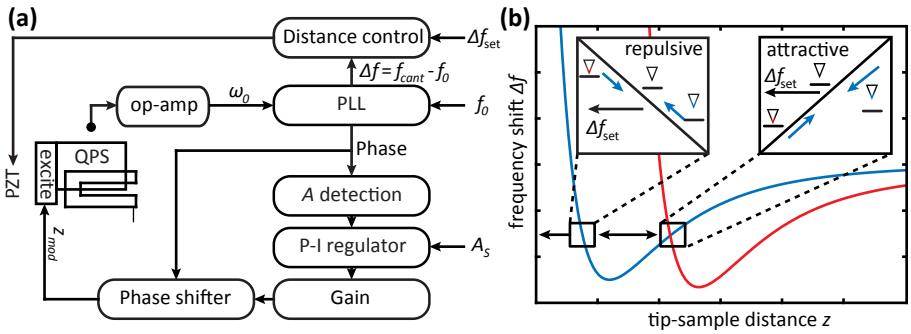

Figure 2.5 (a) Schematic of the FM-AFM qPlus sensor controller system. The qPlus sensor generates a current modulation at its resonance frequency. After amplification, this signal f is send to a PLL for phase and frequency detection. The Δf is used for z-regulation. The phase signal is used for the oscillation amplitude detection and subsequent regulation to the reference value A_s. After appropriate attenuation of the resulting signal, a 90° phase shifter will feed the signal back the z-mod piezo element. **(b)** Exemplary $\Delta f(z)$ curves to illustrate the difficulty of z-regulation over a sample with large z variation.

point is reached again. However, a high value of Δf can also be due to the tip scanning over a molecule. Since the molecule is adsorbed on top of the metal, the L-J curve will be shifted to higher z (red curve in figure 2.5(b)). Hence, above the molecule Δf_{set} us suddenly part if the repulsive branch. However, since the z-regulator was set to the attractive branch on the metal surface, the feedback mechanism will still respond to an increase in Δf by moving the tip closer to the surface, resulting in a tip crash.

Regulation in the repulsive branch will cause similar problems when scanning over a sample where the minimum of the $\Delta f(z)$ curves varies strongly spatially. Therefore, when imaging molecules on substrates the z-regulator is not used. Instead the Δf value is recorded as a function of lateral position while the tip-sample distance z is kept constant.

2.3 Imaging single molecules and chemical reactions

In recent years FM-AFM has flourished as a method to image molecules with sub-molecular resolution. The striking images are especially appealing because they show the molecules directly, without having to analyze a spectrum. Molecules in AFM images

largely look like what you would expect them to look like from reading chemistry textbooks. This section will show how AFM can be used to study chemical problems.

2.3.1 Resolving the chemical structure of an individual molecule

The first molecule that was resolved with sub-molecular resolution with AFM is pentacene.[15] Pentacene is a planar molecule consisting of five conjugated carbon rings (see figure 2.6(a)). Previous high resolution images of molecules were obtained with STM, which is sensitive to the electronic structure of the molecule; hampering imaging the chemical structure.[21]

The AFM image by Gross *et al.* reproduced in figure 2.6(c) shows a striking resemblance to textbook images of a pentacene molecule. In order to resolve the molecule with such detail Gross *et al.* used a functionalized tip apex. The key in imaging single molecules with AFM is overcoming the conflict between the need to approach the molecule closely to measure the force between tip and molecule with sub-molecular resolution and making sure these forces are not so strong as to cause the molecule to move or be picked up.

With this first set of images Gross *et al*. also started to elucidate the mechanism behind high-resolution AFM imaging. From their findings it was already clear that Pauli repulsion is a main cause for the cause the sub-molecular resolution, while van der Waals and electrostatic forces only contribute a diffuse background to the signal.[22] Further discussion on the mechanism behind high-resolution AFM images obtained with functionalized tips continued over the years and more on this topic is written in section 2.5.

2.3.2 Identifying molecules with AFM

The capability to image single molecules with sub-molecular resolution, opened up the opportunity to use AFM as a direct characterization tool. In chemistry, characterization of molecular structures is essential, and there are many techniques available. Some techniques to characterize molecules are mass spectrometry, nuclear magnetic resonance (NMR) and a plethora of spectroscopic techniques. All these techniques depend on the analysis of the cumulated signal over an ensemble of molecules. This

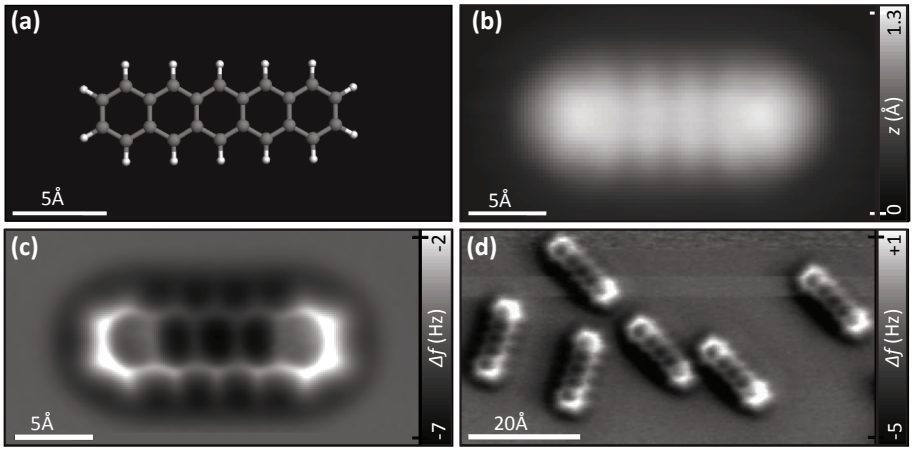

Figure 2.6 STM and AFM imaging of pentacene on Cu(111). **(a)** Ball-and-stick model of the pentacene molecule. **(b)** Constant current STM image at a set-point of 110 pA at 170 mV. **(c)** Constant height AFM image over a single pentacene molecule at -0.1 Å with respect to the STM set-point above Cu(111) with an oscillation amplitude of 0.2 Å. **(d)** Constant height AFM image over multiple pentacene molecules at 0.0 Å with respect to the STM set-point above Cu(111) and an oscillation amplitude of 0.8 Å. The asymmetry in the molecular imaging (showing a "shadow" only on the left side of the molecules) is probably caused by asymmetric adsorption geometry of the CO molecule at the tip apex.[15]

makes them resilient against statistical errors but also complicates the analysis of molecular mixtures. In addition, even with all techniques available, interpretation of the data is not always unequivocal, thus the addition of one more analysis technique was a welcome sight in the field of chemistry.

An example over which there had been some debate is on the structure of cephalandole A. Combined analysis with NMR and mass spectrometry yielded four possible structures (see figure 2.7(a)). Initially structure **2** had been assigned. Later it was found that structure **1** is the correct chemical representation of cephalandole A. To settle the debate, Gross *et al.*[23] used AFM to image a single cephalandole A molecule, aided by DFT calculations, they could confirm that out of the four proposed structures, structure **1** is correct. This illustrates the capabilities of AFM for chemical structure elucidation.

Other chemical compounds have been elucidated with help of AFM data that could not

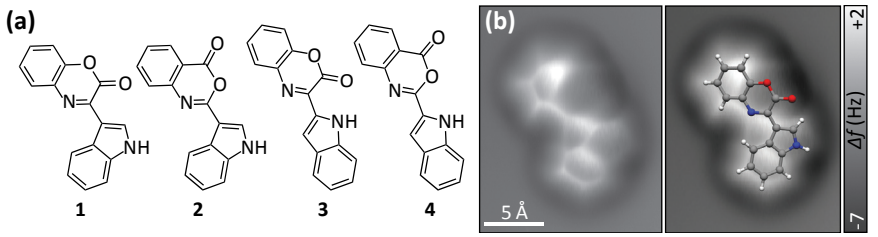

Figure 2.7 (a) The four possible compounds (**1** to **4**) consistent with the available NMR and mass spectrometry data. Compound **1** is the accepted structure of cephalandole A, and **2** is the previously misassigned structure of this compound. **(b)** Constant-height AFM measurements with a CO-functionalized tip were performed on a specimen adsorbed in the NaCl(2 ML)/Cu(111) surface. Image size: 16x19 Å. Oscillation amplitude 0.5 Å, sample voltage 0 mV. The images show the raw data and the same image with the molecular model of cephalandole A (**1**) overlaid as a guide to the eye.[23]

have been resolved by previous techniques alone.[24,25]

A notable case is the use of AFM to study molecules that occur n complex chemical mixtures such as asphaltenes. Due to the complexity of the mixture, ensemble based analysis techniques cannot be used to unambiguously identify the components on the mixture. By analyzing one molecule at a time, the chemical structure of asphaltenes could be unraveled.[26]

Additionally, careful analysis can provide information not only on the general structural skeleton of a compound but also bond order within planar polycyclic aromatic hydrocarbons can be determined.[27]

2.3.3 Observing chemical reactions, intermediates and products

The capability to visualize the chemical structure of single molecules, opens up the possibility to study chemical reactions and reaction mechanisms. One of the most employed strategies is to image reactants, anneal the sample to a certain temperature, and re-image the molecules. This procedure is repeated until the sample is annealed to a temperature where the reaction is completed (all molecules are converted).

Oteyza *et al.*[28] used AFM to image three different reaction products of oligo-(phenylene-1,2-ethynylenes) on a Ag(100) surface. Under annealing this enediyne

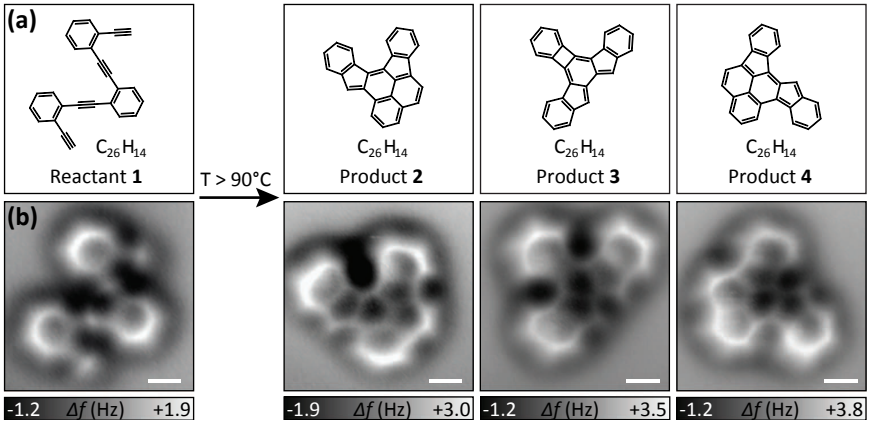

Figure 2.8 Comparison of nc-AFM images and structures for molecular reactant and products. **(a)** nc-afm image of reactant **1** on Ag(100) before annealing, and nc-AFM images of individual products **2**, **3**,and **4** on Ag(100) after annealing at T > 90°C. nc-AFM images were obtained at sample bias V = –0.2 V (f_0 = 29.73 kHz, Q = 90,000, A = 60 pm). **(b)** Schematic representation of the molecular structure of reactant **1** and products **2**, **3**, and **4**. All images were acquired with a CO-modified tip.[28]

undergoes a series of cyclization processes, see figure 2.8. AFM enabled determination of all three atomic structures in the mix of products. The determination of the reaction products after a complicated cyclization reaction resulted in an understanding of the reaction mechanisms.[29,30]

The fact that AFM imaging of molecules is performed at low temperature, typically T = 5 K, combined with the possibility to break C-H bonds with voltage pulses provides a wat to prepare and characterize reactive reaction intermediates that cannot be isolated by other means.[31] In figure 2.9 an example is shown of aryne; a reactive intermediate that has not been studied experimentally before. Pavlicek *et al.* used AFM to prove that this reaction intermediate can actually exist.[32]

In addition, if an AFM and STM are combined in one machine the tip can be used to induce chemical reactions under changing bias voltages and local electron tunneling. Moreover there is the ability to push or drag molecules across the surface to bring them close together and to induce inter-molecular reactions.[33–38]

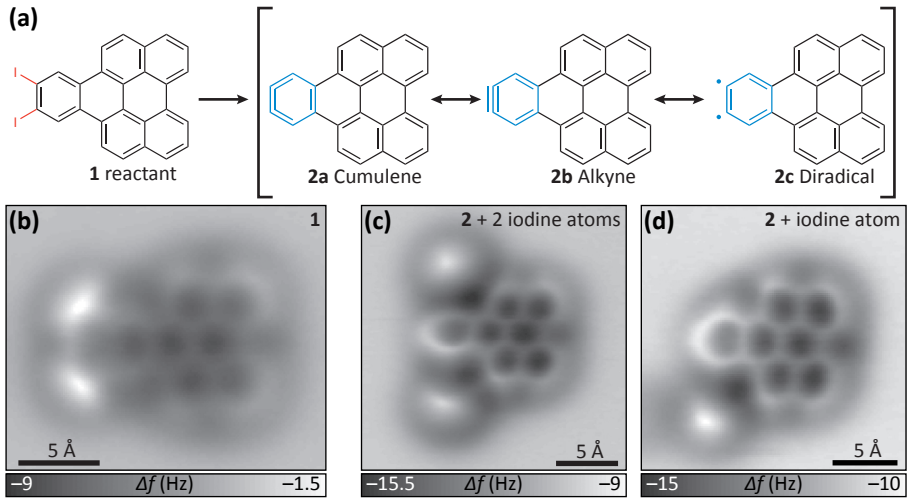

Figure 2.9 Tip induced formation and imaging of an aryle. **(a)** Schematic representation of **1** and the three resonance structures of the product **2a**-**2c**, after tip induces dehalogenation. **(b)** High-resolution AFM image of **1** obtained with an iodine terminated tip apex. (Δz = -1.1 Å w.r.t. STM set-point 2 pA at 0.2 V) **(c-d)** High-resolution AFM image of an aryne molecule close to two (c) and one (d) iodine atoms. (Δz = -1.2 Å)[32]

2.4 Tip termination

Most images we have seen so far are obtained with a tip terminated by a carbon monoxide (CO) molecule. While this is clearly an effective tip termination it is not the only horse in the race. Other tip terminations have been investigated and compared since the start of sub-molecular imaging. Gross *et al.* showed results obtained with Ag, Cl and pentacene decorated tip apices, along with the results with the CO-tip discussed above. To date, the CO-tip remains the most popular tip termination for imaging of single molecules in AFM. In this section we will look at alternative tip terminations and compare their advantages and disadvantages with respect to the ever-popular CO.

2.4.1 A closer look at the CO-tip

The procedure to create a CO-tip is often cited to Bartels *et al.*[39], who describe in detail how to pick up a CO molecule from a Cu(111) surface. The creation of a CO-tip is most quick and easy in STM imaging mode. The transfer of a CO molecule to the tip apex

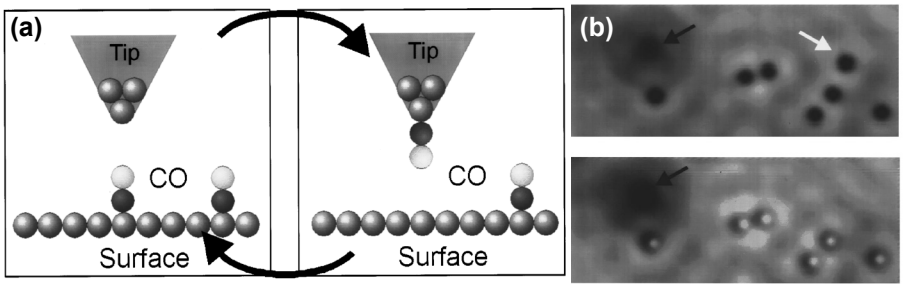

Figure 2.10 (a) Idealized sketch of the picking up and putting down procedures of CO molecules on Cu(111). Notice that the CO stands upright on the surface and has to switch its orientation when being transferred to the tip. **(b)** STM images of Cu(111) with ≈1% of a ML oxygen adsorbed at room temperature and some CO adsorbed at 15 K as taken with a metal tip (top) and after picking up a CO molecule (bottom). With the metal tip all adsorbates appear as depressions (dark spots). After picking up the adsorbate indicated with a white arrow all adsorbates appearing as protrusions (white spots) correspond to CO molecules, the adsorbate still appearing as an depression (black arrow) is hence identified as oxygen. Imaging conditions: 40 mV and 0.8 nA.[39]

consists of the following essential steps: finding and recognizing a CO molecule on the surface, tip relocation over the molecule followed by a combination of tip-sample bias and height changes, and finally the enhanced resolution due to a successful pick-up needs to be confirmed. Again, the combination of STM and AFM in one machine is a great asset for this procedure.

Figure 2.10(a) shows schematically what 'picking up a CO' means: a CO molecule adsorbed on the substrate. It can be transferred to an atomically sharp metal terminated tip. In STM images CO molecules on a metal surface imaged with a metal tip appear as depressions. This contrast changes after the successful pick-up of a CO molecule to a black ring with a white protrusion in the center. This contrast is typical for CO imaged with a CO-tip and well-understood.[40,41]

The use of a CO terminated tip also enhances spatial resolution of STM images.[21] There, the origin of the enhanced contrast is different. In STM the imaging mechanism depends on the overlap of molecular orbitals of tip and sample, and since the CO-

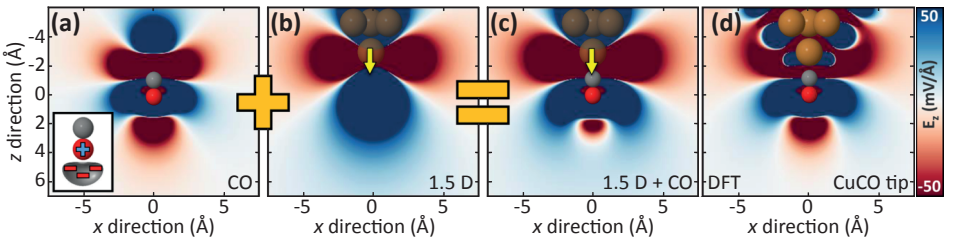

Figure 2.11 *z*-component of the electric field E_z of **(a)** a CO probe, **(b)** a 1.5 D dipole moment modeling a Cu metal tip, and **(c)** CO probe plus a 1.5 D dipole moment. The inset in (a) shows a scheme of the CO charge distribution that is responsible for the strongly negative (repulsive for electrons) E_z in front of the O atom. **(d)** Electric field of a CO–Cu tip as calculated through DFT.[42]

tip has spatially more localized *p*-wave orbitals the resolution is increased compared to the more spread-out s-wave orbital of a metal tip. In AFM sub-molecular contrast obtained by using CO-tips arises only in the regime where Pauli forces are dominant, the tip-sample distance needs to be very small. A sharp metal tip, ending in a single atom is typically very reactive. Thus approaching a molecule will more likely result in picking it up rather than a stable image. Since a Co molecule is relatively inert, the tip can approach the molecule of interest much closer. This allows stable imaging at tip-sample distances where the Pauli repulsion forces are the dominant contributor to the total tip-sample interaction.

The bond between the CO and the metal tip is flexible, *i.e.* at large distances the metal-C-O angle is 180° but under the influence of forces it can deflect and bend.[40] It is now well established that this flexibility essential to understand the contrast observed in AFM images of molecules acquired with CO-terminated tips.

Since the equilibrium position of the CO is vertical, and it will rotate away under a force, a spring constant k can be defined for the metal-CO bond. A high k represents a rigid bond, and a low k represents a bond where the CO can deflect easily.

The charge distribution over the CO and the metal tip is of importance to understand the imaging mechanism. Not only does this bond determine the value of k, but it also affects the effective charge on the CO molecule Q. Any transfer of charge between the CO molecule and the metallic tip-apex will affect the Coulomb forces between tip and

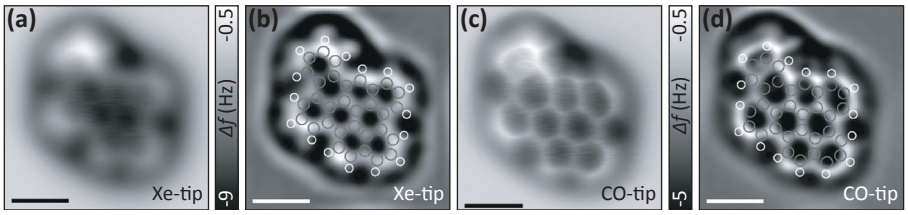

Figure 2.12 (a,c) Constant-height AFM images of a hydrocarbon molecule on NaCl(2ML)/Cu(111). The images were recorded with **(a)** a Xe-tip and **(c)** a CO-tip. **(b,d)** Laplace and low-pass filtered versions of (a) and (c), with atomic positions overlaid. Carbon and hydrogen atoms are colored in gray and white, respectively. Scale bars: 5 Å.[44]

sample. In first order, the effective charge on the CO can be approximated by a point-charge during simulations, as discussed in Chapter 4 of this thesis. Chapter 4 also introduces a method to determine k and Q from experimental data.

A more realistic view of the electrostatic charge around the CO was recently given by Ellner *et al.*[42] They used DFT simulations to study the effect of the metal-CO bond on the natural dipole moment of CO. Figure 2.11 depicts the results. The z component of the electric field E_z as calculated by DFT resembles closely the addition of the natural dipole of CO + a dipole in the metal tip. This complicated electric field around the CO-tip results in different significance and sign of the electrostatic contribution to the force at varying height.

2.4.2 Other tip apex modifications

Attaching a molecule or atom to the tip apex is called functionalizing the tip. Thus far we looked into the details surrounding CO-tips. However the options for tip functionalization seem theoretically endless.[43] Experimentally the merit of a few alternative tip functionalities has been demonstrated.

Figure 2.12 shows a comparison between images of the same hydrocarbon molecule obtained with CO and Xe functionalized tips. Both show sub-molecular resolution. However the bond lengths and bond angles are much more distorted in the CO-tip image. The authors assign this difference to a difference in k between the CO-tip and Xe-tip bonds, where Xe is expected to have a higher k, and is thus less flexible

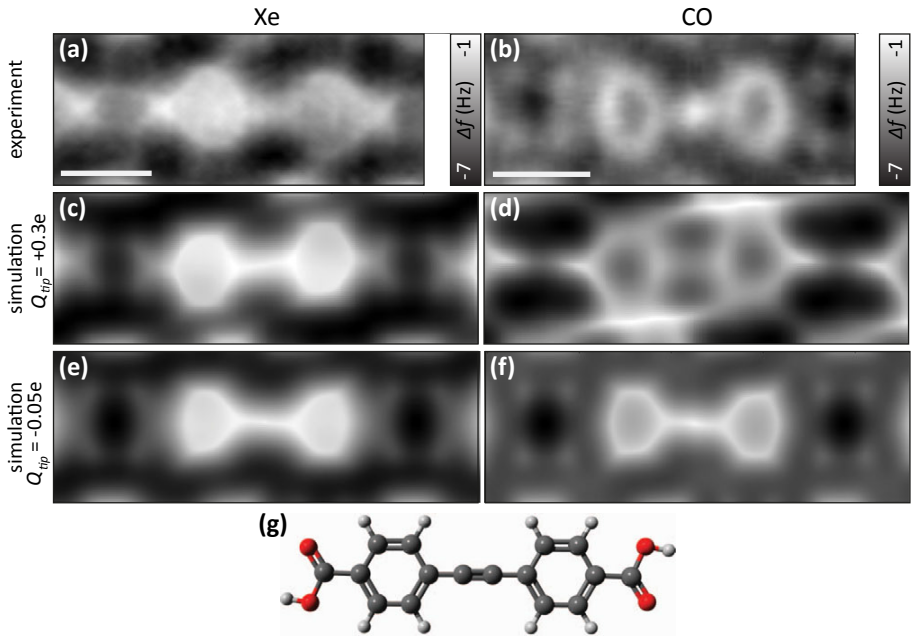

Figure 2.13 Importance of tip charge in simulated Δf images of molecules with a non-homogeneous charge distribution. **(a-b)** Constant-height Δf images recorded with Xe- and CO-tips on a self-assembled layer of molecules (−3 Å and −2.4 Å w.r.t. STM set-point 10 pA at 0.1 V). **(c-d)** Simulations with tip charge: Q_{tip} = 0.3 e for the Xe and CO terminated tips. **(e-f)** Simulations with tip charge Q_{tip} = −0.05 e for the Xe and CO terminated tips. $k_{x,y}$ = 0.25 Nm^{-1} in all calculations. **(g)** Ball-and-stick model of the molecule. Left panel: Xe. Right panel: CO. Scale bars are 5 Å.[45]

in tilting away.[44]

Since AFM is based on the interaction between tip and sample, the properties of the tip are an important factor in imaging. The common method for preparing a sharp metal tip does not offer any conclusive evidence about the exact atomic structure at the tip apex. Functionalizing the tip therefore has the added benefit of having a known and reproducible tip. This facilitates theoretical calculations and simulations of the experiments.

An example of when the effective charge Q of the functionalized tip has a significant effect on the AFM contrast is when the imaged molecules have a non-homogeneous

charge distribution. Figure 2.13 shows the work of van der Lit *et al.*[45], where a stark difference in observed due to the different Q of a CO-tip and a Xe-tip. The Xe-tip was found to have a partial positive charge of Q = +0.3 e, while the CO-tip had as slightly negative charge of Q = -0.05 e. The investigated molecule has a triple bond in the center, which is associated with a partial negative charge, and a carboxyl group at each end. Within the carboxyl group the oxygen atoms have a partial negative charge, while the connecting carbon atom has a partial positive charge. The electrostatic interactions between the two different tip terminations and the differently charged areas of the molecule are clear from the image.

The regions of access negative charge appear bright in the image acquired with a CO tip, whereas regions of positive charge appear darker. Bright contrast is associated with a repulsive interaction force, and vice versa is darker contrast associated with an attractive interaction force in images obtained with a CO terminated tip. In contrast when imaged with a positively charged Xe-tip, the partially negatively charged oxygen atoms appear dark, whereas the partially positively charged carbon atom of the carboxyl groups show up as bright extensions of the rings.

Aside from CO and Xe some other tip terminations that have been used experimentally are Cl^- ions picked up from NaCl ML,[15] C_{60} molecules,[46] and organic molecules.[47] Each different tip functionalization has its advantages and disadvantages. An ideal tip-functionalization is easy to pick up but stable once attached to the tip, has a small diameter to enable high spatial resolution, and is not flexible to prevent distortions, as well as being chemically inert to prevent pick-up events and to not interfere with the chemical composition of the molecule under investigation. In addition a tunable effective charge is useful when investigating the charge distribution in molecules, as discussed in chapter 4.

Recently a new type of tip termination has been demonstrated.[48] Instead of picking up an adsorbed molecule or atom from the surface to functionalize the tip, Mönig *et al.* propose to use a very rigid copper oxide tip. They demonstrate that definitive characterization of the tip geometry, including the metal-oxygen bond, is possible. A ball-and-stick model of the tip apex is shown in figure 2.14(a). The oxygen atom is

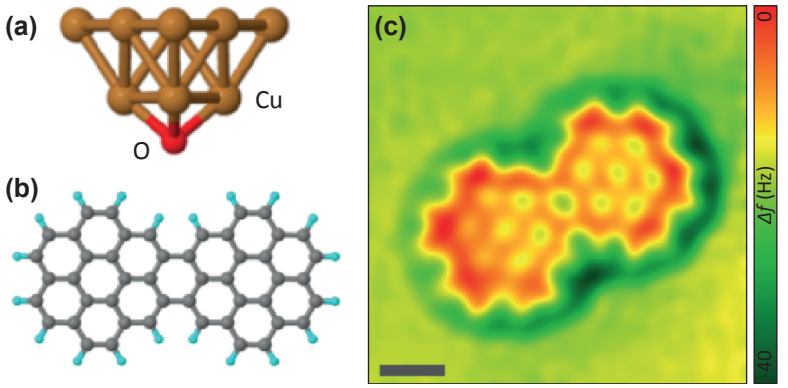

Figure 2.14 (a) Cu-based model tips terminated by an O atom (CuO-tip). **(b)** Constant-height frequency shift image recorded on a single molecule adsorbed on Cu(110) with an O- terminated Cu tip. **(c)** Structural model.[48]

back bonded to 3 copper atoms in a blunt tetrahedral configuration, which makes the oxygen atom very rigid. The result of a tip apex with a very high k is that bond lengths and bond angles do not appear distorted, see figure 2.14(b) However, as we will see in more detail in 2.5, the apparent bonds also appear less sharp with a rigid tip.

For the future I predict that the diversity in tip functionalizations will increase as each tip has its benefits and drawbacks. The rigid CuO-tip has great promise when there is a need to compare data quantitatively to simulated data. However, for qualitative information I think that the now almost standard CO-tip will remain popular, with some competition of tips functionalized by the very molecules that are being studied.

2.5 Discussion on interpretation

There are many components that factor into the observed contrast in AFM images. The convolution of all forces that play a role in AFM imaging of organic molecules is not straightforward to untangle. Electrostatic, van der Waals, Pauli and magnetic forces, as well as junction flexibility, all contribute to the tip-sample interaction, and thus to the image contrast. In this section some of the difficulties in interpretation of AFM data will be discussed. Particular attention will be given to the effect of the flexibility of the probe.

2.5.1 Simulate to understand

A common method to form a better understanding of experimental results is simulation of the experiment. Various computational approaches are available. The two most widely used approaches in the field of imaging molecules with SPM are density functional theory (DFT) and molecular mechanics (MM).

A realistic simulation result requires an accurate, detailed and inclusive description of the experimental process. For AFM this means that all the factors mentioned above need to be considered in the simulation: a quantum mechanical description of the sample and tip, the oscillation of the tip, the flexibility and the charge of the tip.

The relations in section 2.2.1 suggest that the total electron density (TED) obtained from DFT calculations might be used in a direct comparison to AFM images. And to first approximation a slice of the TED at a certain height does resemble AFM images well.[49] Due to the exclusion of the tip entirely in this approach, any effects caused by interactions with the tip are not taken into account. As a result, this approach cannot account for the experimentally observed contrast in all cases.[50–52] Thus a more inclusive approach is needed in order to utilize DFT effectively for AFM simulations.

While DFT generally gives accurate quantum mechanical descriptions for tip, sample, charge and bond-strength, it is awfully computationally expensive for the time resolved simulations needed to include the oscillation of the tip. Molecular mechanics can describe dynamic changes in the experiment much more efficiently. However MM needs a lot of empirical input values while DFT is an *ab initio* method, wherein all physical quantities follow from theory.

A combination of both approaches is therefore commonly used. The molecular structure, adsorption height, charge distribution of the molecule are calculated by a static, single energy DFT calculation. This *ab initio* sample model is then used to simulate the AFM imaging process with MM.

The MM model that is used for this thesis (the 'probe particle model') is developed over several iterations,[53–55] and includes the charge distribution within the sample (from DFT), a model point-charge Q or dipole for the tip, a spring constant k for the flexibility of the probe-metal bonds and the oscillation amplitude A of the tip.

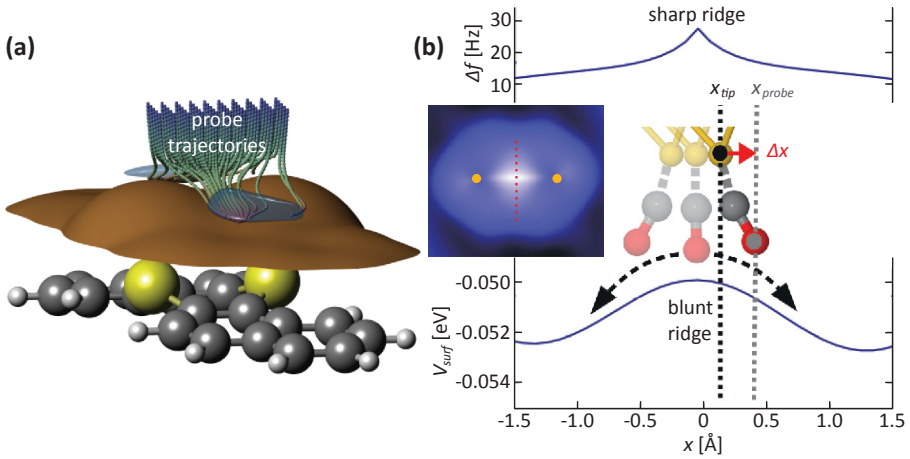

Figure 2.15 Origin of sharp lines in AFM images. **(a)** Molecule (below) with repulsive potential (brown) felt by the probe particle. Probe particle trajectories upon tip approach are also shown. A saddle is formed between two atoms. **(b)** Surface potential V_{Surf} (bottom) and AFM frequency shift Δf (top) along the central cross section of the repulsive saddle. In the center the relaxation Δx of the probe particle towards the position x_{probe} is shown schematically for a tip position x_{tip} close to the ridge of the saddle. The mapping of the force at x_{probe} to the macroscopic tip position x_{tip} explains the sharpening of the Δf curve ("sharp ridge") even for a smooth saddle in V_{Surf} ("blunt ridge"). The inset shows a simulated AFM image of the region of the saddle in repulsive potential, clearly exhibiting the sharp line between the atoms.[53]

Other simulation approaches include a consideration of the tip and the tip-sample interaction.[56–58] However, in this thesis preference was given to the MM model because it is in very good agreement with the experimental AFM images, and the inputted empirical values and provides more insight in the physical mechanism behind the contrast formation.

2.5.2 Sharp edges and image distortions

From quantum mechanics it is known that molecular bonds are not narrow, straight lines, as they often are displayed in chemistry textbooks. However, in AFM images molecules do look very familiar to those textbook images. Looking back at the image of the pentacene molecule in figure 2.6, it is clear that the hexagonal carbon rings appear stretched vertically in the AFM image. The extent to which they are stretched

is unphysically large; even for adjusting molecular bonds to minimize the energy after adsorption. These image distortions, along with the unexpected sharply imaged bonds, lead to a reexamination of which processes are important in AFM images.

A method to undo the image distortion by looking at the lateral force on the probe particle model (PPM) highlights the importance of these lateral forces simulations.[59] The probe particle model demonstrates the origin of the observed lateral distortions as well as the reason for the sharp edges.[55] Innovative of the PPM is the degrees of freedom of the probe particle itself. The molecule or atom with which the tip is functionalized is modeled by a probe particle. Figure 2.15 illustrates the mechanism behind the sharp edges. During the oscillation of the tip the probe will follow any of the trajectories as it approaches the sample. The forces acting between the probe and the sample include electrostatic, van der Waals and Pauli forces. When the probe approaches very close to the sample the repulsive Pauli force will cause the tip to tilt away. For any non-infinite spring constant k the bifurcation of the probe trajectories is inevitable. This bifurcation, where the probe goes either left or right of a saddle point in the TED-landscape, will manifest itself as a straight, sharp line in AFM images. For a small k the Pauli repulsion does not need to be very high to cause lateral movement of the probe. The height at which the bifurcation occurs depends on k and the strength of the tip-sample interaction as the driving force causing the lateral movement of the probe particle is strongly height dependent.

It is important to note that tip tilting also contributes to the contrast in STM images, when the imaging height is below the bifurcation height.[60,61]

An exemplary demonstration of image distortions due to chemical interactions is shown in figure 2.16.[62] The molecule consists of four benzene rings connected by two triple-bonded carbon atoms. The two benzene rings on the left are terminated by hydrogen atoms, while the two on the right have fluorine atoms instead. The carbon backbone is equal on both sides. The differently terminated benzene rings have markedly different contrast in the AFM image. Most notably, the rings appear to have largely different sizes. The authors conclude that the difference primarily originates from the difference in the extension of the π-electrons of the fluorinated and non-

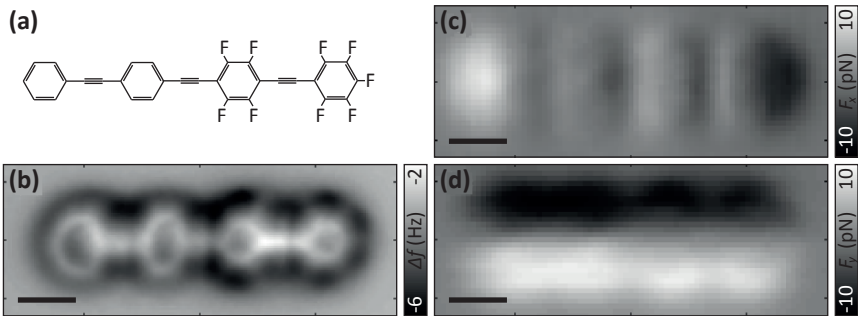

Figure 2.16 (a) The chemical structure of a partially fluorinated hydrocarbon molecule. Green crosses indicate the lateral positions y_{bond} that are compared to quantify the distortions, and blue arrows indicate the lateral positions of the line scans. **(b)** Measured constant-height frequency shift Δf image. The lateral forces extracted from a three-dimensional force map: **(c)** F_x in the x-direction and **(d)** F_y in the y-direction. Measurements **(b–d)** correspond to a tip height of z = 3.55 Å.[62]

fluorinated rings. They accredit tilting of the CO tip at different scanning positions to a difference in van der Waals forces between the CO-tip and the hydrogen/fluorine.

Chapter 4 of this thesis will go into more detail about the origin of image distortions and the influence of electrostatic charges on the apparent position and size of features.

2.5.3 Intermolecular bonds

Knowing imaging artifacts exist motivated us strongly to reexamine images that were previously interpreted with a straightforward mindset. An example is given by the imaging of hydrogen-bonds by Zhang *et al.*, see figure 2.17.[63]

The existence of hydrogen bonds between hydroxyl groups and pyridinic nitrogen atoms is obvious to any chemist. The sub-molecular resolution of AFM has enabled Zhang *et al.* to image configurations of a group of molecules that form inter-molecular hydrogen bonds. The skeletal structures of the molecules are clearly resolved. Over the locations where hydrogen bonds are expected, a repulsive contrast is observed in the images; sharp lines at the approximate locations of the intermolecular bonds. As shown previously, sharpening of features results from tilting of the tip at saddle points in the potential energy landscape. It is important to realize that saddle points in the potential energy landscape can form in the absence of chemical bonds. Therefore,

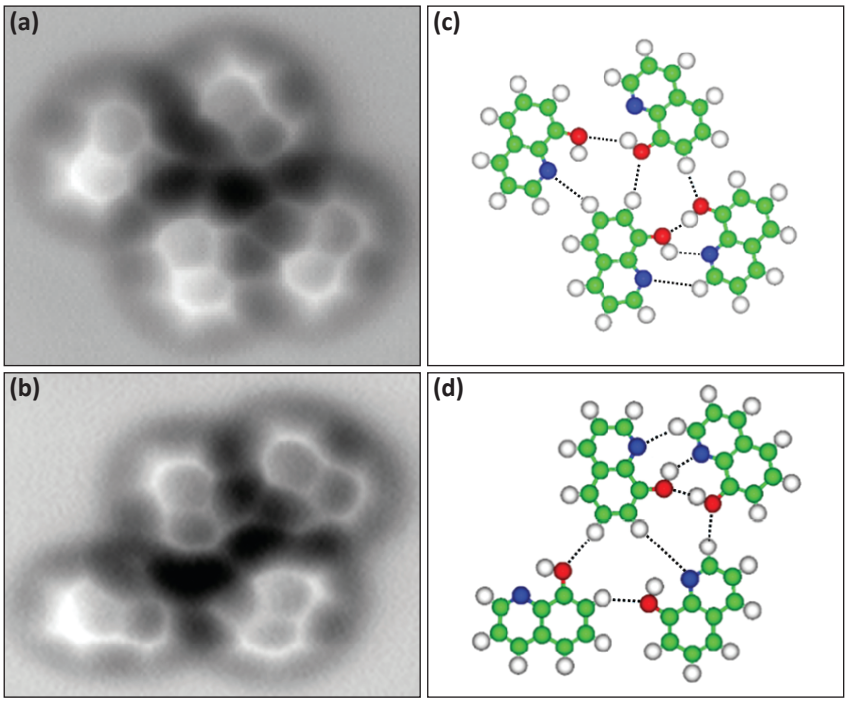

Figure 2.17 AFM measurements of assembled clusters of molecules on Cu(111). **(a-b)** Constant-height frequency shift image of typical molecule-assembled clusters and their corresponding structure models **(c-d)**. Imaging parameters: V = 0 V, A = 100 pm, Δz = +10 pm. Image size: (a) 2.3 by 2.0 nm; (b) 2.5 by 1.8 nm. The dashed lines in (c) and (d) indicate likely H-bonds between molecules. Green, carbon; blue, nitrogen; red, oxygen; white, hydrogen.[63]

assigning line-features to be bonds needs to be done with the utmost care and skepticism. Hydrogen bonds are predominantly electrostatic in origin and the change in the electron density between the atoms is small.

Chapter 3 of this thesis will explore the interpretation of bond-like features in more detail.

To strengthen the argument that tip-flexibility is a cause for bond-like features Jarvis *et al.* imaged a self-assembly of C_{60} molecules with a C_{60} terminated tip, see figure 2.18.[64] The center-to-center distance between the C_{60} molecules is about 1 nm, much too long for inter-molecular bonds. Nonetheless intermolecular bond-like features are

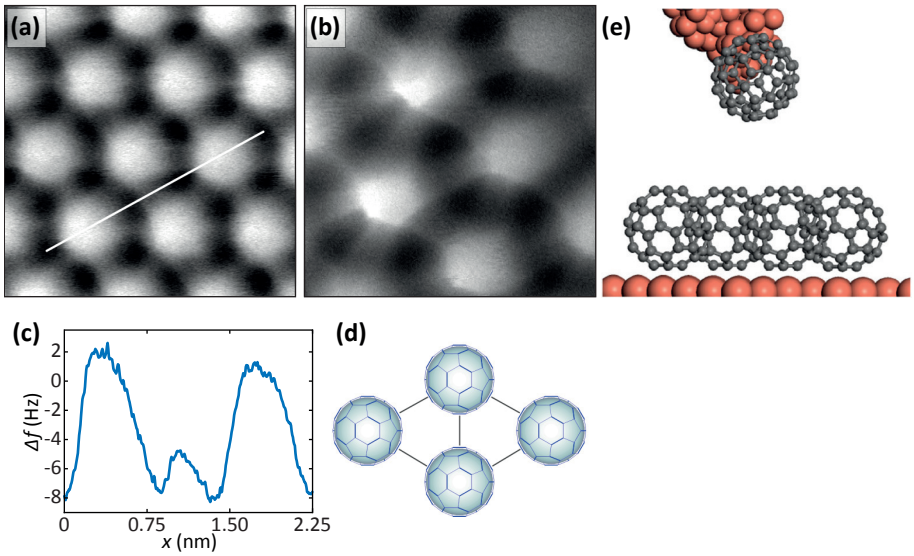

Figure 2.18 Apparent intermolecular features. NC-AFM frequency shift images of a 2D assembly of **(a)** a thick (six-layer) film of $H_2O@C_{60}$ (image size: 3.2 × 3.2 nm, oscillation amplitude: 300 pm) and **(b)** C_{60} molecules recorded (image size: 2.3 × 2.3 nm, oscillation amplitude: 110 pm) in the constant height mode, revealing interconnecting features between nearest neighbor molecules. **(c)** Line profile measurement along the white line shown in (a). **(d)** Schematic of the C_{60} packing arrangement and locations of apparent intermolecular features. **(e)** Illustrative and schematic diagram of experimental setup. Note that a single C_{60} molecule is shown bound to the tip apex. It is more likely that the tip apex is covered with a number of C_{60} molecules.[64]

observed. Additionally, they showed that the bond-like features only appear below a height where Pauli repulsion is significant, and thus where repulsive tip-tilting is likely.

The discussion on the origin of bond-like features in AFM images is still ongoing, however there is consensus that not all bond-like features arise from bonds.[50,58,65] The better understanding of the imaging mechanism of bond-like features in AFM can be of practical use. Imaging artifacts that impede straightforward interpretation evolve into features of interest, that hold information on the molecular system.[66]

2.6 Adding a third dimension

Although AFM is generally considered a surface science, generating 2D images, the future will hold more elaborate strategies that venture into the third data dimension.

2.6.1 How to deal with non-planar molecules

Most molecules that are investigated by AFM are planar hydrocarbons, and have an at least partially conjugated π-system of flat benzene rings. If AFM is to continue as a technique that can help understand chemical reactions on surfaces to assist catalyst design, the molecule diversity needs to increase drastically. Imaging the full 3D structure of proteins with AFM is not a realistic conjecture. However, recent developments have shown that imaging smaller non-planar molecules is feasible. One method, demonstrated by Albrecht *et al.*,[29] uses multiple scanning planes that are not perpendicular to the surface. Figure 2.19 depicts this technique at a glance. The molecular structure is identified from a 3D data set. To resolve the structure of a non-planar molecule from Δf imaging, the 3D data set is displayed along three different planar cross sections. While one of them is parallel to the surface, the other two are aligned with respect to the two carbon rings that are tilted with respect to the surface, green and red in figure 2.19(a).

Another technique to look at non-planar molecules is proposed by Moreno *et al.*[67] and uses a multipass method, where the tip scans the surface twice. The first scanline runs in feedback, to get a topography based on the van der Waals forces. The second scanline runs out of feedback, while using the first scanline plus a vertical offset to obtain atomic resolution on both the substrate and an adsorbed molecule.

2.6.2 Applications of 3D Δf data

AFM can provide more information on molecules than just their chemical structure. The Lennard-Jones shaped curves from $\Delta f(z)$ spectra contain all forces between the tip and the position over the sample where the spectrum was obtained. Sugimoto *et al.*[68] showed that these forces differ significantly between different chemical species, and can be used for chemical identification of atoms in surface alloys. Building on this idea, it has been shown for many systems that atomic species can be distinguished by

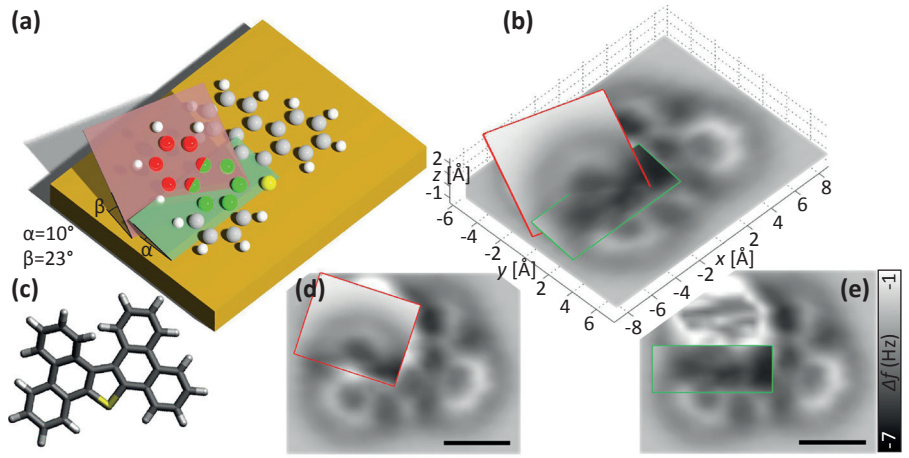

Figure 2.19 Molecular structure identification from a 3D data set. **(a)** 3D representation of molecular structure including the cross sections, along which the experimental data is displayed in **(b)**. **(c)** Top view of the geometric structure. **(d, e)** Top views of 3D data with only one of the tilted cross sections in each panel (scale bars 5 Å).[29]

looking at the $\Delta f(z)$ spectra or the total 3D Δf data block over the sample.[68–71]

Mapping the entire force field over an adsorbed molecule was the next step in using 3D Δf data.[72] Chapter 5 and 6 of this thesis shows how mapping 3D Δf data can be combined with the insight by Sugimoto *et al.* to chemically distinguish between atomic species in doped graphene and organic molecules.

The position of the minimum of a $\Delta f(z)$ spectrum can be mapped over the scan area by analyzing 3D Δf data. The coordinates of the minimum $\Delta f^*(x,y)$ and $z^*(x,y)$ are of interest because they allow us to compare Δf values on equal footing instead of at a single height and the height z at which Pauli repulsion starts to become significant. Schuler *et al.*[73] showed that by mapping $z^*(x,y)$ the relative adsorption height within and between molecules can be determined. Two of the $z^*(x,y)$ maps on two hydrocarbon molecules are shown in figure 2.20. The carbon backbone structure is clear from the $z^*(x,y)$ maps, as well as the parabolic adsorption shape of pentacene, as predicted by DFT.

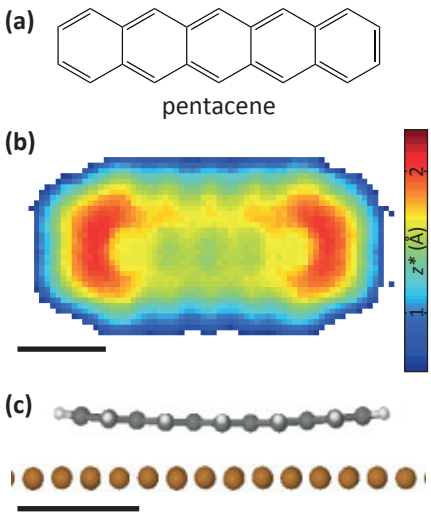

Figure 2.20 (a) Chemical structure of pentacene. **(b)** The tip height z^* at minimal Δf on pentacene on Cu(111) with a CO terminated tip. $z^*(x,y)$ is extracted from a 3D Δf map and given with respect to the z^* value on Cu(111). White points mark spectra where the Δf minimum was not reached during data acquisition. **(c)** The calculated geometry for pentacene on Cu(111) using DFT + vdW^{surf}. Scale bars are 5 Å.[73]

Chapter 5 and 6 of this thesis also employ $\Delta f^*(x,y)$ and $z^*(x,y)$ maps and reveals how these can be used in atom and molecule identification. Chapter 7 contains a detailed analysis of the adsorption geometry two isomers also using 3D Δf data.

2.6.3 KPFM

Kelvin probe force microscopy (KPFM) is closely related to AFM because it also probes forces between tip and sample. Where 3D AFM data usually maps force or Δf as a function of tip-sample distance z, in KPFM the bias voltage between tip and sample V is varied and Δf is measured as a function of V. The resulting $\Delta f(V)$ curve is a parabola, as can be seen in the inset of figure 2.21(a). The top of this parabola is where the force is minimum; the frequency shift is closest to 0 Hz. The bias-voltage that need to be applied to reach this situation is the voltage that compensated the contact potential difference between tip and sample. It is therefore known as the local contact potential difference (LCPD) V^*.[74]

The contact potential difference between tip and sample fluctuates for different areas of the sample when the sample has a non-homogeneous charge distribution or chemical structure. KPFM can therefore be used to identify atomic species, defects and charge states.[75–77]

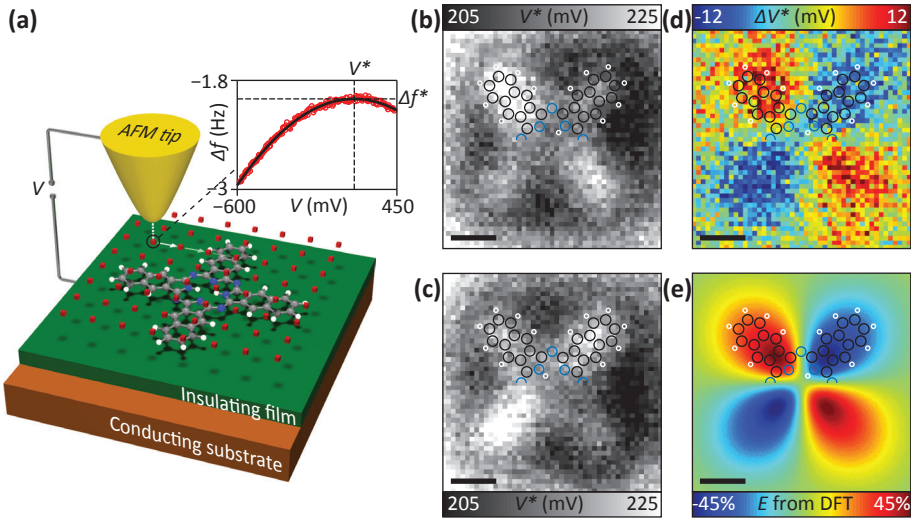

Figure 2.21 LCPD images of the tautomerization switching of naphthalocyanine. **(a)** Schematic of the measurement principle. At each tip position, the frequency shift is recorded as a function of the sample bias voltage (inset, red circles). The maximum of the fitted parabola (inset, solid black line) yields V^* and Δf^* for that position. **(b-c)** LCPD images of naphthalocyanine on NaCl(2ML)/Cu(111) before (b), and after (c), switching the tautomerization state of the molecule. The images were recorded with a copper-terminated tip on a 64×64 lateral grid at constant height (z = 0.1 nm w.r.t. the STM set-point over the substrate of 3 pA at 0.2 V). **(d)** Difference image obtained by subtracting c from b. **(e)** DFT-calculated asymmetry of the z-component of the electric field above a free naphthalocyanine molecule at a distance d = 0.5 nm from the molecular plane. All scale bars are 0.5 nm. The DFT-calculated atomic positions are overlaid in the upper halves of b–e. Carbon, hydrogen and nitrogen atoms are in grey, white and blue, respectively.[78]

Mohn *et al.* demonstrated that the LCPD measured by KPFM relates to the total charge distribution of a molecule.[78] Figure 2.21 shows contour plots of V^* as a function of lateral position for two tautomers before and after switching, see figure 2.21(b-c). The difference between these two KPFM images clearly resembles the electric field over the molecule as calculated by DFT.

Despite the established existing relationship between the LCPD as measured by KPFM and the electric field there is still ongoing discussion on the interpretation of KPFM images.[79] The LCPD cannot be related directly, numerically, to electrostatic

force, charge density, or the electric field. At large tip-sample distances the LCPD qualitatively resembles the electrostatic field. At small tip-sample distances where atomic resolution is usually obtained the LCPD is still mostly the result of Pauli repulsion rather than electrostatic interactions.[80] The ambiguous interpretation at different heights hampers the use of KPFM for imaging the electrostatic field of molecules with sub-molecular resolution. In chapter 7 of this thesis KPFM is used to detect the presence of a dipole moment in an adsorbed molecule.

New techniques have been presented that do result in maps of charge distributions with sub-molecular resolution.[81] Chapter 4 of this thesis outlines a method for measuring the electrostatic field over a molecule with sub-molecular resolution, without making use of the LCPD, but by looking directly at electrostatic forces.

2.7 References

[1] I. Swart, L. Gross, P. Liljeroth, Single-molecule chemistry and physics explored by low-temperature scanning probe microscopy. *Chem. Commun.* **47**, 9011–9023 (2011).

[2] L. Gross, Recent advances in submolecular resolution with scanning probe microscopy. *Nat. Chem.* **3**, 273–278 (2011).

[3] C. Barth, A. S. Foster, C. R. Henry, A. L. Shluger, Recent trends in surface characterization and chemistry with high-resolution scanning force methods. *Adv. Mater.* **23**, 477–501 (2011).

[4] F. J. Giessibl, Advances in atomic force microscopy. *Rev. Mod. Phys.* **75**, 949–983 (2003).

[5] E. I. Altman, M. Z. Baykara, U. D. Schwarz, Noncontact Atomic Force Microscopy: An Emerging Tool for Fundamental Catalysis Research. *Acc. Chem. Res.* **48**, 2640–2648 (2015).

[6] G. Binnig, C. F. Quate, Atomic Force Microscope. *Phys. Rev. Lett.* **56**, 930–933 (1986).

[7] G. Binnig, H. Rohrer, Scanning tunneling microscopy. *Surf. Sci.* **126**, 236–244 (1982).

[8] Y. Martin, H. K. Wickramasinghe, Magnetic imaging by "'force microscopy'" with 1000 Å resolution. *Appl. Phys. Lett.* **50**, 1455–1457 (1987).

[9] G. Meyer, N. M. Amer, Novel optical approach to atomic force microscopy. *Appl. Phys. Lett.* **53**, 1045–1047 (1988).

[10] W. Clauss, J. Zhang, D. J. Bergeron, A. T. Johnson, Application and calibration of a quartz needle sensor for high resolution scanning force microscopy. *J. Vac. Sci. Technol. B Microelectron. Nanom. Struct.* **17**, 1309 (1999).

[11] F. J. Giessibl, High-speed force sensor for force microscopy and profilometry utilizing a quartz tuning fork. *Appl. Phys. Lett.* **73**, 3956–3958 (1998).

[12] G. Binnig, C. Gerber, T. R. Albrecht, C. F. Quate, Atomic Resolution with Atomic Force Microscope. *Europhys. Lett.* **3**, 1281–1286 (1987).

[13] T. R. Albrecht, P. Grütter, D. Horne, D. Rugar, Frequency modulation detection using high- Q cantilevers for enhanced force microscope sensitivity. *J. Appl. Phys.* **69**, 668–673 (1991).

[14] F. J. Giessibl, Forces and frequency shifts in atomic-resolution dynamic-force microscopy. *Phys. Rev. B.* **56**, 16010–16015 (1997).

[15] L. Gross, F. Mohn, N. Moll, P. Liljeroth, G. Meyer, The Chemical Structure of a Molecule Resolved by Atomic Force Microscopy. *Science.* **325**, 1110–1114 (2009).
[16] D. Y. Abramovitch, S. B. Andersson, L. Y. Pao, G. Schitter, A Tutorial on the Mechanisms, Dynamics, and Control of Atomic Force Microscopes. *2007 Am. Control Conf.*, 3488–3502 (2007).
[17] J. E. Sader, S. P. Jarvis, Accurate formulas for interaction force and energy in frequency modulation force spectroscopy. *Appl. Phys. Lett.* **84**, 1801–1803 (2004).
[18] J. L. Hutter, J. Bechhoefer, Calibration of atomic-force microscope tips. *Rev. Sci. Instrum.* **64**, 1868–1873 (1993).
[19] F. J. Giessibl, F. Pielmeier, T. Eguchi, T. An, Y. Hasegawa, Comparison of force sensors for atomic force microscopy based on quartz tuning forks and length-extensional resonators. *Phys. Rev. B.* **84**, 125409 (2011).
[20] F. J. Giessibl, Atomic resolution on Si(111)-(7×7) by noncontact atomic force microscopy with a force sensor based on a quartz tuning fork. *Appl. Phys. Lett.* **76**, 1470–1472 (2000).
[21] L. Gross, N. Moll, F. Mohn, A. Curioni, G. Meyer, F. Hanke, M. Persson, High-Resoution Molecular Orbital Imaging Using a p-Wave STM *Tip. Phys. Rev. Lett.* **107**, 86101 (2011).
[22] N. Moll, L. Gross, F. Mohn, A. Curioni, G. Meyer, The mechanisms underlying the enhanced resolution of atomic force microscopy with functionalized tips. *New J. Phys.* **12**, 125020 (2010).
[23] L. Gross, F. Mohn, N. Moll, G. Meyer, R. Ebel, W. M. Abdel-Mageed, M. Jaspars, Organic structure determination using atomic-resolution scanning probe microscopy. *Nat. Chem.* **2**, 821–825 (2010).
[24] K. O. Hanssen *et al.*, A combined atomic force microscopy and computational approach for the structural elucidation of breitfussin A and B: Highly modified halogenated dipeptides from thuiaria breitfussi. *Angew. Chemie.* **51**, 12238–12241 (2012).
[25] N. Pavliček, B. Fleury, M. Neu, J. Niedenfu, C. Herranz-lancho, M. Ruben, J. Repp, Atomic Force Microscopy Reveals Bistable Configurations of Dibenzo[a,h] thianthrene and their Interconversion Pathway. *Phys. Rev. Lett.* **108**, 86101 (2012).
[26] B. Schuler, G. Meyer, D. Peña, O. C. Mullins, L. Gross, Unraveling the Molecular Structures of Asphaltenes by Atomic Force Microscopy. *J. Am. Chem. Soc.* **137**, 9870–9876 (2015).
[27] P. Varga, M. Schmid, Chemical discrimination on atomic level by STM. *Appl. Surf. Sci.* **141**, 287–293 (1999).
[28] D. G. de Oteyza, P. Gorman, Y.-C. Chen, S. Wickenburg, A. Riss, D. J. Mowbray, G. Etkin, Z. Pedramrazi, H.-Z. Tsai, A. Rubio, M. F. Crommie, F. R. Fischer, Direct Imaging of Covalent Bond Structure in Single-Molecule Chemical Reactions. *Science.* **340**, 1434–1437 (2013).
[29] F. Albrecht, N. Pavliček, C. Herranz-Lancho, M. Ruben, J. Repp, Characterization of a Surface Reaction by Means of Atomic Force Microscopy. *J. Am. Chem. Soc.* **137**, 7424–7428 (2015).
[30] S. Kawai *et al.*, Thermal control of sequential on-surface transformation of a hydrocarbon molecule on a copper surface. *Nat. Commun.* **7**, 12711 (2016).
[31] Q. Sun, L. Cai, S. Wang, R. Widmer, H. Ju, J. Zhu, L. Li, Y. He, P. Ruffieux, R. Fasel, W. Xu, Bottom-Up Synthesis of Metalated Carbyne. *J. Am. Chem. Soc.* **138**, 1106–1109 (2016).
[32] N. Pavliček, B. Schuler, S. Collazos, N. Moll, D. Pérez, E. Guitián, G. Meyer, D. Peña, L. Gross, On-surface generation and imaging of arynes by atomic force microscopy. *Nat. Chem.* **7**, 623–628 (2015).
[33] F. Mohn, J. Repp, L. Gross, G. Meyer, M. S. Dyer, M. Persson, Reversible bond formation in a gold-atom-organic-molecule complex as a molecular switch. *Phys. Rev. Lett.* **105**, 266102

(2010).
[34] B. Schuler, S. Collazos, L. Gross, G. Meyer, D. Pérez, E. Guitián, D. Peña, From perylene to a 22-ring aromatic hydrocarbon in one-pot. *Angew. Chemie.* **53**, 9004–9006 (2014).
[35] B. Schuler, S. Fatayer, F. Mohn, N. Moll, N. Pavliček, G. Meyer, D. Peña, L. Gross, Reversible Bergman cyclization by atomic manipulation. *Nat. Chem.* **8**, 220–224 (2016).
[36] J. Krüger, N. Pavliček, J. M. Alonso, D. Pérez, E. Guitián, T. Lehmann, G. Cuniberti, A. Gourdon, G. Meyer, L. Gross, F. Moresco, D. Peña, Tetracene Formation by On-Surface Reduction. *ACS Nano.* **10**, 4538–4542 (2016).
[37] N. Kocić, X. Liu, S. Chen, S. Decurtins, O. Krejčí, P. Jelínek, J. Repp, S.-X. Liu, Control of Reactivity and Regioselectivity for On-Surface Dehydrogenative Aryl–Aryl Bond Formation. *J. Am. Chem. Soc.* **138**, 5585–5593 (2016).
[38] Y. He, M. Garnica, F. Bischoff, J. Ducke, M.-L. Bocquet, M. Batzill, W. Auwärter, J. V. Barth, Fusing tetrapyrroles to graphene edges by surface-assisted covalent coupling. *Nat. Chem.* **9**, 1–6 (2016).
[39] L. Bartels, G. Meyer, K.-H. Rieder, Controlled vertical manipulation of single CO molecules with the scanning tunneling microscope: A route to chemical contrast. *Appl. Phys. Lett.* **71**, 213 (1997).
[40] Z. Sun, M. P. Boneschanscher, I. Swart, D. Vanmaekelbergh, P. Liljeroth, Quantitative Atomic Force Microscopy with Carbon Monoxide Terminated Tips. *Phys. Rev. Lett.* **106**, 46104 (2011).
[41] L. Bartels, G. Meyer, K.-H. Rieder, D. Velic, E. Knoesel, A. Hotzel, M. Wolf, G. Ertl, Dynamics of Electron-Induced Manipulation of Individual CO Molecules on Cu(111). *Phys. Rev. Lett.* **80**, 2004–2007 (1998).
[42] M. Ellner, N. Pavliček, P. Pou, B. Schuler, N. Moll, G. Meyer, L. Gross, R. Peréz, The Electric Field of CO Tips and Its Relevance for Atomic Force Microscopy. *Nano Lett.* **16**, 1974–1980 (2016).
[43] C.-S. Guo, M. a. Van Hove, R.-Q. Zhang, C. Minot, Prospects for Resolving Chemical Structure by Atomic Force Microscopy: A First-Principles Study. *Langmuir*. **26**, 16271–16277 (2010).
[44] F. Mohn, B. Schuler, L. Gross, G. Meyer, Different tips for high-resolution atomic force microscopy and scanning tunneling microscopy of single molecules. *Appl. Phys. Lett.* **102**, 73109 (2013).
[45] J. van der Lit, F. Di Cicco, P. Hapala, P. Jelinek, I. Swart, Submolecular Resolution Imaging of Molecules by Atomic Force Microscopy: The Influence of the Electrostatic Force. *Phys. Rev. Lett.* **116**, 96102 (2016).
[46] A. Sweetman, M. A. Rashid, S. P. Jarvis, J. L. Dunn, P. Rahe, P. Moriarty, Visualizing the orientational dependence of an intermolecular potential. *Nat. Commun.* **7**, 10621 (2016).
[47] C. Wagner, M. F. B. Green, P. Leinen, T. Deilmann, P. Krüger, M. Rohlfing, R. Temirov, F. S. Tautz, Scanning Quantum Dot Microscopy. *Phys. Rev. Lett.* **115**, 26101 (2015).
[48] H. Mönig, D. R. Hermoso, O. Díaz Arado, M. Todorović, A. Timmer, S. Schüer, G. Langewisch, R. Pérez, H. Fuchs, Submolecular Imaging by Noncontact Atomic Force Microscopy with an Oxygen Atom Rigidly Connected to a Metallic Probe. *ACS Nano.* **10**, 1201–1209 (2016).
[49] N. Moll, L. Gross, F. Mohn, A. Curioni, G. Meyer, A simple model of molecular imaging with noncontact atomic force microscopy. *New J. Phys.* **14**, 83023 (2012).
[50] A. M. Sweetman, S. P. Jarvis, H. Sang, I. Lekkas, P. Rahe, Y. Wang, J. Wang, N. R. Champness, L. Kantorovich, P. Moriarty, Mapping the force field of a hydrogen-bonded assembly. *Nat. Commun.* **5**, 1–7 (2014).

[51] S. P. Jarvis, A. M. Sweetman, I. Lekkas, N. R. Champness, L. Kantorovich, P. Moriarty, Simulated structure and imaging of NTCDI on Si(1 1 1)-7 × 7 : a combined STM, NC-AFM and DFT study. *J. Phys. Condens. Matter.* **27**, 54004 (2015).
[52] L. Gross, F. Mohn, N. Moll, B. Schuler, A. Criado, E. Guitian, D. Pena, A. Gourdon, G. Meyer, Bond-Order Discrimination by Atomic Force Microscopy. *Science.* **337**, 1326–1329 (2012).
[53] P. Hapala, G. Kichin, C. Wagner, F. S. Tautz, R. Temirov, P. Jelínek, Mechanism of high-resolution STM/AFM imaging with functionalized tips. *Phys. Rev. B.* **90**, 85421 (2014).
[54] P. Hapala, R. Temirov, F. S. Tautz, P. Jelínek, Origin of High-Resolution IETS-STM Images of Organic Molecules with Functionalized Tips. *Phys. Rev. Lett.* **113**, 226101 (2014).
[55] M. P. Boneschanscher, S. K. Hämäläinen, P. Liljeroth, I. Swart, Sample Corrugation Affects the Apparent Bond Lengths in Atomic Force Microscopy. *ACS Nano.* **8**, 3006–3014 (2014).
[56] C.-S. Guo, M. a. Van Hove, X. Ren, Y. Zhao, High-Resolution Model for Noncontact Atomic Force Microscopy with a Flexible Molecule on the Tip Apex. *J. Phys. Chem. C.* **119**, 1483–1488 (2015).
[57] Y. Sakai, A. J. Lee, J. R. Chelikowsky, First-Principles Atomic Force Microscopy Image Simulations with Density Embedding Theory. *Nano Lett.* **16**, 3242–3246 (2016).
[58] A. J. Lee, Y. Sakai, M. Kim, J. R. Chelikowsky, Repulsive tip tilting as the dominant mechanism for hydrogen bond-like features in atomic force microscopy imaging. *Appl. Phys. Lett.* **108** (2016).
[59] M. Neu, N. Moll, L. Gross, G. Meyer, F. J. Giessibl, J. Repp, Image correction for atomic force microscopy images with functionalized tips. *Phys. Rev. B.* **89**, 205407 (2014).
[60] C. Weiss, C. Wagner, R. Temirov, F. S. Tautz, Direct Imaging of Intermolecular Bonds in Scanning Tunneling Microscopy. *J. Am. Chem. Soc.* **132**, 11864–11865 (2010).
[61] C. Weiss, C. Wagner, C. Kleimann, M. Rohlfing, F. S. Tautz, R. Temirov, Imaging Pauli Repulsion in Scanning Tunneling Microscopy. *Phys. Rev. Lett.* **105**, 86103 (2010).
[62] N. Moll, B. Schuler, S. Kawai, F. Xu, L. Peng, A. Orita, J. Otera, A. Curioni, M. Neu, J. Repp, G. Meyer, L. Gross, Image Distortions of a Partially Fluorinated Hydrocarbon Molecule in Atomic Force Microscopy with Carbon Monoxide Terminated Tips. *Nano Lett.* **14**, 6127–6131 (2014).
[63] J. Zhang, P. Chen, B. Yuan, W. Ji, Z. Cheng, X. Qiu, Real-Space Identification of Intermolecular Bonding with Atomic Force Microscopy. *Science.* **342**, 611–614 (2013).
[64] S. P. Jarvis, M. A. Rashid, A. Sweetman, J. Leaf, S. Taylor, P. Moriarty, J. Dunn, Intermolecular artifacts in probe microscope images of C_{60} assemblies. *Phys. Rev. B.* **92**, 241405 (2015).
[65] C.-S. Guo, X. Xin, M. A. Van Hove, X. Ren, Y. Zhao, Origin of the Contrast Interpreted as Intermolecular and Intramolecular Bonds in Atomic Force Microscopy Images. *J. Phys. Chem. C.* **119**, 150611095359009 (2015).
[66] S. Kawai, A. Sadeghi, F. Xu, L. Peng, A. Orita, J. Otera, S. Goedecker, E. Meyer, Extended Halogen Bonding between Fully Fluorinated Aromatic Molecules. *ACS Nano.* **9**, 2574–2583 (2015).
[67] C. Moreno, O. Stetsovych, T. K. Shimizu, O. Custance, Imaging Three-Dimensional Surface Objects with Submolecular Resolution by Atomic Force Microscopy. *Nano Lett.* **15**, 2257–2262 (2015).
[68] Y. Sugimoto, P. Pou, M. Abe, P. Jelinek, R. Pérez, S. Morita, O. Custance, Chemical identification of individual surface atoms by atomic force microscopy. *Nature.* **446**, 64–67 (2007).
[69] Y. Sugimoto, T. Namikawa, M. Abe, S. Morita, Mapping and imaging for rapid atom discrimination: A study of frequency modulation atomic force microscopy. *Appl. Phys. Lett.*

94, 23108 (2009).
[70] R. Hoffmann, D. Weiner, a. Schirmeisen, a. Foster, Sublattice identification in noncontact atomic force microscopy of the NaCl(001) surface. *Phys. Rev. B.* **80**, 115426 (2009).
[71] M. Telychko, P. Mutombo, P. Merino, P. Hapala, M. Ondráček, F. C. Bocquet, J. Sforzini, O. Stetsovych, M. Vondráček, P. Jelínek, M. Švec, Electronic and Chemical Properties of Donor, Acceptor Centers in Graphene. *ACS Nano.* **9**, 9180–9187 (2015).
[72] F. Mohn, L. Gross, G. Meyer, Measuring the short-range force field above a single molecule with atomic resolution. *Appl. Phys. Lett.* **99**, 53106 (2011).
[73] B. Schuler, W. Liu, A. Tkatchenko, N. Moll, G. Meyer, A. Mistry, D. Fox, L. Gross, Adsorption Geometry Determination of Single Molecules by Atomic Force Microscopy. *Phys. Rev. Lett.* **111**, 106103 (2013).
[74] M. Nonnenmacher, M. P. O'Boyle, H. K. Wickramasinghe, Kelvin probe force microscopy. *Appl. Phys. Lett.* **58**, 2921 (1991).
[75] K. Okamoto, K. Yoshimoto, Y. Sugawara, S. Morita, KPFM imaging of Si(1 1 1)-Sb surface for atom distinction using NC-AFM. *Appl. Surf. Sci.* **210**, 128–133 (2003).
[76] L. Gross, B. Schuler, F. Mohn, N. Moll, N. Pavliček, W. Steurer, I. Scivetti, K. Kotsis, M. Persson, G. Meyer, Investigating atomic contrast in atomic force microscopy and Kelvin probe force microscopy on ionic systems using functionalized tips. *Phys. Rev. B.* **90**, 155455 (2014).
[77] L. Gross, F. Mohn, P. Liljeroth, J. Repp, F. J. Giessibl, G. Meyer, Measuring the Charge State of an Adatom with Noncontact Atomic Force Microscopy. *Science.* **324**, 1428–1431 (2009).
[78] F. Mohn, L. Gross, N. Moll, G. Meyer, Imaging the charge distribution within a single molecule. *Nat. Nanotechnol.* **7**, 227–231 (2012).
[79] L. Nony, A. S. Foster, F. Bocquet, C. Loppacher, Understanding the Atomic-Scale Contrast in Kelvin Probe Force Microscopy. *Phys. Rev. Lett.* **103**, 36802 (2009).
[80] B. Schuler, S. Liu, Y. Geng, S. Decurtins, Contrast formation in Kelvin probe force microscopy of single π-conjugated molecules. *Nano Lett.* **14**, 3342–6 (2014).
[81] F. Albrecht, J. Repp, M. Fleischmann, M. Scheer, M. Ondráček, P. Jelínek, Probing Charges on the Atomic Scale by Means of Atomic Force Microscopy. *Phys. Rev. Lett.* **115**, 76101 (2015).

3

Intermolecular contrast in AFM images without intermolecular bonds

abstract

Intermolecular features in atomic force microscopy images of organic molecules have been ascribed to intermolecular bonds. A recent theoretical study by Hapala *et al.*[1] showed that these features can also be explained by the flexibility of molecule-terminated tips. We probe this effect by carrying out atomic force microscopy experiments on a model system that contains regions where intermolecular bonds should and should not exist between close-by molecules. Intermolecular features are observed in both regions, demonstrating that intermolecular contrast cannot be directly interpreted as intermolecular bonds.

based on

Sampsa K. Hämäläinen, Nadine van der Heijden, Joost van der Lit, Stephan den Hartog, Peter Liljeroth, and Ingmar Swart, *Physical Review Letters* **113**, 186102 (2014)

3.1 Introduction

The use of molecule-modified tips in noncontact atomic force microscopy (AFM) has enabled the visualization of the chemical structure of molecules with unprecedented resolution.[2–4] Molecule-terminated tips have also been used to probe the bond orders in conjugated molecules and to map the charge distribution inside a molecule.[5,6] Recently, even intermolecular features assigned to hydrogen bonds have been reported.[7,8] According to the IUPAC definition,[9] hydrogen bonds primarily have an electrostatic origin and may include some covalent character and other attractive interactions. It is not clear why these should yield significant repulsive contrast in AFM.[1,8] As AFM images with sub-molecular resolution were obtained with molecule-modified tips, the tip flexibility has to be considered for a quantitative understanding of the results.[5,10–14]

Ab initio calculations, *e.g.*, by density functional theory (DFT), of the CO tip-substrate system are hampered by the fact that the exact atomic structure of the metal tip behind the CO molecule is unknown. This affects, for example, the calculated lateral force constant. On the other hand, it has been demonstrated that a molecular mechanics approach is sufficient for a quantitative understanding of the contrast formation in the AFM images.[11] The AFM contrast over the bonds is caused by the presence of a saddle surface set up by the spherical potentials from the nearby atoms. As the tip-sample distance is decreased, the CO flexibility causes an apparent sharpening of the bonds.[5,11] A similar mechanism should operate irrespective of the origin of the saddle surface in the interaction potential landscape. For example, intramolecular features that do not correspond to chemical bonds have been observed.[15] Recent computational work by Hapala *et al.*[1] suggests that the intermolecular features observed in AFM are not related to actual hydrogen bonds, but are rather caused by the CO flexibility and the shape of the potential landscape between the molecules. The same mechanism was shown to be responsible for the observed contrast in scanning tunneling hydrogen microscopy (STHM) and in inelastic tunneling probe microscopy.[1,16–19]

Despite the compelling arguments in favor of the intermolecular features having been caused by the CO flexibility, the systems considered thus far also had hydrogen bonds in the positions of the enhanced AFM contrast. This makes it difficult to

establish the origin of intermolecular contrast in AFM images. In this chapter, we focus on a molecular system, where four bis(para-pyridyl)acetylene (BPPA) molecules form a tetramer stabilized by hydrogen bonds. This results in two nitrogen atoms from neighboring molecules being forced close together without chemical or hydrogen bonds being formed between them. We experimentally show that an apparent intermolecular bond shows up in AFM images where no bond exists. We corroborate these experiments using a molecular mechanics model and quantitatively match the observed contrast with the expected response caused by the flexibility of the CO molecule at the tip apex.

3.2 Experimental method

The BPPA molecules were synthesized according to reference [20]. Samples were prepared by evaporating the BPPA molecules from a Knudsen cell-type evaporator onto a Au(111) single crystal, cleaned by sputtering-annealing cycles. After preparation, the sample was inserted into a low-temperature STM/AFM (T = 4.8 K, Omicron LT-STM/qPlus AFM), housed within the same ultrahigh vacuum system (base pressure $\sim 10^{-10}$ mbar). We used a qPlus sensor with a resonance frequency f_0 of 24 454 Hz, a quality factor of > 10 000, spring constant k = 1800 N/m, and a peak-to-peak oscillation amplitude of ~1.7 Å (amplitude A = 0.85 Å). Picking up an individual carbon monoxide molecule, to functionalize the tip apex, was carried out as described previously.[2,21] For the constant-height AFM images, the tip-sample distance was typically decreased by a few tens of pm (indicated in the figure captions) with respect to the STM set point (V = 0.1 V, I = 10 pA) after switching off the feedback. To eliminate creep and minimize drift, the tip was allowed to stabilize for 12 hours before AFM images were acquired (recorded with V = 0 V).

3.3 Experimental results and DFT simulations

Upon adsorption on the Au(111) substrate, the BPPA molecules self-assemble into several different structures. Figure 3.1(a) shows one of the more common structures. It consists of BPPA tetramers, which are held together by C–H···N hydrogen bonds between the electronegative pyridinic nitrogens and the hydrogen atoms of the

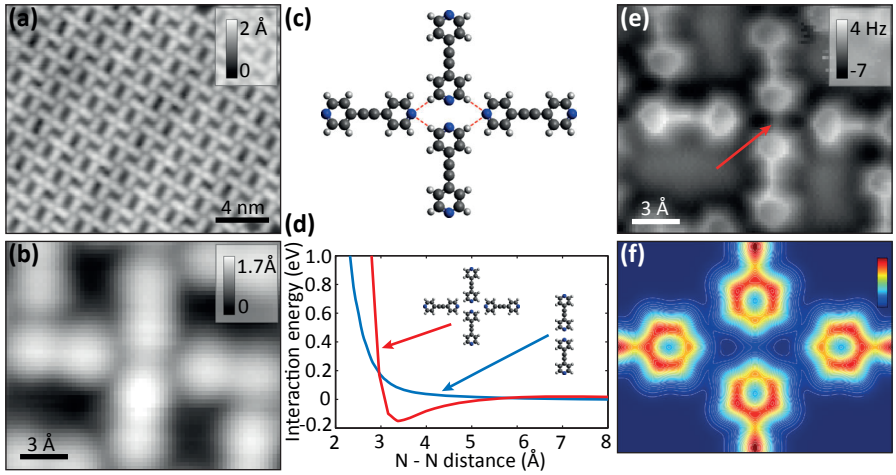

Figure 3.1 (a) Overview STM image of the self-assembled BPPA molecules. **(b)** STM image of a BPPA tetramer. **(c)** Schematic of the tetramer. **(d)** Energy-distance curve for two BPPA molecules (blue line) and for a tetramer (red line). **(e)** AFM image of the tetramer taken with a CO-tip, showing apparent intermolecular bonds. **(f)** Total electron density 3.1 Å above the molecular plane given by DFT.

pyridine rings, see figure 3.1(b). A ball-and-stick model of these tetramers is given in figure 3.1(c). Within the tetramer, the hydrogen bonds, red dashed lines in figure 3.1(c), force the nitrogens of the two opposing BPPA molecules close to each other ($d_{N\text{-}N} \approx 3$ Å).

We can exclude the presence of coordinating Au atoms in the middle of the tetramers as the distance between the molecules is much smaller than expected for 2 times a typical Au–N bond.[22] In addition, if present, a Au atom should be visible in the AFM image, even if it is located below the plane of the molecules.[23]

We have analyzed the structure of the tetramer by DFT calculations of the molecules in the absence of the substrate. Omission of the substrate is justified as the molecules are expected to interact weakly with the Au(111) surface.[24,25] We used dispersion corrected GGA (PBE-D3) and hybrid functionals (B3LYP-D3) in combination with a TZ2P basis set as implemented in ADF.[26] The energy vs distance curve of a dimer shown in figure 3.1(d), displays pure repulsive behavior, consistent with the expected

repulsive interaction between the electron lone pairs of the pyridinic nitrogens. In contrast, for the tetramer, we find a binding energy of −151 meV (PBE-D3). Hence, the tetramer represents a stable configuration. The simulated distance between the nitrogen atoms (3.3 Å) is in reasonable agreement with the experimental value (3.0 Å).

3.4 Contrast in regions between molecules

The constant-height AFM image of a BPPA tetramer taken with a CO terminated tip in figure 3.1(e), shows weak contrast on the C–H···N bond, similar to the recently published results on imaging hydrogen bonds with AFM.[7,8] However, there is also contrast in the region between the opposing nitrogen atoms (indicated by the arrow in figure 3.1(e), despite the absence of a bond between these atoms.

It has been proposed that the atomic scale contrast can be modeled by considering only the total electron density at the position of the AFM tip apex.[27] However, as discussed previously,[8] this is not sufficient to explain the AFM response even in the case of a rigid tip apex. Additional effects, such as the depletion of the charge density due to the tip-sample interaction may need to be taken into account.[8] The discrepancy between the total electron density and the AFM response is also seen in our data. Figure 3.1(f) shows the total electron density 3.1 Å above the plane of the molecules. As expected, the electron density in the region between the molecules is much lower than in between atoms. In the conventional model of the AFM imaging with CO terminated tips,[27] this should translate in a much weaker intermolecular contrast, contrary to what we observe experimentally. We will show below that the contrast in the actual measurement can be understood by considering the bending of the CO molecule at the tip apex.[1,11]

3.5 Molecular mechanics simulations

We use a model based on molecular mechanics,[11] similar to the model used by Hapala *et al.*[1] The tip is modeled in two parts: a macroscopic sphere representing the metallic bulk tip and a CO molecule which is allowed to move on a lever attached to

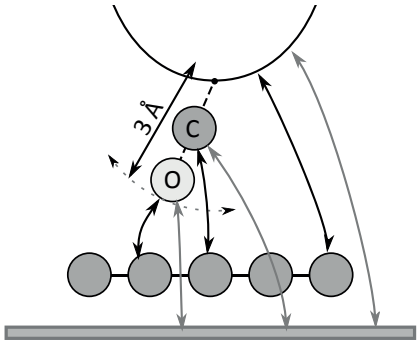

Figure 3.2 Illustration of the tip model used in the simulation. The arrows refer to the different force components that either are functions of the (*x*,*y*,*z*)-coordinates (black) or only depend on the *z* coordinate (gray).

the apex of the sphere. The macroscopic sphere and the substrate under the molecules were treated on a continuum level, while the CO and the molecules were treated atomistically as shown schematically in figure 3.2. We use a Lennard-Jones-type 9-6 potential for all the interatomic interactions with the parameters rescaled from the 12-6 potential from reference [28] such that the position and depth of the potential minimum remained constant. We tested different forms of the repulsive interaction; the exact form has only a very minor effect on the simulated AFM response. While electrostatic interactions have been shown to be relevant with CO terminated tips,[29,30] we neglect them in the present case as the electrostatic force components would only cause the location of the saddle point in the interaction potential surface to shift along the hydrogen bond and would not have an effect on the AFM contrast across the bond. The CO was relaxed self-consistently at each point before calculating the forces. The frequency shift Δf at a given height was calculated taking into account the finite oscillation amplitude used in the experiment.[31]

Figure 3.3(a) shows a calculated constant-height AFM image of two carbon atoms 3 Å apart with a rigid CO molecule on the tip apex. As expected, the resulting Δf image shows two spherically symmetric maxima centered on top of the atoms. The interaction potential felt by the CO molecule is plotted in figure 3.3(b). Letting the CO respond to the lateral forces by bending has a dramatic influence on the simulated AFM image, see figure 3.3(c). The two atoms produce a saddle surface between them, which causes the CO to bend away from the line connecting the atoms. The bending

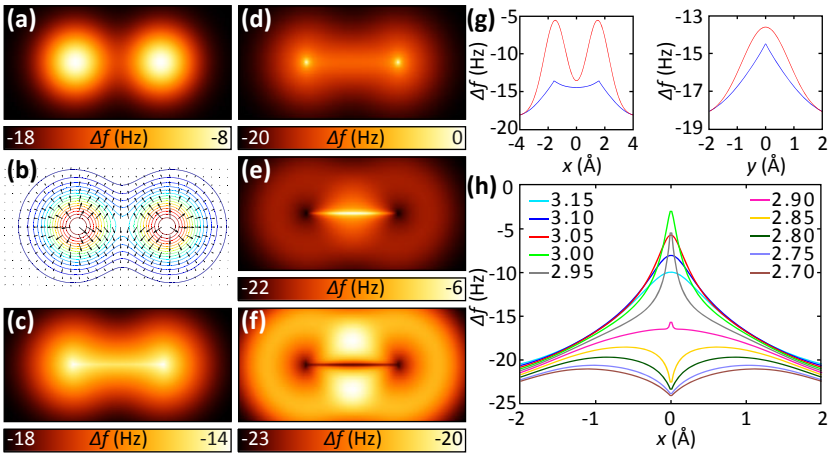

Figure 3.3 (a) Simulated constant height AFM image (tip height 2.9 Å) with a rigid CO tip of two carbon atoms 3 Å apart. **(b)** CO potential on top of the atoms (contour) and the bending of the CO in the simulation. **(c)** Simulated constant-height AFM image with a flexible CO tip (k_{tip} = 0.6 N/m) at the same tip height as in panel (a). **(g)** Cross sections along and across the apparent bond, respectively. **(d-f)** Δf images calculated at the low amplitude limit at different heights. **(h)** Δf cross sections across the apparent bond between the atoms at the low-amplitude limit. All tip-sample distances are measured from the oxygen of the CO at the lowest point of oscillation.

of the CO causes a decrease in the measured Δf signal. Thus, the sharp contrast along the line connecting the atoms is the result of the reduced repulsion away from the symmetry line rather than an increased repulsion between the atoms (due to, *e.g.*, increased electron density). This is illustrated in figure 3.3(g), which shows cross sections of the Δf surfaces along (x-direction) and across (y-direction) a line between the atoms for a rigid (red) and a flexible (blue) CO-tip.

This is the essential effect behind the very sharp contrast obtained in AFM with CO terminated tips on molecules where the bonds between the atoms appear unphysically sharp.[5,11] The sharpening will happen on any saddle-like potential surface: it does not require actual electron density between the atoms, *i.e.* a bond. This is clearly shown in the simulation in figure 3.2(c), where no bond exists as the CO interaction with the atoms is modeled by the L-J potential. Consequently, the CO bending will pick up the shape of the potential energy surface between two molecules, and symmetry lines

will show with enhanced contrast. This means that intermolecular contrast cannot be taken as a proof of the existence of an intermolecular bond.[1]

3.6 Height dependence of apparent bonds

In order to verify this effect experimentally, we have studied the evolution of the intermolecular features within the BPPA tetramer as a function of the tip-sample distance. Figure 3.4 shows a set of constant-height AFM images taken with a CO terminated tip at different heights above the BPPA tetramer junction with a comparison to the images produced by our simple CO-tip model. In neither the experiments nor in the simulations are intermolecular bond-like features observed for large tip-sample distances, as the CO never reaches the repulsive regime. Taking the tip closer, lines start to appear both between the two opposing nitrogens and on the actual hydrogen bonds holding the tetramer together. The contrast first appears between the two opposing nitrogens as they are closer to one another and hence, the saddle surface is formed there first. Upon approaching the tip further, contrast also appears in the region of the hydrogen bonds that hold the tetramer together. At the smallest tip-sample distance, the CO bending starts to dictate the contrast formation. Surprisingly, the contrast on the intermolecular lines becomes almost indistinguishable from the contrast on the acetylene moieties connecting the pyridine rings in the BPPA molecule, both in experiment and simulation.

The sharp contrast produced by the bending of the CO molecule can easily be incorrectly interpreted as overly high resolution. In reality, the bending of the CO sets a limit to the resolution that can be obtained in AFM with flexible tips. As can be seen in figure 3.2(d-f, h), the simulated low-amplitude Δf signal starts to level out and invert when the tip is pushed further in. The height at which this happens is defined by the stiffness of the tip. This results in a loss of contrast between repulsion maxima (*e.g.*, on top of atoms) and other areas of repulsion when integrating over the tip oscillation amplitude. This eventually renders all saddle surfaces and atoms equally bright in the Δf image irrespective of the magnitude of the repulsion, or electron density. At this point, the contrast formation in AFM is dictated by the lateral stiffness of the CO and is no longer related to the magnitude of the tip-sample interaction.

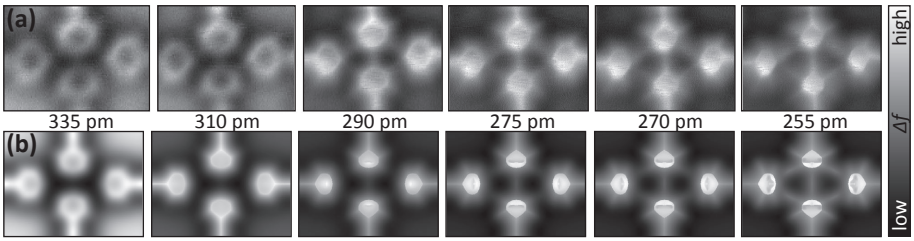

Figure 3.4 (a) Experimental constant-height AFM images with a CO tip taken at different heights on top of the tetramer junction showing the appearance of both C–H···N and N–N intermolecular contrast at close tip-sample distances. **(b)** Simulated constant-height AFM images with a flexible CO tip (k_{tip} = 0.6 N/m) at the given heights showing the appearance of the same intermolecular contrast. The relative height scale is the same in the experimental and simulated images with the simulated height of 385 pm matching the tunneling conditions of 10 pA at 0.1 V. The heights correspond to the lowest point of the tip oscillation.

This work and the work by Hapala *et al.*[1] raises an important question: to what extent is tip bending responsible not just for the intermolecular, but also for the intramolecular contrast in planar molecules? In other words: can AFM image bonds, or is the technique only sensitive to the potential energy landscape originating from (spherically symmetric) potentials of the atoms in the molecule? A covalent bond is a region of enhanced electron density between two atoms. If electron density would be the only contribution to the contrast, it is very difficult to understand the similar contrast between atoms (where the electron density is much higher) and bonds. Indeed, tip relaxations are essential to reproduce experimentally observed intramolecular contrast.[1,15] This suggests that tip flexibility also plays a dominant role in imaging intramolecular bonds.

As discussed in the introduction, electrostatic interactions and small changes in electron density are not expected to result in repulsive contrast in AFM images. In order to see hydrogen bonds experimentally, one would need to be able to resolve the extra electron density caused by the bonding. This would require a quantitative estimate of the electron density on the atoms in order to extrapolate onto the region of the hydrogen bonds. This is experimentally very demanding as the tip flexibility will cause loss of contrast on the atoms at these small tip-sample distances.

3.7 Conclusion

In conclusion, we present an AFM measurement of BPPA tetramers using a CO terminated tip. Identical intermolecular contrast appears both on top of the hydrogen bonds and between two pyridinic nitrogens which do not bond. We show that the CO bending causes two effects which enhance the apparent intermolecular features in AFM. The CO bends away from the ridges in the saddle surface of the interaction potential, which produces sharp lines between nearby atoms. At the same time, bending away from the actual atoms decreases the Δf signal on top of the molecules, which increases the relative intensity on the intermolecular features. This means that the contrast on both real and apparent bonds is mostly a result of the bending of the probe molecule on the AFM tip. Hence, intermolecular contrast in AFM images does not necessarily represent intermolecular bonds.

3.8 References

[1] P. Hapala, G. Kichin, C. Wagner, F. S. Tautz, R. Temirov, P. Jelínek, Mechanism of high-resolution STM/AFM imaging with functionalized tips. *Phys. Rev. B.* **90**, 85421 (2014).

[2] L. Gross, F. Mohn, N. Moll, P. Liljeroth, G. Meyer, The Chemical Structure of a Molecule Resolved by Atomic Force Microscopy. *Science.* **325**, 1110–1114 (2009).

[3] L. Gross, F. Mohn, N. Moll, G. Meyer, R. Ebel, W. M. Abdel-Mageed, M. Jaspars, Organic structure determination using atomic-resolution scanning probe microscopy. *Nat. Chem.* **2**, 821–825 (2010).

[4] D. G. de Oteyza, P. Gorman, Y.-C. Chen, S. Wickenburg, A. Riss, D. J. Mowbray, G. Etkin, Z. Pedramrazi, H.-Z. Tsai, A. Rubio, M. F. Crommie, F. R. Fischer, Direct Imaging of Covalent Bond Structure in Single-Molecule Chemical Reactions. *Science.* **340**, 1434–1437 (2013).

[5] L. Gross, F. Mohn, N. Moll, B. Schuler, A. Criado, E. Guitian, D. Pena, A. Gourdon, G. Meyer, Bond-Order Discrimination by Atomic Force Microscopy. *Science.* **337**, 1326–1329 (2012).

[6] F. Mohn, L. Gross, N. Moll, G. Meyer, Imaging the charge distribution within a single molecule. *Nat. Nanotechnol.* **7**, 227–231 (2012).

[7] J. Zhang, P. Chen, B. Yuan, W. Ji, Z. Cheng, X. Qiu, Real-Space Identification of Intermolecular Bonding with Atomic Force Microscopy. *Science.* **342**, 611–614 (2013).

[8] A. M. Sweetman, S. P. Jarvis, H. Sang, I. Lekkas, P. Rahe, Y. Wang, J. Wang, N. R. Champness, L. Kantorovich, P. Moriarty, Mapping the force field of a hydrogen-bonded assembly. *Nat. Commun.* **5,** 1–7 (2014).

[9] E. Arunan, G. R. Desiraju, R. A. Klein, J. Sadlej, S. Scheiner, I. Alkorta, D. C. Clary, R. H. Crabtree, J. J. Dannenberg, P. Hobza, H. G. Kjaergaard, A. C. Legon, B. Mennucci, D. J. Nesbitt, Definition of the hydrogen bond (IUPAC Recommendations 2011). *Pure Appl. Chem.* **83**, 1637–1641 (2011).

[10] Z. Sun, M. P. Boneschanscher, I. Swart, D. Vanmaekelbergh, P. Liljeroth, Quantitative Atomic Force Microscopy with Carbon Monoxide Terminated Tips. *Phys. Rev. Lett.* **106**, 46104

(2011).
[11] M. P. Boneschanscher, S. K. Hämäläinen, P. Liljeroth, I. Swart, Sample Corrugation Affects the Apparent Bond Lengths in Atomic Force Microscopy. *ACS Nano.* **8**, 3006–3014 (2014).
[12] A. J. Weymouth, T. Hofmann, F. J. Giessibl, Quantifying Molecular Stiffness and Interaction with Lateral Force Microscopy. *Science.* **343**, 1120–1122 (2014).
[13] M. Neu, N. Moll, L. Gross, G. Meyer, F. J. Giessibl, J. Repp, Image correction for atomic force microscopy images with functionalized tips. *Phys. Rev. B.* **89**, 205407 (2014).
[14] N. Moll, B. Schuler, S. Kawai, F. Xu, L. Peng, A. Orita, J. Otera, A. Curioni, M. Neu, J. Repp, G. Meyer, L. Gross, Image Distortions of a Partially Fluorinated Hydrocarbon Molecule in Atomic Force Microscopy with Carbon Monoxide Terminated Tips. *Nano Lett.* **14**, 6127–6131 (2014).
[15] N. Pavliček, B. Fleury, M. Neu, J. Niedenfu, C. Herranz-lancho, M. Ruben, J. Repp, Atomic Force Microscopy Reveals Bistable Configurations of Dibenzo[a,h] thianthrene and their Interconversion Pathway. *Phys. Rev. Lett.* **108**, 86101 (2012).
[16] R. Temirov, S. Soubatch, O. Neucheva, A. C. Lassise, F. S. Tautz, A novel method achieving ultra-high geometrical resolution in scanning tunnelling microscopy. *New J. Phys.* **10**, 53012 (2008).
[17] C. Weiss, C. Wagner, R. Temirov, F. S. Tautz, Direct Imaging of Intermolecular Bonds in Scanning Tunneling Microscopy. *J. Am. Chem. Soc.* **132**, 11864–11865 (2010).
[18] C. -l. Chiang, C. Xu, Z. Han, W. Ho, Real-space imaging of molecular structure and chemical bonding by single-molecule inelastic tunneling probe. *Science.* **344**, 885–888 (2014).
[19] P. Hapala, R. Temirov, F. S. Tautz, P. Jelínek, Origin of High-Resolution IETS-STM Images of Organic Molecules with Functionalized Tips. *Phys. Rev. Lett.* **113**, 226101 (2014).
[20] N. R. Champness, A. N. Khlobystov, A. G. Majuga, M. Schröder, N. V. Zyk, An Improved Preparation of 4-Ethynylpyridine and its Application to the Synthesis of Linear Bipyridyl Ligands. *Tetrahedrom Lett.* **40**, 5413–5416 (1999).
[21] L. Bartels, G. Meyer, K.-H. Rieder, D. Velic, E. Knoesel, A. Hotzel, M. Wolf, G. Ertl, Dynamics of Electron-Induced Manipulation of Individual CO Molecules on Cu(111). *Phys. Rev. Lett.* **80**, 2004–2007 (1998).
[22] F. Mohr, Gold Chemistry: Applications and Future Directions in the Life Sciences. *Wiley-VCH*, Weinheim (2009).
[23] F. Albrecht, M. Neu, C. Quest, I. Swart, J. Repp, Formation and Characterization of a Molecule–Metal–Molecule Bridge in Real Space. *J. Am. Chem. Soc.* **135**, 9200–9203 (2013).
[24] W.-H. Soe, C. Manzano, A. De Sarkar, N. Chandrasekhar, C. Joachim, Direct Observation of Molecular Orbitals of Pentacene Physisorbed on Au(111) by Scanning Tunneling Microscope. *Phys. Rev. Lett.* **102**, 176102 (2009).
[25] J. van der Lit, M. P. Boneschanscher, D. Vanmaekelbergh, M. Ijäs, A. Uppstu, M. Ervasti, A. Harju, P. Liljeroth, I. Swart, Suppression of electron–vibron coupling in graphene nanoribbons contacted via a single atom. *Nat. Commun.* **4**, 2023 (2013).
[26] ADF2010, SCM, Theoretical Chemistry, Vrije Universiteit, Amsterdam, The Netherlands, (available at http://www.scm.com).
[27] N. Moll, L. Gross, F. Mohn, A. Curioni, G. Meyer, The mechanisms underlying the enhanced resolution of atomic force microscopy with functionalized tips. *New J. Phys.* **12**, 125020 (2010).
[28] A.D. MacKerell, Jr. *et al.*, All-Atom Empirical Potential for Molecular Modeling and Dynamics Studies of Proteins. *J. Phys. Chem. B.* **102**, 3586–3616 (1998).

[29] M. Schneiderbauer, M. Emmrich, A. J. Weymouth, F. J. Giessibl, CO Tip Functionalization Inverts Atomic Force Microscopy Contrast via Short-Range Electrostatic Forces. *Phys. Rev. Lett.* **112**, 166102 (2014).
[30] A. Schwarz, A. Köhler, J. Grenz, R. Wiesendanger, Detecting the dipole moment of a single carbon monoxide molecule. *Appl. Phys. Lett.* **105**, 11606 (2014).
[31] F. J. Giessibl, A direct method to calculate tip–sample forces from frequency shifts in frequency-modulation atomic force microscopy. *Appl. Phys. Lett.* **78**, 123 (2001).

4

Mapping the electrostatic force field of single molecules from high-resolution scanning probe images

abstract

How electronic charge is distributed over a molecule determines to a large extent its chemical properties. Here, we demonstrate how the electrostatic force field, originating from the inhomogeneous charge distribution in a molecule, can be measured with sub-molecular resolution. We exploit the fact that distortions typically observed in high-resolution atomic force microscopy images are for a significant part caused by the electrostatic force acting between charges of the tip and the molecule of interest. By finding a geometrical transformation between two high-resolution AFM images acquired with two different tips, the electrostatic force field or potential over individual molecules and selfassemblies thereof can be reconstructed with sub-molecular resolution.

based on

Prokop Hapala, Martin Švec, Oleksandr Stetsovych, Nadine J. van der Heijden, Martin Ondráček, Joost van der Lit, Pingo Mutombo, Ingmar Swart, and Pavel Jelínek, *Nature Communications* **7**, 11560 (2016)

4.1 Introduction

Scanning probe techniques routinely provide detailed information on the electronic and geometric structure of molecules. For example, the frontier molecular orbitals,[1] the chemical structure of molecules[2–4] and bond orders[5] can be imaged. The possibility to image molecules[6] and atomic clusters[7] with nearly atomic resolution, also at elevated temperatures[8–11] provided a great stimulus for surface science.[12–17]

From the perspective of chemistry, the capability to measure the charge distribution of a molecule is extremely useful as this property determines the chemical reactivity of a molecule, as well as many other molecular properties.[18] However, imaging the charge distribution within a single molecule remains a challenge. Thus far, kelvin probe force microscopy (KPFM) is the only technique able to measure a quantity that is related to the charge distribution of an individual molecule: the local contact potential difference.[19–21] The acquisition and unambiguous interpretation of KPFM data on the atomic and sub-molecular level is a nontrivial task.[20,22–24] One of the primary difficulties is that there is no clear definition to which physical quantity (electrostatic potential, field, surface dipole or other) the detected signal should be compared (see, for example, the discussion in reference [25]). Furthermore, at the typical tip-sample distances required to obtain sub-molecular resolution in atomic force microscopy (AFM) images, the measured KPFM signal is governed by the complex interplay of local electrostatic fields of tip and sample, their mutual polarization,[26] mechanical distortions and the conductance due to overlap of molecular orbitals.[27] In this regime, the usual interpretation of KPFM data is longer valid.[28]

Very recently, two alternative techniques, scanning quantum dot microscopy (SQDM)[29] and the kelvin probe force spectroscopy (KPFS),[28] were introduced. Both methods partially solve the deficiencies of the KPFM method discussed above. Namely, SQDM is able to provide a quantitative analysis of the electrostatic potential, but only in the far distance regime, limiting the spatial resolution. The KPFS method provides high spatial resolution but suffers from the same drawback of ambiguous definition of the observable as KPFM.

As the charge distribution is to be imaged with high-resolution resolution, the use

of chemically passivated tips is essential.[30–32] Several different types of forces and processes have been identified to be important for the contrast in AFM images acquired with such tips. These include the Pauli, van der Waals and electrostatic forces, as well as the flexibility of the functionalized tip.[2,5,33–39] The latter is especially important to understand the distortions in the appearance of molecules in sub-molecular resolution images.[34,36,40–45]

Here we will show that the electrostatic forces acting between probe and an inspected molecule can significantly affect the sub-molecular contrast. Furthermore, we will show that distortions of the high-resolution images induced by the electrostatic force can be used to map the electrostatic potential of the molecule with sub-molecular resolution.

4.2 General considerations

To illustrate the central idea behind the method proposed here, we consider imaging a neutral molecule with an inhomogeneous charge distribution with a tip terminated by a positively charged flexible probe particle. The probe particle is attracted to regions of excess electron density, whereas it is repelled from regions that have a positive charge. Consequently, positively/negatively charged areas will appear smaller/larger than they really are with such a tip. The opposite tendency is true for negatively charged tips. Hence, the distortions in sub-molecular resolution AFM images acquired with charged tips carry information on the charge distribution within the molecule. Here, we demonstrate how these image distortions can be used to determine the spatial distribution of the electrostatic field above molecules with sub-molecular resolution. The technique is applied to reconstruct the local electrostatic field of both individual molecules and self-assembled monolayers.

First, let us briefly discuss the origin and character of the apparent bonds, or sharp edges, in high-resolution AFM/STM images. At close tip-sample distances, the repulsive Pauli interaction induces a significant lateral deflection of the probe particle. There is a discontinuity in the deflection above saddle points of the energy landscape as can be seen in figure 4.1 and discussed in chapter 3. The saddle points (sharp

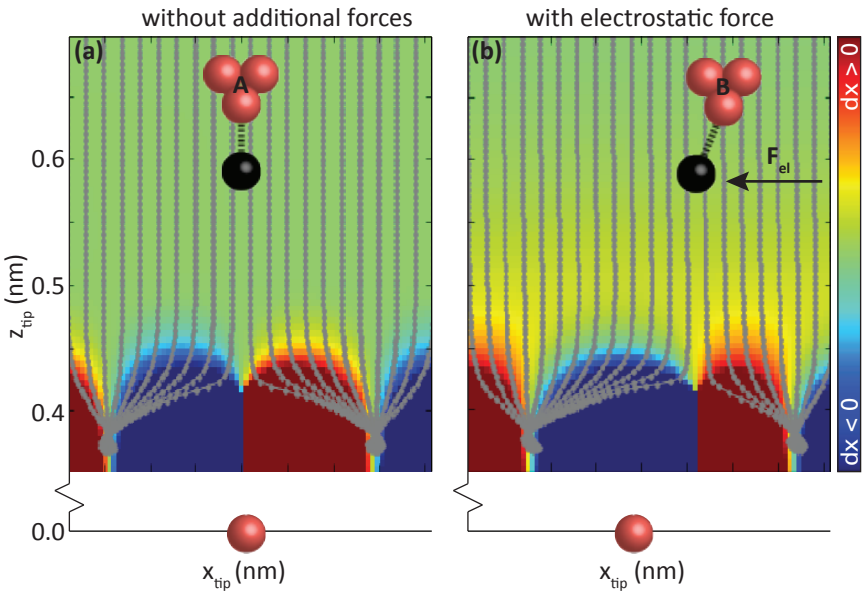

Figure 4.1 (a) Simulated deflections of the probe particle as a function of tip position. Grey lines represent the additional deflection of the probe particle with respect to its optimal configuration in far distance. The deflection of the probe particle to the left and right is indicated by blue and red, respectively. **(b)** Same as (a) but now in the presence of an additional constant lateral force.

edges) are typically present over atoms or bonds at a tip-sample distance where the Pauli repulsion fully compensates the attractive forces. Consequently, the trajectory of the probe particle is split into branches, giving rise to sharp edges.[35,38,43] Hence, the apparent bonds correspond to saddle points of the potential energy surface experienced by the probe particle at a certain tip-sample distance.

Figure 4.1(a) shows the trajectories of the probe particle, simulated using molecular mechanics, when tip approaches a one-dimensional chain of atoms separated by 2.9 Å (corresponding to the width of a typical benzene ring). The lateral deflection of the probe particle to the left and right is depicted in blue and red, respectively. Note that the trajectories of the probe particle are split into two branches. The deflection depends non-linearly on the tip height. However, the position of the sharp discontinuous boundary between bending left and right, that is, between blue and red regions, does not depend on the tip-sample distance. This is in agreement with our

experimental observation that at close tip-sample distances the apparent position of various sharp edges in AFM images do not change with distance. This finding can be rationalized by the fact that the position of sharp edges is determined by the distance where the bifurcation of the probe particle trajectory on tip approach happens. Consequently, while the lateral distortions of the probe particle may be large beyond this point, the lateral apparent position of the sharp edge remains constant.

We see clearly that the deflection dx depends non-linearly on the tip-height z_{tip} (as can be seen from both the gray-scaled trajectories and from the color-code in figure 4.1), but the position of the sharp discontinuous boundary between the left and right bending (blue and red region) does not depend on the tip-sample distance z_{tip}. This is due to the symmetry of the chosen system (the infinite chain of equidistant carbon atoms), which does not introduce any asymmetric lateral van der Waals force at large tip-sample distances. This means that the probe particle deflection dx is zero when the tip and sample are far apart. Consequently the saddle point of the potential energy surface is positioned symmetrically right on top of the center of carbon atoms.

In figure 4.1(b) we repeated the same simulation but with an additional lateral force component F_x pointing along x-axis, which can represent *e.g.* the electrostatic interaction between a charged probe particle and local surface electrostatic potential. We assume that this additional lateral force F_x induces an extra lateral deflection dx' of the probe particle, which is linearly proportional to F_x according to Hook's law $F_x = K\,dx'$ where K is the lateral bending stiffness of the probe particle attached to the tip base. Consequently the two coordinate systems of tip (x_{tip}) and the probe particle (x_{pp}) are now shifted with respect to each other and the characteristic sharp feature in AFM images appears at different positions when measured by a scanning probe.

The total lateral force F_{tot} is the sum of van der Waals forces F_{vdW}, Pauli forces F_{Pauli} and, optionally, electrostatic forces F_{el}. The presence of the lateral force Ftot induces a lateral deflection dx of the flexible probe particle with respect to the tip position x_{tip}, see figure 4.2(b-c). As long as dx is small, it is linearly proportional to F_{tot} acting on the probe particle, according to Hooke's law: $dx = F_{tot}/K$,[34,39] where K is the lateral bending stiffness of the bond between the probe particle and the tip. Variation of the

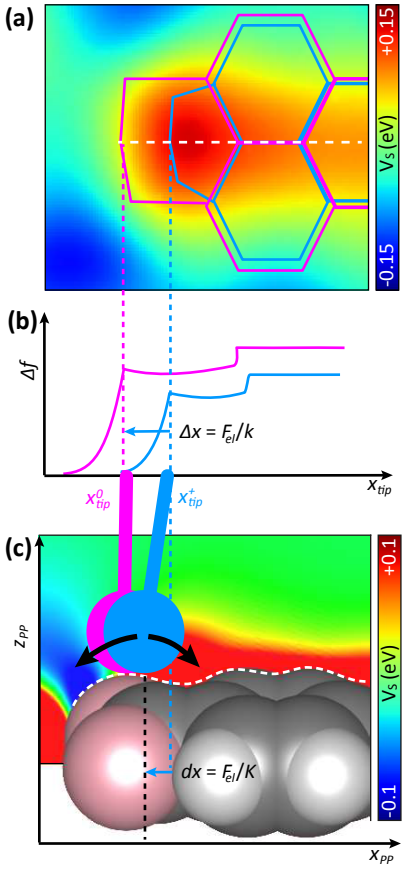

Figure 4.2 Schematic view of the impact of electrostatic forces on high-resolution AFM images. **(a)** Blue and pink lines represent the positions of sharp edges observed in high-resolution AFM images acquired using positively charged and neutral tips, respectively. Corresponding *x*,*y*-cut-plane of the Hartree potential $V_s(x,y)$ above the molecule is displayed in the background. **(b)** Variation of the frequency shift Δf as function of the tip positions for the neutral x^0_{tip} and positively charged x^+_{tip} probe particle. **(c)** The lateral relaxation Δx of the probe particle with (blue) and without (pink) an effective charge on the tip is different above a molecule due to the presence of the electrostatic force. The electrostatic force originates from the interaction between the electrostatic potential of the molecule (V_s) on the surface and the effective charge on the probe particle at its given position x_{PP}.

lateral electrostatic force F_{el} causes a shift of the characteristic feature at a different lateral tip position (indicated by x^+_{tip}) with respect to the position with the absence of the electrostatic lateral force (x^0_{tip}) as shown in figure 4.2. Consequently, the positions of the apparent bonds x_{tip} in high-resolution AFM images do not correspond to their actual positions on the surface.

From the above, it is clear that the apparent shift of the characteristic features Δx in AFM/STM images, therefore, carries information about the lateral forces F_{tot} with atomic resolution. The apparent shift is linearly related to the deflection of the probe particle from the tip base: $\Delta x = \gamma dx = \gamma(x_{tip} - x_{PP})$, see figure 4.2. Here, x_{PP} denotes the actual position of the probe particle and $\gamma \approx 2$. The value of γ is found from a hard-sphere assumption together with geometric relations, and fits well with DFT simulations.[46]

In the following discussion, we will express everything in the experimentally observable Δx instead of in dx. In this notation, Δx is linearly proportional to the lateral force: $\Delta x = F_{tot}/k$, where $k = K/\gamma$ is the effective lateral stiffness.

In our analysis of the electrostatic field, we will use the differences in the apparent positions of sharp contours recorded with two different tips. Specifically, we extract and compare the apparent positions of the same contour feature (for example, a particular atom vertex or bond edge) from two high-resolution AFM images obtained with different tips or scanning conditions (labelled tip A and tip B) at approximately the same tip-sample distances. The apparent position of features acquired with the different tips are indicated by $x_{tip,A}$ and $x_{tip,B}$. In the following, we are interested in the relative difference of the apparent positions $\delta x = x_{tip,A} - x_{tip,B}$. Because we measure the same object on the surface, the real position of any atom or bond that corresponds to a particular contour feature is the same for both images. Therefore, δx can be expressed as the difference between the image distortions in the two images of the same object:

$$\delta x = x_{tip,A} - x_{tip,B} \quad (1)$$

$$= \Delta x_A - \Delta x_B \quad (2)$$

$$= F_A/k_A - F_B/k_B \quad (3)$$

Here, F_A and F_B are the total lateral force acting on the probe particle in case A and B, respectively. Since the onset of the Pauli force is very steep only the van der Waals and electrostatic force components of the total force contribute to the apparent lateral distortions Δx. The distortion then depends linearly on the lateral van der Waals and electrostatic forces.[46]

In the following, we therefore use the following expression for the differences in the lateral distortions:

$$\delta x = \frac{F_{vdW,A} + F_{el,A}}{k_A} - \frac{F_{vdW,B} + F_{el,B}}{k_B} \quad (4)$$

In this general form, there is unfortunately no clear way how to attribute partial relative distortions to each force component, for example, to determine the lateral electrostatic force field F_{el} component only from the high-resolution images. However, under certain assumptions and/or with the help of numerical simulations this problem can be circumvented.

We will now discuss an approach to extract the lateral electrostatic force field component from equation (4). In general, the effective stiffness k and charge Q of the tips, as well as the van der Waals contributions are different for each tip. The charge of the probe particle depends on the configuration and chemical nature of the metal apex,[47] as well as how the Xe/CO is coordinated. Hence, even tips terminated with the same species can have a different charge.

First, we will consider the simplest case: two high-resolution images are acquired with nearly identical tips, for example, Xe-terminated metallic tips, differing only in their effective charge. In this case, the following approximations hold: (i) the effective lateral stiffness k of both tips is identical or very similar (that is, $k_A \approx k_B = k$); (ii) the lateral components of the van der Waals forces for tip A and B are also almost identical at a given tip-sample distance. Since both tips are used to image the same object, the surface electrostatic field E_S must be the same in both images. Under these approximations, equation (4) simplifies to:

$$\delta x = \frac{F_{el,A} + F_{el,B}}{k} \tag{5}$$

$$= \frac{Q_A - Q_B}{k} E_S \tag{6}$$

where Q_A and Q_B are the effective charges of tips A and B, respectively. This equation shows that we can obtain quantitative information about E_S directly from the difference in the image distortions. The only parameters that are needed are the effective lateral stiffness k and the difference between the effective charges Q_A and Q_B. These can be estimated for each tip from a direct comparison between experimental and simulated high-resolution AFM/STM images.[35,48] Alternatively, k can be obtained directly from experimental measurements.[49]

Next, we consider a more general case where the van der Waals contribution for the two tips is significantly different but one of the tips is neutral, that is, $Q_B \approx 0$. This would correspond to the situation where macroscopically different tips, possibly with different tip termination, are used. In this case, we obtain the following relation for the surface electrostatic field E_S:

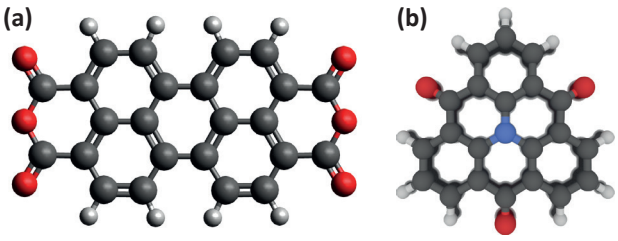

Figure 4.3 Ball-and-stick models of **(a)** perylene-3,4,9,10-tetracarboxylic dianhydride (PTCDA) and **(b)** 1,5,9-trioxo-13-azatriangulene (TOAT).

$$E_S = \frac{k_A(\delta x - \delta x_{vdW})}{Q_A} \tag{7}$$

where $\delta x_{vdW} = F_{vdW,A}/k_A - F_{vdW,B}/k_B$. The differences of the van der Waals deformation field components δx_{vdW} can be estimated from numerical simulations. We note here that the effect of the van der Waals contribution is indispensable only at the periphery of the molecule. Although it may be difficult to extract absolute values in this scenario, the overall shape of the electrostatic field is preserved.

4.3 Methods

To test our approach to measure the electrostatic field with sub-molecular resolution, we performed two different sets of experiments. First, we studied a densely packed self-assembled layer of PTCDA on Ag(111) with two differently charged but otherwise similar Xe-tips. Second, we studied individual 1,5,9-trioxo-13-azatriangulene (TOAT) molecules on Cu(111) with a neutral CO-tip and a positively charged Xe-tip. A ball-and-stick model of both molecules is shown in figure 4.3.

4.3.1 AFM/STM measurements

The PTCDA on Ag(111) experiments were carried out with a Specs LT STM/AFM with a commercially available Kolibri sensor, operating at 1.2 K in ultra-high vacuum. The Kolibri sensor parameters used in the experiment are: $f_0 \approx 985\,387$ Hz, $Q \approx 230\,000$ and $A \approx 70$ pm.

The Ag(111) surface was cleaned by repeated cycles of sputtering (Ar^+, $P_{Ar} \approx 5\times10^{-6}$ mbar, 10 min) and annealing ($T \approx 800$ K, 5 min). PTCDA was evaporated in

ultra-high vacuum ($P < 1.5 \times 10^{-9}$ mbar) for 4 min from a crucible thermally heated to approximately 400 °C. Evaporation was performed about 10 min after the final annealing of the Ag(111) crystal, with no post evaporation annealing. Xe (99.99% purity) was deposited on the cold sample ($T \approx 10$ K) by opening shutters for 14 s to $P_{Xe} = 5 \times 10^{-7}$ mbar. The tip was functionalized in two steps. First, a metal terminated tip was obtained by a controlled contact of the sensor into the clean Ag(111) surface with a +2 V bias pulse. Second, the Xe-tip was obtained by spontaneous pick-up of a Xe atom from a Xe island while scanning in STM mode (0.1 V, 10 pA).

Individual TOAT molecules on Cu(111) with a neutral CO-tip and a positively charged Xe-tip were imaged using a Scienta-Omicron LT STM/AFM with a commercially available qPlus sensor, operating at 4.6 K in ultrahigh vacuum with an average pressure of 5×10^{-10} mbar. The baked qPlus sensor (3 h at 120 °C) had a quality factor of $Q \approx 30\,000$, a resonance frequency of $f_0 = 25\,634$ Hz and a peak-to-peak oscillation amplitude of approximately 2 Å.

A Cu(111) crystal surface was cleaned with several sputter and anneal cycles before inserting it in the microscope head. The TOAT molecules were thermally evaporated onto the cold surface using an e-beam evaporator (Focus GmbH). For STM imaging, the bias voltage was applied to the sample. After approaching the tip to the surface, an atomically sharp metal tip was prepared by controlled crashes into the copper surface combined with bias pulses. Each chemically passivated tip was prepared by subsequent pick-up of either a Xe atom or CO molecule.[2,50–52] After a free-lying TOAT molecule was located on the surface, the tip was left in tunneling contact ($I = 10$ pA at $V = 0.1$ V) and allowed to relax for 12 h to minimize drift and piezo-creep.

The acquisition of the three-dimensional (3D) force maps was done automatically for both sets of experiments, by measuring a sequence of constant-height images and changing the tip-sample separation in between subsequent images. The step in z was chosen to be in the order of picometres and positive, that is, increasing the tip-sample distance. All AFM images were acquired in constant-height mode. After each AFM image, the STM feedback loop was enabled for 2 s to further minimize tip-sample drift.

A complete stack of images resulting in a 3D force grid took about 13 h to acquire.

Images acquired with different tips were aligned vertically using the following procedure: First for each tip a data cube with simulated 3D frequency shift values is generated for a particular set of k and Q values. The offset in z-distance of the experimental and theoretical data sets is then determined by aligning the z-position of the frequency shift minimum for the centers of the molecules. Once this information is available for each tip, images corresponding to approximately the same tip-sample distance can be selected.

4.3.2 DFT calculations

For the DFT calculations of the PTCDA/Ag(111) system we used a pre-optimized herringbone structure of PTCDA molecules on Ag(111) surface consisting of two molecules in the unit cell and a slab of 3 Ag layers (99 Ag atoms).[53] The Hartree potential used for generating the theoretical electrostatic force field was obtained from self-consistent total energy DFT using the Vienna *ab initio* simulation package with generalized gradient approximation based functional PW91 and projector augmented-wave method.[54–56] Plane wave basis set was chosen with E_{cut} = 396 eV.

For the TOAT/Cu(111) system the total energy DFT calculations were performed using the FHI-aims code.[57] We used a 6×6 supercell made of four Cu layers to describe the Cu(111) surface. The TOAT molecule was placed on the surface with the N atom in a top-position. This position was chosen based on the experimental findings.[58] All the atoms except the two bottom Cu layers were relaxed until the remaining atomic forces and the total energy were below 10^{-2} eV/Å and 10^{-5} eV, respectively. A Monkhorst-Pack grid of 2×2×1 was used for the integration in the Brillouin zone. All the calculations were carried out at the GGA-PBE level including the Tkatchenko-Scheffler treatment of the van der Waals interaction.[59,60] The use of van der Waals interactions was necessary to correctly describe the interaction between the molecule and surface. The basis set, pseudopotentials, integration grids and Hartree potential accuracy were specified using the 'tight' settings. For species like H, O and N the basis set level was set to 'tier 2' while for Cu a first tier was used. Note that a 'tier' represents a single

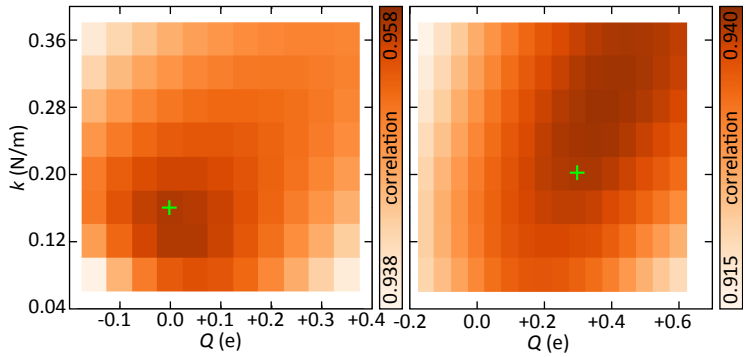

Figure 4.4 Estimation of effective k and Q for PTCDA. Two sets of frequency shift data are processed, registered and compared to the theoretically calculated maps. The input parameters (the probe particle charge Q and bending stiffness k) of the best-matching theoretical data sets represent an estimation of the probe particle characteristics in the experiment. **(a)** 2D map of linear correlation between theoretical and experimental image depending on stiffness and effective charge in mode. The green + indicates the correlation chosen for further calculations for tip A, where k = 0.16 N/m and Q=0.0 e. **(b)** 2D correlation map for tip B. The green + indicates the correlation chosen for further calculations, where k = 0.20 N/m and Q = +0.3 e.

set of radial functions added to the minimal basis to effectively describe the chemical bond.

4.3.3 Processing of experimental data and matching to simulation

To calculate high-resolution AFM images a home built AFM simulation toolkit was used.[34,35] We used default parameters of pairwise L-J potentials. The optimized structures and corresponding surface Hartree potentials were obtained from fully relaxed total energy DFT simulations of the system. The effective tip charge Q and lateral stiffness k of the probe particle are a free input of the model. The positions of the $\Delta f(z)$ minima in the centers of the molecules were taken as the reference points in z, for both the experiment and theory.

To estimate the effective stiffness k and effective charge Q the experimental and theoretical data sets are correlated.

The mechanical probe particle model can generate frequency shift maps in three

dimensions. The model uses as an input the model of the optimized structure and corresponding Hartree potential obtained from the total energy DFT calculations and two additional parameters - the effective charge of the probe particle (Q) and the stiffness of the particle on the tip (k). As the two parameters affect the contrast and proportions of the molecules, they can be fitted to match the experimental data. The fitting can be divided into three basic steps: 1) A theoretical three-dimensional frequency shift map is generated for one set of parameters. 2) The offsets in z-distance of the experimental and theoretical data sets are determined according to the z-position of the frequency shift minimum for the centers of the molecules. 3) The calculated images are periodically replicated according to the lattice vectors and registered onto the experimental data set.

As a measure of the "goodness" of the match between any two registered sets, a linear Pearson correlation of their overlapping regions was used. The procedure works very well on periodic structures, since they naturally contain a lattice, which provides anchoring points for matching with another data of the equal structure. This avoids the need for a precise distance and angle calibration, because the lattice serves as a reference itself. However, on AFM images of single molecules, some parameters have to be restricted, *e.g.* fix the zoom at one level and disable any distortion, to maintain the physical distances in the data as it had been measured.

This procedure is then repeated on other theoretical frequency shift maps generated for a range of the input parameters. The correlation with the experimental data is computed for each set of input parameters. The values of k and Q are taken to be those that provide the strongest correlation with the experimental results.

Figures 4.4 and 4.5 show the correlation between experimental data and simulated data sets with various k and Q values for the PTCDA and TOAT sample respectively. The exact value of k and Q is still uncertain within a rather broad and shallow valley of the best fit.

From the above, it should be clear that the electrostatic potential can be obtained by integration of the vector field generated from the images acquired with different tips. However, due to small errors in the distortion vectors direct integration of the

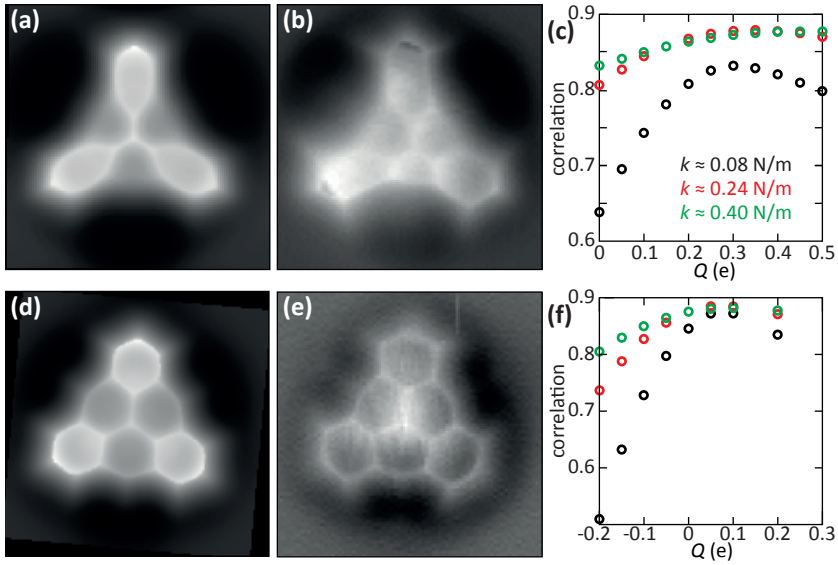

Figure 4.5 Estimation of effective *k* and *Q* for TOAT **(a)** Simulated AFM image of TOAT with Xe-tip and effective charge *Q* = +0.35 e, and spring constant *k* = 0.24 N/m. **(b)** Experimental *Δf* image of TOAT with Xe-tip. **(c)** Linear correlation coefficient between experimental image (b) and simulated images with Xe-tip for different effective charge *Q* and stiffness *k*. **(d)** Simulated AFM image of TOAT with CO-tip and effective charge *Q* = 0.0 e, and spring constant *k* = 0.24 N/m. **(e)** Experimental *Δf* image of TOAT with CO-tip. **(f)** Linear correlation coefficient between experimental image (d) and simulated images with CO-tip different effective charge *Q* and stiffness *k*.

distortion vector field will not provide satisfactory results. Instead, the vector field is fitted by a potential. A least-square minimization method was used by iterative blind random variation (mutation) of the potential. The resolution of the reconstructed potential is given by the resolution of the deformation vector field, in our case 3 times smaller than the resolution of the original images.

The algorithm takes the original vector field as the input and iteratively determines the potential using the following steps:

1) A potential is set to an array of random values and a vector field is calculated from it by finite differences.

2) The sum of squares is evaluated for the difference between calculated and the input vector fields. This sum of squares is stored as a reference value.

3) The electrostatic potential φ is modified by addition a randomly generated value $\delta\varphi$ and the vector field is calculated again using the modified potential.

4) If the sum of squared differences improves, then a new potential and sum of squares is stored, otherwise step 3 is repeated.

This algorithm is repeated until the potential is recovered. In our case, the boundary conditions are set to zero. Consequently, the algorithm tends to over-relax the potential near the edges of the simulation cell. To alleviate this problem, the procedure is interrupted once the features in the potential landscape are smooth and appear continuous.

4.4 Results

The experimental results and the extracted electrostatic potentials are discussed below for the two systems under investigation.

4.4.1 Molecular layers of PTCDA on Ag(111)

In the case of densely packed self-assembled molecular layers, the van der Waals force component varies slowly. In addition, the effective stiffness k for different tips typically has similar values. Therefore, the term δx_{vdW} in equation (7) can be neglected and the surface electrostatic field is given by $E_S = k_A\, \delta x / Q_A$.

Figure 4.6(a-b) shows two constant-height AFM images of a self-assembled monolayer of PTCDA on Ag(111) acquired with a neutral and positively charged Xe tip at the same tip-sample distance. Note that the apparent size of the anhydride groups, indicated by the red circles, is different in the two images. We attribute these differences to a repulsive electrostatic interaction between the positively charged Xe tip and the positively charged anhydride groups.[61] This assignment is supported by a very good agreement between experimental and simulated AFM images of PTCDA/Ag(111) with different effective charges on the Xe tip, as can be seen in figure 4.6(c-d). The determined values for k_A, k_B, Q_A and Q_B are: 0.16 N/m, 0.20 N/m, 0.0 e and +0.3 e, respectively, as previously presented in figure 4.4.

The abundant presence of sharp features in the AFM images allows us to use an

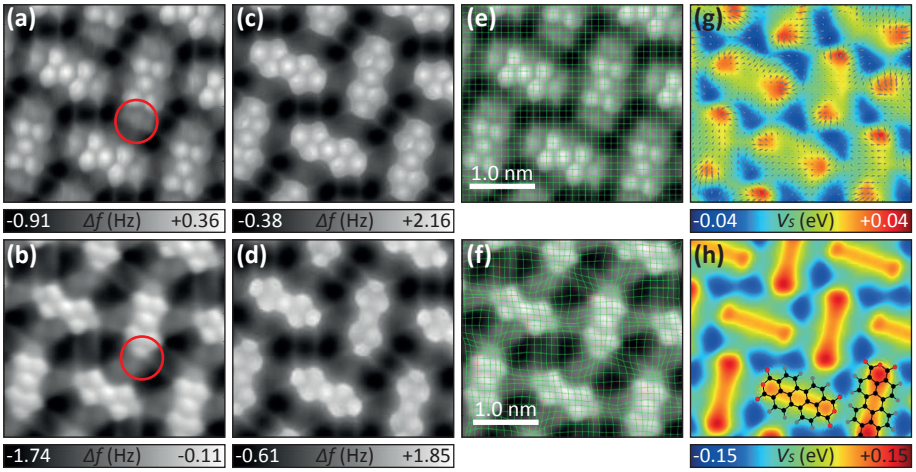

Figure 4.6 Determining the electrostatic field above a close-packed PTCDA layer. **(a,b)** Experimental high-resolution AFM images of a self-assembled monolayer of PTCDA deposited on Ag(111) obtained with two different Xe tips. **(c)** Simulated AFM image using an effective charge Q = 0.0 e and the effective lateral stiffness k = 0.16 N/m. **(d)** Same as (c) but with Q = +0.3 e and k = 0.20 N/m. **(e,f)** The experimental images superimposed with a deformation grid defined by comparing the corresponding sharp features between the two images in (a) and (b). **(g)** Electrostatic potential calculated from the deformation field (grey arrows). **(h)** Calculated Hartree potential from DFT simulations 3.0 Å above the molecular layer.

automatic computer algorithm to determine the differences in the image distortions, that is, δx. First, two AFM images are brought into register. Subsequently, the distortion field is found by comparing the corresponding sharp features between the two images. The algorithm is based on matching small regions of the two images. The image is divided into small tiles, in our case regularly distributed circular areas with a diameter of the characteristic image feature (for example, C–C bonds, carbon hexagons *etc.*). These circular areas are each matched to the other image by moving them laterally, searching for maximum correlation. The resulting translation vectors represent a good approximation of the distortion between the two images, and serve as input for the electrostatic potential determination. The green grids plotted in figure 4.6(e-f) visualize the determined deformation.

As argued above, the as-obtained deformation field, grey arrows in figure 4.6(g),

is linearly proportional to the lateral electrostatic field above the molecular layer, with proportionality constant k_A/Q_A. The electrostatic potential obtained from the experimental images is shown in figure 4.6(g) and is in very good agreement with the electrostatic potential as calculated from density functional theory (DFT), displayed in figure 4.6(h). The absolute magnitude +0.04 to -0.04 eV of the electrostatic field as determined experimentally is approximately three times smaller than estimated from DFT calculations. This discrepancy can be attributed to several effects, such as uncertainties in the absolute tip-sample distance where the electrostatic potential is measured; in the values of the effective charge Q and lateral stiffness k; in or the finite oscillation amplitude. The limits of the method and their possible solutions are addressed in section 4.5 of this chapter.

From the correlation analysis of the experimental and theoretical AFM images of PTCDA shown in figure 4.4, we can estimate the uncertainties in Q and k. For the neutral tip, the maximum correlation is well defined within ±0.05 e and ±0.08 N/m. However, for the positively charged tip there are multiple Q-k combinations that provide a similar correlation between experiment and theory. As the scaling term of the vector field is the ratio Q/k, we can estimate the systematic error from its variation. By selecting the different favorable Q-k pairs, we find a systematic error of approximately 20%. It is important to note that this uncertainty only affects the absolute values, that is, the relative variation of the electrostatic potential is correct.

4.4.2 Single TOAT molecule on Cu(111)

As a second example, we studied individual TOAT molecules, since they have a highly non-homogeneous charge distribution. The central N atom donates an electron to the delocalized p-system and is thus positively charged. In contrast, the three ketone groups at the edge of the molecule withdraw electron density from the ring system and therefore have a partial negative charge. High-pass filtered constant-height AFM images of a TOAT molecule on Cu(111) acquired with a Xe-tip and a CO-tip are shown in figure 4.7(a) and (b) respectively. There are significant differences between images acquired with the two different tip terminations. The central region of the molecule

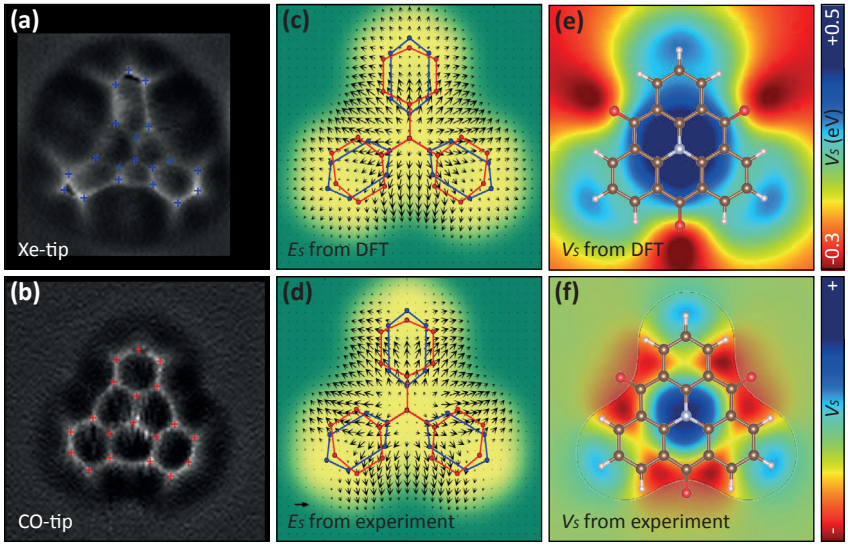

Figure 4.7 Determining the electrostatic field above an individual molecule. **(a)** High-pass filtered constant-height AFM images of a TOAT molecule on Cu(111) acquired with a Xe-tip. Crosses indicate characteristic vertices. **(b)** Same as (a) but measured with a CO-tip. **(c)** Electrostatic force field calculated from DFT. **(d)** Experimentally determined electrostatic force field obtained after subtraction of the van der Waals component from the deformation field obtained from the images shown in (a-b). **(e)** Calculated Hartree potential. **(f)** Eelectrostatic potential calculated from the experimental deformation field shown in (d).

appears smaller while the peripheral benzene rings are elongated for images acquired with a Xe- tip compared to images obtained with a CO-tip. Again, this effect is attributed to a repulsive interaction between the positively charged Xe-tip and the positively charged central area of the molecule. This effect is reproduced by our simulations for a Xe-tip with an effective charge $Q = +0.3$ e and lateral stiffness $k = 0.24$ N/m, see figure 4.5(a-c). Similarly, we found the best match between experimental and theoretical AFM images acquired with the CO-tip with an effective charge $Q = 0.0$ e and lateral stiffness $k = 0.24$ N/m, see figure 4.5(d-f). For individual molecules, positions of vertices were determined manually, displayed as blue and red markers in figure 4.7(a-b). The deformation field can be obtained by alignment of corresponding vertices (δx) in the two AFM images using interpolation by radial basis functions and exploiting the

threefold rotational symmetry of the TOAT molecule. The obtained deformation field is directly proportional to total lateral force field.

Here, the estimated lateral force field also contains the van der Waals force component, which can be determined with the help of numerical modelling.[34] Thus the electrostatic field E_S can be reconstructed from equation (7) using the fitted lateral stiffness ($k_A = k_B$) and differential van der Waals deformation field δx_{vdW}. Figure 4.7(d) shows the as-determined electrostatic field while its calculated counterpart is given in figure 4.7(c). The agreement between theory and experiment above the molecule is again very good. Note that the method cannot provide resolution outside of the molecule, the green area in figure 4.7(c-d), due to the lack of sharp features in this region. Hence we nullified the obtained electrostatic field in this area.

For the TOAT molecules, we obtained the experimental electrostatic potential VS by determining the derivative of the electrostatic field E_S. The resulting electrostatic potential, shown in figure 4.7(f), matches the calculated electrostatic field over the molecule including a complex charge distribution on the benzene rings. The charge distribution near the oxygen atoms cannot be described properly due to the lack of sharp features in this area. In the TOAT case, our method cannot reliably quantify the absolute magnitude of the electrostatic potential due to uncertainties associated with subtraction of the van der Waals force field and the absence of sharp features outside the molecule. We therefore decided not to provide a quantitative comparison of the electrostatic potential V_S to avoid an over-interpretation of our method.

4.5 Discussion

In the following, important advantages and limitations of the method are discussed.

The resolution of our method is directly connected to the requirement of having sharp edges in images originating from a saddle point of the potential energy surface. Therefore, the method can only be used to determine the electrostatic field at close tip-sample distances where such features are present. As discussed above, the position of the sharp edges remains practically constant in the close distance regime. This has two important consequences. First, the position of sharp edges is determined by a bifurcation in the probe-particle trajectories upon tip approach. The deflection

of the probe particle beyond this branching point does not further affect the apparent position of the edges in the images. Consequently, only the value of the lateral spring constant k at the tip-sample distance where the branching occurs will influence the results. Therefore, variations of the lateral stiffness k with tip-sample distance do not affect the analysis. Second, our method can only map the electrostatic field at the height where the trajectory of the probe particle branches.

It is important to note that sharp edges are visible in both simultaneously acquired AFM and STM channels. In addition, sharp features are also present in high-resolution STM and IETS-STM images.[3,4] Hence, in principle, our method can also be applied to such data.

The possibility to extract quantitative information depends critically on several factors. First, uncertainties in the values of k and Q could potentially be eliminated by acquiring two images with the same functionalized tip, the charge of which can be effectively modified by other means, for example, by some oxidation/reduction process of the moiety attached to the tip. A search for new functionalized tips with the possibility to modulate an effective charge without losing its mechanical stability is the subject of current investigations. Alternatively, one can try to reduce the uncertainties in k and Q by, for example, using more sophisticated algorithms for image analysis. The simulation of the electrostatic interaction can be further improved by implementation of a more realistic charge distribution on the probe particle using dipole/quadrupole or even the charge distribution obtained directly from ab initio calculations.[62]

4.6 Conclusion

In conclusion, we showed that the electrostatic interaction between the probe and a molecule on the surface results in apparent distortions of the structure of molecules in high-resolution images. This effect can be exploited to map the electrostatic field originating from polar molecules with high resolution by analyzing the differences in the distortions in images acquired with differently charged tips. The arguments and results presented above demonstrate the background, advantages and limitations of the method to probe the electrostatic potential of molecules with sub-molecular spatial resolution. The main advantages of this method are the clear relation between

the physical observables and the electrostatic field, the high spatial resolution and its applicability to both STM and AFM images. In addition, it offers the prospect of extracting quantitative information. Here, we applied the method for molecules, but it can be easily extended to surfaces and surface defects. As such, it constitutes a valuable complementary tool to existing techniques.

Finally we would like to stress that the general idea behind the technique can be applied to any lateral force acting on the last atom of the tip. Consequently, new potential applications can be envisaged, such as imaging the electrostatic field of the probe itself or that of excited molecules. In addition, it may be possible to map molecular magnetic fields as well.

4.7 References

[1] J. Repp, G. Meyer, S. M. Stojković, A. Gourdon, C. Joachim, Molecules on Insulating Films: Scanning-Tunneling Microscopy Imaging of Individual Molecular Orbitals. *Phys. Rev. Lett.* **94**, 26803 (2005).

[2] L. Gross, F. Mohn, N. Moll, P. Liljeroth, G. Meyer, The Chemical Structure of a Molecule Resolved by Atomic Force Microscopy. *Science.* **325**, 1110–1114 (2009).

[3] R. Temirov, S. Soubatch, O. Neucheva, A. C. Lassise, F. S. Tautz, A novel method achieving ultra-high geometrical resolution in scanning tunnelling microscopy. *New J. Phys.* **10**, 53012 (2008).

[4] C. -l. Chiang, C. Xu, Z. Han, W. Ho, Real-space imaging of molecular structure and chemical bonding by single-molecule inelastic tunneling probe. *Science.* **344**, 885–888 (2014).

[5] L. Gross, F. Mohn, N. Moll, B. Schuler, A. Criado, E. Guitian, D. Pena, A. Gourdon, G. Meyer, Bond-Order Discrimination by Atomic Force Microscopy. *Science.* **337**, 1326–1329 (2012).

[6] L. Gross, Recent advances in submolecular resolution with scanning probe microscopy. *Nat. Chem.* **3**, 273–278 (2011).

[7] M. Emmrich, F. Huber, F. Pielmeier, J. Welker, T. Hofmann, M. Schneiderbauer, D. Meuer, S. Polesya, S. Mankovsky, D. Kodderitzsch, H. Ebert, F. J. Giessibl, Subatomic resolution force microscopy reveals internal structure and adsorption sites of small iron clusters. *Science.* **348**, 308–311 (2015).

[8] A. Sweetman, S. P. Jarvis, P. Rahe, N. R. Champness, L. Kantorovich, P. Moriarty, Intramolecular bonds resolved on a semiconductor surface. *Phys. Rev. B.* **90**, 165425 (2014).

[9] K. Iwata, S. Yamazaki, P. Mutombo, P. Hapala, M. Ondráček, P. Jelínek, Y. Sugimoto, Chemical structure imaging of a single molecule by atomic force microscopy at room temperature. *Nat. Commun.* **6**, 7766 (2015).

[10] C. Moreno, O. Stetsovych, T. K. Shimizu, O. Custance, Imaging Three-Dimensional Surface Objects with Submolecular Resolution by Atomic Force Microscopy. *Nano Lett.* **15**, 2257–2262 (2015).

[11] F. Huber, S. Matencio, A. J. Weymouth, C. Ocal, E. Barrena, F. J. Giessibl, Intramolecular Force

Contrast and Dynamic Current-Distance Measurements at Room Temperature. *Phys. Rev. Lett.* **115**, 66101 (2015).
[12] D. G. de Oteyza, P. Gorman, Y.-C. Chen, S. Wickenburg, A. Riss, D. J. Mowbray, G. Etkin, Z. Pedramrazi, H.-Z. Tsai, A. Rubio, M. F. Crommie, F. R. Fischer, Direct Imaging of Covalent Bond Structure in Single-Molecule Chemical Reactions. *Science.* **340**, 1434–1437 (2013).
[13] N. Pavliček, B. Fleury, M. Neu, J. Niedenfu, C. Herranz-lancho, M. Ruben, J. Repp, Atomic Force Microscopy Reveals Bistable Configurations of Dibenzo[a,h] thianthrene and their Interconversion Pathway. *Phys. Rev. Lett.* **108**, 86101 (2012).
[14] S. Kawai, A. Sadeghi, X. Feng, P. Lifen, R. Pawlak, T. Glatzel, A. Willand, A. Orita, J. Otera, S. Goedecker, E. Meyer, Obtaining Detailed Structural Information about Supramolecular Systems on Surfaces by Combining High-Resolution Force Microscopy with ab Initio Calculations. *ACS Nano.* **7**, 9098–9105 (2013).
[15] B. Schuler, G. Meyer, D. Peña, O. C. Mullins, L. Gross, Unraveling the Molecular Structures of Asphaltenes by Atomic Force Microscopy. *J. Am. Chem. Soc.* **137**, 9870–9876 (2015).
[16] N. Pavliček, B. Schuler, S. Collazos, N. Moll, D. Pérez, E. Guitián, G. Meyer, D. Peña, L. Gross, On-surface generation and imaging of arynes by atomic force microscopy. *Nat. Chem.* **7**, 623–628 (2015).
[17] T. Dienel, S. Kawai, H. Söde, X. Feng, K. Müllen, P. Ruffieux, R. Fasel, O. Gröning, Resolving Atomic Connectivity in Graphene Nanostructure Junctions. *Nano Lett.* **15**, 5185–5190 (2015).
[18] J. Clayden, N. Greeves, S. Warren, Organic Chemistry *Oxford University Press* (2001).
[19] M. Nonnenmacher, M. P. O'Boyle, H. K. Wickramasinghe, Kelvin probe force microscopy. *Appl. Phys. Lett.* **58**, 2921 (1991).
[20] F. Mohn, L. Gross, N. Moll, G. Meyer, Imaging the charge distribution within a single molecule. *Nat. Nanotechnol.* **7**, 227–231 (2012).
[21] R. Baier, C. Leendertz, M. C. Lux-Steiner, S. Sadewasser, Toward quantitative Kelvin probe force microscopy of nanoscale potential distributions. *Phys. Rev. B.* **85**, 165436 (2012).
[22] G. H. Enevoldsen, T. Glatzel, M. C. Christensen, J. V. Lauritsen, F. Besenbacher, Atomic Scale Kelvin Probe Force Microscopy Studies of the Surface Potential Variations on the TiO2(110) Surface. *Phys. Rev. Lett.* **100**, 236104 (2008).
[23] S. Sadewasser, P. Jelinek, C.-K. Fang, O. Custance, Y. Yamada, Y. Sugimoto, M. Abe, S. Morita, New Insights on Atomic-Resolution Frequency-Modulation Kelvin-Probe Force-Microscopy Imaging of Semiconductors. *Phys. Rev. Lett.* **103**, 266103 (2009).
[24] B. Schuler, S. Liu, Y. Geng, S. Decurtins, Contrast formation in Kelvin probe force microscopy of single π-conjugated molecules. *Nano Lett.* **14**, 3342–6 (2014).
[25] J. L. Neff, P. Rahe, Insights into Kelvin probe force microscopy data of insulator-supported molecules. *Phys. Rev. B.* **91**, 85424 (2015).
[26] M. Corso, M. Ondráček, C. Lotze, P. Hapala, K. J. Franke, P. Jelínek, J. I. Pascual, Charge Redistribution and Transport in Molecular Contacts. *Phys. Rev. Lett.* **115**, 136101 (2015).
[27] A. J. Weymouth, T. Wutscher, J. Welker, T. Hofmann, F. J. Giessibl, Phantom Force Induced by Tunneling Current: A Characterization on Si(111). *Phys. Rev. Lett.* **106**, 226801 (2011).
[28] F. Albrecht, J. Repp, M. Fleischmann, M. Scheer, M. Ondráček, P. Jelínek, Probing Charges on the Atomic Scale by Means of Atomic Force Microscopy. *Phys. Rev. Lett.* **115**, 76101 (2015).
[29] C. Wagner, M. F. B. Green, P. Leinen, T. Deilmann, P. Krüger, M. Rohlfing, R. Temirov, F. S. Tautz, Scanning Quantum Dot Microscopy. *Phys. Rev. Lett.* **115**, 26101 (2015).
[30] L. Bartels, G. Meyer, K.-H. Rieder, D. Velic, E. Knoesel, A. Hotzel, M. Wolf, G. Ertl, Dynamics of

Electron-Induced Manipulation of Individual CO Molecules on Cu(111). *Phys. Rev. Lett.* **80**, 2004–2007 (1998).

[31] J. Welker, F. J. Giessibl, Revealing the Angular Symmetry of Chemical Bonds by Atomic Force Microscopy. *Science.* **336**, 444–449 (2012).

[32] F. Mohn, B. Schuler, L. Gross, G. Meyer, Different tips for high-resolution atomic force microscopy and scanning tunneling microscopy of single molecules. *Appl. Phys. Lett.* **102**, 73109 (2013).

[33] N. Moll, L. Gross, F. Mohn, A. Curioni, G. Meyer, The mechanisms underlying the enhanced resolution of atomic force microscopy with functionalized tips. *New J. Phys.* **12**, 125020 (2010).

[34] P. Hapala, G. Kichin, C. Wagner, F. S. Tautz, R. Temirov, P. Jelínek, Mechanism of high-resolution STM/AFM imaging with functionalized tips. *Phys. Rev. B.* **90**, 85421 (2014).

[35] P. Hapala, R. Temirov, F. S. Tautz, P. Jelínek, Origin of High-Resolution IETS-STM Images of Organic Molecules with Functionalized Tips. *Phys. Rev. Lett.* **113**, 226101 (2014).

[36] C.-S. Guo, X. Xin, M. A. Van Hove, X. Ren, Y. Zhao, Origin of the Contrast Interpreted as Intermolecular and Intramolecular Bonds in Atomic Force Microscopy Images. *J. Phys. Chem. C.* **119**, 150611095359009 (2015).

[37] J. van der Lit, F. Di Cicco, P. Hapala, P. Jelinek, I. Swart, Submolecular Resolution Imaging of Molecules by Atomic Force Microscopy: The Influence of the Electrostatic Force. *Phys. Rev. Lett.* **116**, 96102 (2016).

[38] M. P. Boneschanscher, S. K. Hämäläinen, P. Liljeroth, I. Swart, Sample Corrugation Affects the Apparent Bond Lengths in Atomic Force Microscopy. *ACS Nano.* **8**, 3006–3014 (2014).

[39] M. Neu, N. Moll, L. Gross, G. Meyer, F. J. Giessibl, J. Repp, Image correction for atomic force microscopy images with functionalized tips. *Phys. Rev. B.* **89**, 205407 (2014).

[40] J. Zhang, P. Chen, B. Yuan, W. Ji, Z. Cheng, X. Qiu, Real-Space Identification of Intermolecular Bonding with Atomic Force Microscopy. *Science.* **342**, 611–614 (2013).

[41] A. M. Sweetman, S. P. Jarvis, H. Sang, I. Lekkas, P. Rahe, Y. Wang, J. Wang, N. R. Champness, L. Kantorovich, P. Moriarty, Mapping the force field of a hydrogen-bonded assembly. *Nat. Commun.* **5**, 1–7 (2014).

[42] N. Moll, B. Schuler, S. Kawai, F. Xu, L. Peng, A. Orita, J. Otera, A. Curioni, M. Neu, J. Repp, G. Meyer, L. Gross, Image Distortions of a Partially Fluorinated Hydrocarbon Molecule in Atomic Force Microscopy with Carbon Monoxide Terminated Tips. *Nano Lett.* **14**, 6127–6131 (2014).

[43] S. K. Hämäläinen, N. van der Heijden, J. van der Lit, S. den Hartog, P. Liljeroth, I. Swart, Intermolecular Contrast in Atomic Force Microscopy Images without Intermolecular Bonds. *Phys. Rev. Lett*. **113**, 186102 (2014).

[44] S. Kawai, A. Sadeghi, F. Xu, L. Peng, A. Orita, J. Otera, S. Goedecker, E. Meyer, Extended Halogen Bonding between Fully Fluorinated Aromatic Molecules. *ACS Nano.* **9**, 2574–2583 (2015).

[45] S. P. Jarvis, M. A. Rashid, A. Sweetman, J. Leaf, S. Taylor, P. Moriarty, J. Dunn, Intermolecular artifacts in probe microscope images of C60 assemblies. *Phys. Rev. B.* **92**, 241405 (2015).

[46] P. Hapala, M. Švec, O. Stetsovych, N. J. van der Heijden, M. Ondráček, J. van der Lit, P. Mutombo, I. Swart, P. Jelínek, Mapping the electrostatic force field of single molecules from high-resolution scanning probe images. *Nat. Commun.* **7**, 11560 (2016).

[47] D. Z. Gao, J. Grenz, M. B. Watkins, F. Federici Canova, A. Schwarz, R. Wiesendanger, A. L. Shluger, Using Metallic Noncontact Atomic Force Microscope Tips for Imaging Insulators

and Polar Molecules: Tip Characterization and Imaging Mechanisms. *ACS Nano.* **8**, 5339–5351 (2014).

[48] Z. Sun, M. P. Boneschanscher, I. Swart, D. Vanmaekelbergh, P. Liljeroth, Quantitative Atomic Force Microscopy with Carbon Monoxide Terminated Tips. *Phys. Rev. Lett.* **106**, 46104 (2011).

[49] A. J. Weymouth, T. Hofmann, F. J. Giessibl, Quantifying Molecular Stiffness and Interaction with Lateral Force Microscopy. *Science.* **343**, 1120–1122 (2014).

[50] D. M. Eigler, C. P. Lutz, W. E. Rudge, An atomic switch realized with the scanning tunnelling microscope. *Nature.* **352**, 600–603 (1991).

[51] L. Bartels, G. Meyer, K.-H. Rieder, Controlled vertical manipulation of single CO molecules with the scanning tunneling microscope: A route to chemical contrast. *Appl. Phys. Lett.* **71**, 213 (1997).

[52] F. J. Giessibl, Advances in atomic force microscopy. *Rev. Mod. Phys.* **75**, 949–983 (2003).

[53] M. Rohlfing, R. Temirov, F. S. Tautz, Adsorption structure and scanning tunneling data of a prototype organic-inorganic interface: PTCDA on Ag(111). *Phys. Rev. B.* **76**, 115421 (2007).

[54] G. Kresse, J. Furthmüller, Efficient iterative schemes for ab initio total-energy calculations using a plane-wave basis set. *Phys. Rev. B.* **54**, 11169–11186 (1996).

[55] J. P. Perdew, J. A. Chevary, S. H. Vosko, K. A. Jackson, M. R. Pederson, D. J. Singh, C. Fiolhais, Atoms, molecules, solids, and surfaces: Applications of the generalized gradient approximation for exchange and correlation. *Phys. Rev. B.* **46**, 6671–6687 (1992).

[56] G. Kresse, D. Joubert, From ultrasoft pseudopotentials to the projector augmented-wave method. *Phys. Rev. B.* **59**, 1758–1775 (1999).

[57] V. Blum, R. Gehrke, F. Hanke, P. Havu, V. Havu, X. Ren, K. Reuter, M. Scheffler, Ab initio molecular simulations with numeric atom-centered orbitals. *Comput. Phys. Commun.* **180**, 2175–2196 (2009).

[58] N. J. van der Heijden, P. Hapala, J. A. Rombouts, J. van der Lit, D. Smith, P. Mutombo, M. Švec, P. Jelinek, I. Swart, Characteristic Contrast in Δ f min Maps of Organic Molecules Using Atomic Force Microscopy. *ACS Nano.* **10**, 8517–8525 (2016).

[59] J. P. Perdew, K. Burke, M. Ernzerhof, Generalized Gradient Approximation Made Simple. *Phys. Rev. Lett.* **77**, 3865–3868 (1996).

[60] A. Tkatchenko, M. Scheffler, Accurate Molecular Van Der Waals Interactions from Ground-State Electron Density and Free-Atom Reference Data. *Phys. Rev. Lett.* **102**, 73005 (2009).

[61] L. Gross, B. Schuler, F. Mohn, N. Moll, N. Pavliček, W. Steurer, I. Scivetti, K. Kotsis, M. Persson, G. Meyer, Investigating atomic contrast in atomic force microscopy and Kelvin probe force microscopy on ionic systems using functionalized tips. *Phys. Rev. B.* **90**, 155455 (2014).

[62] M. Ellner, N. Pavliček, P. Pou, B. Schuler, N. Moll, G. Meyer, L. Gross, R. Peréz, The Electric Field of CO Tips and Its Relevance for Atomic Force Microscopy. *Nano Lett.* **16**, 1974–1980 (2016).

5

Recognizing nitrogen dopant atoms in graphene using AFM

abstract

Doping graphene by heteroatoms such as nitrogen presents an attractive route to control the position of the Fermi level in the material. We prepared N-doped graphene on Cu(111) and Ir(111) surfaces via chemical vapor deposition of two different molecules. Using scanning tunneling microscopy images as a benchmark, we show that the position of the dopant atoms can be determined using atomic force microscopy. Specifically, the frequency shift–distance curves $\Delta f(z)$ acquired above a nitrogen atom are significantly different from the curves measured over a carbon atom. Similar behavior was found for N-doped graphene on Cu(111) and Ir(111). The results are corroborated by density functional theory calculations employing a van der Waals functional.

based on

Nadine J. van der Heijden, Daniël Smith, Gaetano Calogero, Rik S. Koster, Daniel Vanmaekelbergh, Marijn A. van Huis, and Ingmar Swart, *Physical Review B* **93**, 245430 (2016)

5.1 Introduction

The position of the Fermi level in conventional semiconductors can be controlled by introducing dopant atoms into the lattice. The same approach can be used for graphene.[1–5] In order to understand the effect of dopant atoms in graphene, it is essential to be able to study the number of dopants, their distribution, and how they are incorporated in the lattice, ideally down to the atomic level.

Scanning tunneling microscopy (STM) has been used to study the geometric and electronic structure of mechanically exfoliated and epitaxially grown graphene[6–15] and graphene nanostructures.[16–21] Doped graphene has also been studied with STM. For example, it was found that nitrogen- and boron-dopant atoms in graphene have a characteristic appearance in STM images, allowing their identification.[22–24] Furthermore, it was found that the nitrogen atoms in graphene, grown by chemical vapor deposition, occupy predominantly one sublattice of graphene.[25] Due to the convolution of geometric and electronic contributions to the STM signal, it is typically not straightforward to determine how the dopant atoms are incorporated into the lattice. However, precisely the incorporation in the lattice determines how the dopant atoms affect the properties of the host material.[26]

Atomic force microscopy (AFM) can image the geometric structure of graphite and graphene with atomic resolution.[3,27–34] Chemical recognition of atoms in a material with AFM is however nontrivial. It has been shown that AFM-based force-distance spectroscopy can provide chemical contrast between the chemically very different Pb, Si, and Sn atoms in an alloy surface.[35] More recently, the chemical reactivity of boron- and nitrogen-doped graphene grown on silicon carbide was investigated with AFM.[24] Chemically passivated tips can also provide different contrast above boron atoms in graphene.[5] Since we aim to identify two chemical elements that are similar in size and are expected to have the same coordination in the lattice, we opted to use metal tips. Metal tips are not chemically inert and we expected that by using metal tips discerning small differences would be easier than with functionalized tips.

Here, we describe a method by which individual N-dopant atoms in graphene can be recognized by AFM. Using STM data as a benchmark, we show that the minima in frequency shift–distance $\Delta f(z)$ spectra are distinctly different for N and C atoms.

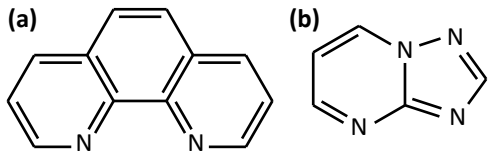

Figure 5.1 (a) 1,10-phenanthroline (Phen). **(b)** 1,2,4-Triazolo[1,5-a]pyrimidine (Pyr).

This behavior was observed for graphene grown on Cu(111) and Ir(111) surfaces. By exploiting the well-defined moiré pattern of the latter, we analyzed the influence of height corrugation of the substrate, as well as the coupling strength to the surface. The experimental results are corroborated by density functional theory (DFT) calculations.

5.2 Methods

5.2.1 Sample preparation and synthesis

Clean Cu(111) and Ir(111) crystals were prepared using several sputtering and annealing cycles with Ar^+. For the synthesis of N-doped graphene on Cu(111), a protocol from Zabet-Khosousi *et al.* was adapted,[25] while for synthesis on Ir(111) we adapted the method described by N'Diaye *et al.*[7] Two types of precursor molecules were used: 1,10-phenanthroline (Phen) and 1,2,4-triazolo(1,5-a)pyrimidine (Pyr), both purchased from Sigma-Aldrich and used without further purification (indicated purity: 99% for both). Their chemical structures are shown in figure 5.1. Note that the ratio between N and C atoms in the molecules is 1:6 for Phen and 4:5 for Pyr. Precursors were thermally evaporated onto a hot Cu(111) (875 °C) or Ir(111) (1200 °C) surface. After molecular deposition, the temperature of the metal crystals was kept constant at these temperatures for 20 minutes for Cu(111) and for 30 seconds for Ir(111). The Ir(111) crystal was transferred out of the preparation chamber at an elevated temperature to minimize the adsorption of residual molecules onto the surface.

5.2.2 Experimental procedures

The experiments were performed using a combined LT STM/AFM from Scienta

Omicron GmbH. The base pressure was lower than 2×10^{-9} mbar, and the working temperature was 4.6 K. A commercially available qPlus sensor with resonance frequency $f_0 \approx 25$ kHz, spring constant $k \approx 1800$ N/m, and quality factor $Q \approx 25$k was used, which was operated with a peak-to-peak amplitude of approximately 2 Å. All STM images were obtained in constant-current mode, with the bias applied to the sample. All AFM images were acquired in constant-height mode. 3D frequency shift data was obtained by taking multiple constant-height AFM images at stepwise increasing tip-sample distance. Semi-active drift compensation was applied by correlating STM images obtained between AFM images to determine the lateral drift and compensating for this between consecutive AFM images. Tips providing atomic resolution were prepared by controlled contact with the metal surface and voltage pulses, resulting in a sharp metal tip apex. The tip apex was not functionalized because we expect that using a chemically active tip apex would enable discerning small differences in chemical properties of the investigated atoms. From the 3D data cube, we extracted the coordinates of the minima of all $\Delta f(z)$ curves (Δf_{min} and z_{min}) by fitting a parabolic function to points up to 0.5 Hz above the most negative Δf value.

5.2.3 Density functional theory calculations

Density functional theory (DFT) simulations were performed on a crystallographic model of graphene/Ir(111). The hexagonal supercell consisted of a (9×9×4) slab of iridium atoms and a single (10×10) layer of graphene; see figure 5.2.[10] The calculations employed the projector augmented plane wave method,[36,37] the generalized gradient approximation (GGA) and the exchange-correlation functional formulated by Perdew, Burke, and Ernzerhof (PBE)[38] as implemented in the Vienna Ab initio Simulation Package (VASP).[37,39,40] Van der Waals forces were added by DFT-D3 (BJ damping),[41] and a Γ-centered (3×3×1) k-point mesh was used for sampling. Cut-off values for the wave functions and augmentation functions of 400 eV and 560 eV were used, respectively. Table I gives some key numbers concerning the corrugation of the graphene layer with respect to the Ir(111) substrate, as well as a comparison to previous work. Our results are in good agreement with previously reported values. We found an adsorption energy of 88 meV per C atom, which is close to previously

Table I Corrugation of the graphene moiré pattern on Ir(111). The value of *h* in the various positions is computed using the height of the nearest Ir atom as a reference.

Reference	Method	h_{top} (Å)	h_{fcc} (Å)	h_{hcp} (Å)	h_{bridge} (Å)	$\hbar$ (Å)	Δh (Å)
Hämäläinen *et al.*[34]	LEED	3.71	3.29	3.27	n/a	3.39±0.03	0.43±0.09
Busse *et al.*[10]	DFT	3.62	3.29	3.27	n/a	3.41	0.35
Voloshina *et al.*[33]	DFT	3.58	3.28	3.27	3.315	n/a	n/a
This work	DFT	3.63[a]	3.32[b]	3.31	3.32	3.40	0.34

[a]All the atoms that constitute the hexagon in the top position have the same height.
[b]The values for h_{fcc}, h_{hcp}, and h_{bridge} correspond to the height of the lowest atom among otherwise equivalent sites.

reported values.[10]

$\Delta f(z)$ curves were simulated based on calculations involving a tetrahedral metal Ir(111) cluster of four atoms that was brought closer to the sample in a stepwise manner. The size of the tip cluster was limited to four atoms (in two layers) to balance the computational cost and accuracy, considering the large unit cell needed to describe the substrate. The small oscillation amplitudes used in the experiment increase the sensitivity to short-range chemical forces, thus justifying the two-layer tip cluster. However, our calculations will underestimate the magnitude of the electrostatic and van der Waals contributions to the total tip-sample force.[42] During these calculations the tip-apex atom, the probed atom, and its three nearest neighbors were allowed to relax their position; the positions of all other atoms of the graphene and iridium slab were fixed. We fitted the as-obtained data points with a Morse potential. The fitted energy-distance curves were first converted to force-distance curves by taking the derivative with respect to distance, and subsequently to $\Delta f(z)$ curves using the method described by Giessibl.[43]

5.3 Results and discussion

5.3.1 Growing N-doped graphene

We first describe the results for N-doped graphene on Cu(111). Figure 5.3(a-b) shows an overview and higher magnification image of a graphene film grown using Phen.

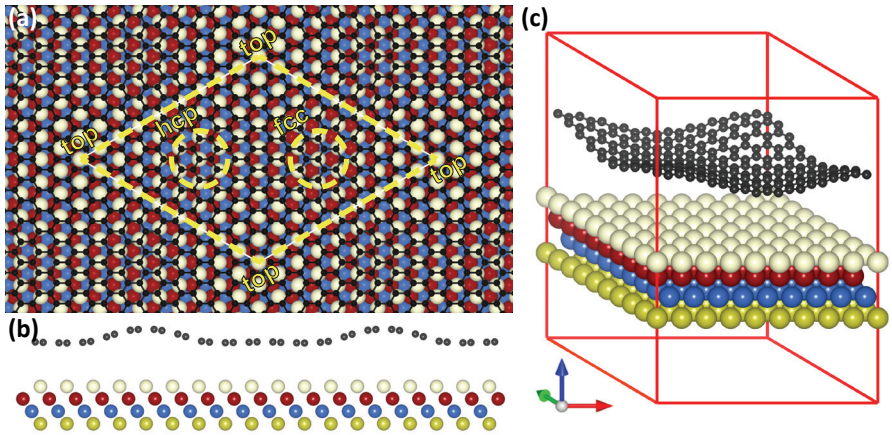

Figure 5.2 Crystallographic model of graphene/Ir(111). Carbon atoms are indicated in black. Iridium atoms are colored by layer. Top, second, third and bottom layers are colored white, red, blue, and yellow, respectively. **(a)** Top view, with the super cell and its characteristic positions outlined in yellow. **(b)** Side view, height difference in graphene corrugation are amplified by a factor 10. **(c)** Oblique projection.

The overview image shows that synthesis of N-doped graphene on Cu(111) resulted in flaked, irregular, small patches of graphene with a diameter up to 100 nm. A more zoomed view of such a graphene patch, figure 5.3(b), shows characteristic triangular shaped features that have been assigned to individual N dopants in graphene.[23,25,44] Determining the optimal parameters to grow large graphene flakes on Cu(111) using the method described above is beyond the scope of the present paper.

Phen can also be used to grow N-doped graphene on Ir(111). In this case, films with lateral sizes on the order of micrometers were obtained. Figure 5.3(c) shows an STM image of such a large graphene sheet. The elongated features with larger apparent height, *i.e.*, the white stripes, are due to rippling of the graphene sheet.[6,45] Higher magnification STM images of the graphene films on Ir(111) also feature triangular shapes, not present in pristine graphene; see figure 5.3(d). These features have previously been identified as signatures of N dopants.[45]

As evidenced by the STM images shown in figure 5.3(e-f), graphene films on Ir(111) could also be grown using Pyr as the precursor molecule. Despite the fact that this molecule has a significantly higher N to C ratio, the concentration of dopant atoms

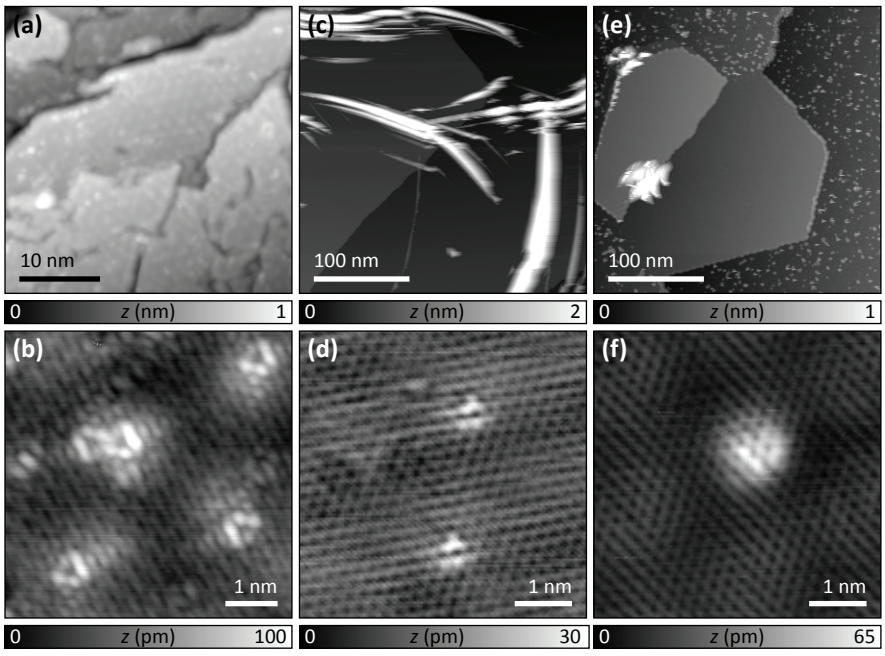

Figure 5.3 (a-b) Overview and zoom of graphene on Cu(111) grown with Phen precursor molecules. **(a)** STM set-point 20 pA at 100 mV. **(b)** STM set-point 50 pA at 1.0 V. Dopant concentration is approximately 1%. **(c-d)** Overview and zoom of graphene on Ir(111) grown with Phen precursor molecules. **(c)** STM set-point 1 nA at 100 mV. **(d)** STM set-point 1 nA at 100 mV. Dopant concentration is less than 1%. **(e-f)** Overview and zoom of graphene on Ir(111) grown with Pyr precursor molecules. **(e)** STM set-point 1 nA at 100 mV. **(f)** STM set-point 500 pA at 100 mV. Dopant concentration is less than 1%.

was found to be of the same order of magnitude as that of the graphene sheets grown with Phen. In the films grown with Pyr molecules, we encountered triangular-shaped features with a significantly larger spatial extension, as shown in figure 5.3(f). Similar features have previously been attributed to two N atoms in close proximity.[22,23]

5.3.2 Signatures of dopant N atoms

The fact that the N dopants have a well-defined signature in STM images means that we can use this data to benchmark the AFM data; *i.e.*, by sequentially acquiring an STM and AFM image of the same area, the location of the N atom in the graphene can be pinpointed.

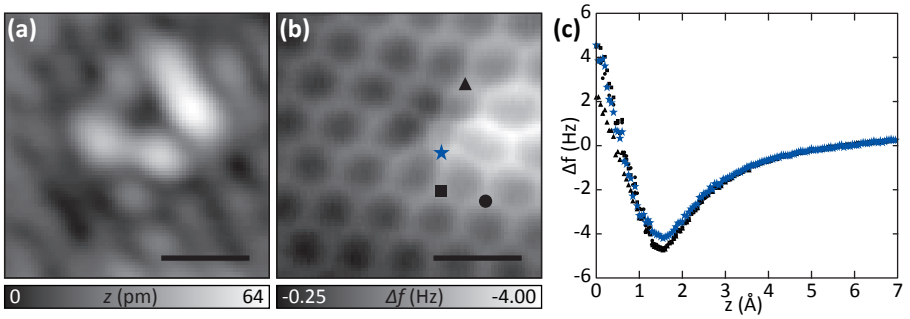

Figure 5.4 (a) STM image of an N-dopant in graphene on Cu(111), set-point 50 pA at 1.0 V. **(b)** Constant height AFM image of the same location at -20 pm w.r.t. STM set-point. **(c)** $\Delta f(z)$ curves obtained over the positions as indicated in (b). Scale bars are 5 Å.

Figure 5.4(a-b) shows an STM and AFM image of the same area of a N-doped graphene film on Cu(111). Again, the STM image shows a clear feature due to the N atom. However, it is not possible to determine the location of the N atom directly from the STM or the AFM images. The STM image is not atomically resolved at the location of and in the immediate surrounding of the dopant atom. In contrast, the six-membered rings of the graphene lattice are clearly resolved in the AFM image. Interestingly, in the vicinity of the N atom, the six-membered rings appear heavily distorted.

From DFT calculations the lateral stretching in the graphene network induced by the substitutional dopant is only about 1% in compression to the nearest-neighbor distance. Thus these distortions are imaging artifacts and are most likely due to the electrostatic interaction between the dopant atom, which has a partial positive charge, and the dipole moment of the tip,[40,42,46,47] see also chapter 4. A Bader charge analysis shows that the N atom has a charge of 1.27 e, where 73% of that charge is extracted from the 3 neighboring C atoms, donating 0.3 e each to the N atom.

The proposed location of the N atom in the AFM image, indicated by the blue star marker in figure 5.4(b), is not at the center of the triangular signature of the STM image, despite the fact that the two images, figures 5.4(a) and 5.4(b), are obtained over exactly the same location. Due to tip geometry the location where the signature currents are observed can be slightly offset with respect to the location of the lattice

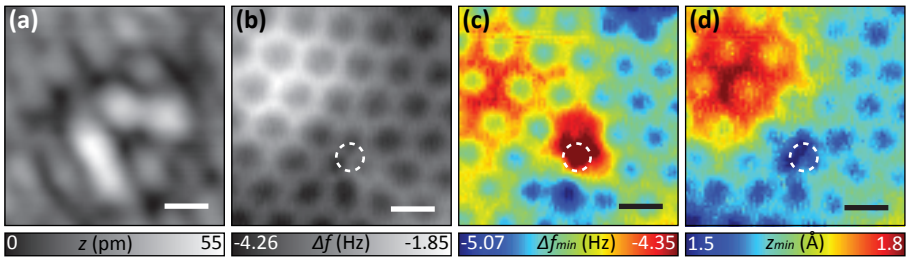

Figure 5.5 (a) STM image of an N-dopant in graphene on Cu(111), set-point 50 pA at 1.0 V. **(b)** Constant height AFM image of the same location at -20 pm w.r.t. STM set-point. **(c)** Δf_{min} map of the same area. **(d)** Corresponding z_{min} map, where 0 corresponds to -20 pm w.r.t. STM set-point. Scale bars are 3 Å.

sites as measured by AFM. The region of less negative frequency shift values at the right-hand side of the image is due to the vertical corrugation of the film.[33,48]

We acquired several $\Delta f(z)$ curves at atoms that should have (approximately) the same height above the surface; see the markers in figure 5.4(b). The spectra are shown in figure 5.4(c). Note that the spectra on three equivalent C atoms overlap, whereas the spectrum taken above the N atom is significantly different. In particular, the minimum of the $\Delta f(z)$ curve over an N atom is less negative than over a C atom at an equivalent position in the lattice. This trend was observed for different tips. This demonstrates that the method used by Sugimoto *et al.*,[35] where AFM can be used to discriminate atoms, can be successfully extended to N and C atoms in graphene on Cu(111).

To investigate the effect of the dopant on the potential-energy landscape as probed by the AFM, a Δf data cube was acquired by taking a series of constant-height AFM images at increasing tip-sample distance. From this data cube, a $\Delta f(z)$ spectrum and therefore the coordinates of the minimum, Δf_{min} and z_{min}, can be extracted for every pixel.[30]

Figure 5.5(a-b) shows STM and AFM images obtained over the same location. In the STM image, the characteristic feature of a N dopant is observed, while in the AFM image six membered rings can be seen. Again, there are image distortions close to the N dopant. The Δf_{min} and z_{min} maps extracted from a Δf data cube are shown in figures 5.5(c) and (d), respectively. From the Δf_{min} map it is clear that the effect of the N atom

on the minimum Δf follows the same trend as before: the minimum Δf above the N atom is generally less negative than over C atoms. This effect is not localized on a single atom. This is attributed to the influence of the partially charged N atom on the charge density of the atoms to which it is bound.[24] At the location of the dopant atom there is also some contrast in the z_{min} map. In particular, the tip has to approach the N atom more closely to reach the minimum of the $\Delta f(z)$ curve.

The Δf_{min} and z_{min} maps exhibit a larger region of contrast (less negative frequency shift and larger tip-sample distance). As can be seen by comparing the maps to the constant-height AFM image, this region coincides with a top site of the moiré pattern. The fact that the geometric structure of the sample influences the Δf_{min} map can be rationalized as follows: due to the corrugation of the graphene, the van der Waals (vdW) attraction between the bulk of the tip and the graphene differs between top and valley sites; *i.e.*, in a valley site the tip will experience a larger vdW attraction from the surrounding top sites, while at a top site the surrounding valleys are farther away, resulting in a smaller vdW attraction.

5.3.3 Influence of the substrate

To investigate the general applicability of this approach and to study the influence of the sample-substrate interaction, we performed the same experiments on N-doped graphene grown on an Ir(111) surface. Graphene on Ir(111) is physisorbed, but exhibits a chemical modulation.[10] The C atoms located at top sites of the moiré pattern have a weak vdW interaction with the substrate, while the atoms in the hcp site form a weak covalent bond to the surface. This provides the opportunity to investigate the influence of the interaction between the surface and the species of interest on the chemical recognition by AFM.

First, we present N-doped graphene on Ir(111) made with precursor Phen in figure 5.6(a-d). A unit cell of the moiré lattice is overlaid on the images to indicate the positions of the dopant atoms relative to their position in the moiré pattern. From the STM image, figure 5.6(a), we can see that there are two N dopants at approximately the same lattice positions with respect to the moiré pattern, namely an hcp site. Consequently, they have a similar effect on the surrounding energy landscape. In the

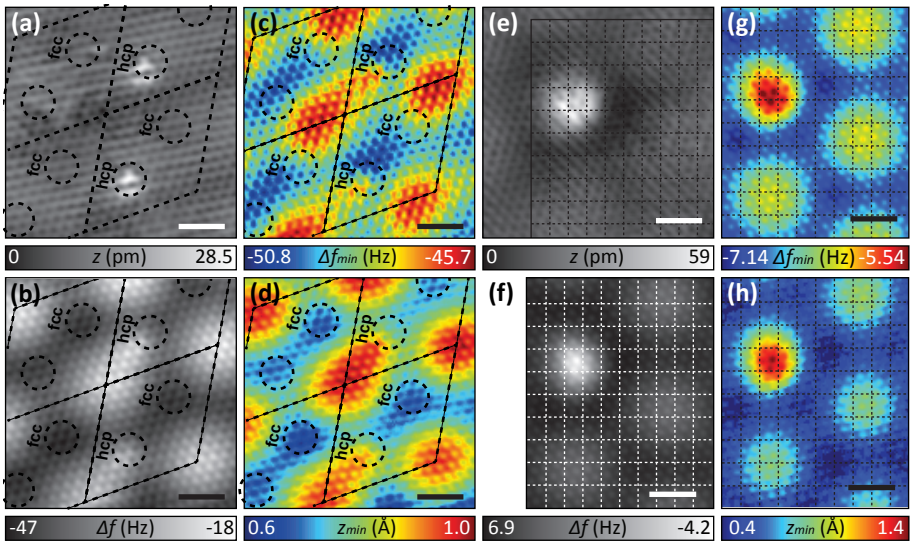

Figure 5.6 (a) STM image of a N-dopant in graphene on Ir(111) grown with Phen, at set-point 1 nA at 100 mV. **(b)** Constant height AFM image of the same location at -100 pm w.r.t. STM set-point. **(c)** Δf_{min} map of the same area. **(d)** Corresponding z_{min} map. **(e)** STM image of a N-dopant in graphene on Ir(111) grown with Pyr, at set-point 500 pA at 100 mV. **(f)** Constant height AFM image of the same location at -150 pm w.r.t. STM set-point. **(g)** Δf_{min} map of the same area. **(h)** Corresponding z_{min} map. Scale bars are 1 nm.

AFM image, figure 5.6(b), the top sites appear elongated towards the positions of the dopants. The elongation effect cannot be caused by an asymmetry of the tip as top sites that do not have a N atom in an adjacent hcp site (right and left side of the image) do not show the elongation. A similar elongation is found in the Δf_{min} and z_{min} maps shown in figure 5.6(c-d). As was observed for N-doped graphene on Cu(111), Δf_{min} is significantly less negative over the N atom than over C atoms located at the same position in the moiré unit cell.

If we overlay the moiré lattice extracted from the constant height AFM image onto the Δf_{min} and z_{min} maps, there is a significant mismatch for the former; *i.e.*, the locations of least negative frequency shift appear shifted with respect to the positions of the top sites of the moiré lattice. In contrast, the moiré lattice extracted from the AFM image fits the z_{min} map, which was extracted from the same data as the Δf_{min} map, quite well.

The shift in the Δf_{min} map is most likely caused by an asymmetry in the mesoscopic tip shape. If the tip is asymmetric at this length scale, the vdW attraction will also be asymmetric. The same argumentation, used to explain why the corrugation of the surface is visible in the Δf_{min} map, explains why the moiré top positions appear shifted in the Δf_{min} map. Important to note here is that only the apparent positions of the top and valley sites have changed: the actual moiré pattern positions, as well as the locations of the dopant atoms, remain the same. The characteristic contrast of the N atoms is still at their hcp locations in the overlaid moiré grid, where the Δf_{min} for N is less negative than for the surrounding C atoms.

Figures 5.6(e-h) show results from a set of experiments performed on N-doped graphene grown using Pyr. Interestingly, the STM signature is very different from that shown in figure 5.6(a) and has a significantly larger spatial extension. From the AFM image, it is concluded that the feature observed in the STM channel is located at the top site of the moiré lattice. Previously, a very similar signature in STM images was attributed to two N atoms on neighboring positions on the same sub lattice, *i.e.* with one N atom in the meta position with respect to the other.[23]

Figures 5.6(g) and (h) show the Δf_{min} and z_{min} maps. Also in this case, the area where the N atoms are expected to be has a clearly different signature in both maps compared to C-only top sites of the moiré lattice. Note that the difference between the top sites in the z_{min} map is much larger than typical variations observed between identical top sites,[34] reinforcing the assignment that the feature observed in the STM image is due to incorporation of (multiple) N atoms at that site.

The contrast over the rings/atoms is reversed in figures 5.6(b-d) in comparison to figures 5.6(f)–6(h). That is, in figures 5.6(b-d), the centers of the hexagonal rings are more attractive (larger negative frequency shift) than the apparent bonds, whereas this trend is reversed in figures 5.6(f-h). The contrast inversion in constant-height AFM images of graphene has been reported before and is due to the offsets in the $\Delta f(z)$ curves acquired over apparent bonds and the center of the hexagons.[15]

5.3.4 Comparison to DFT simulations

To corroborate the experimental findings, we performed DFT calculations. In particular, we simulated $\Delta f(z)$ curves obtained for N-doped graphene on Ir(111). We chose to model graphene on Ir(111) because of its well-defined moiré pattern that can be modeled well by a periodic supercell, taking (10×10) unit cells of graphene on (9×9) cells of Ir(111).[10,33] We simulated $\Delta f(z)$ curves for N and C atoms in two distinctive positions in the moiré pattern. These are the top and hcp sites of the moiré unit cell, as indicated in figure 5.2(a). At the top sites, the interaction between graphene and Ir(111) is mainly due to vdW interactions, whereas at the hcp sites a weak covalent bond is formed between C atoms and the underlying Ir atoms.[10]

The results of the energy-distance calculations, as well as the corresponding fits to a Morse potential, are shown in figure 5.7(a-b). The blue curves are for an N atom, the black curves for a C atom in the same position. From these curves we calculated the corresponding $\Delta f(z)$ curves, see figure 5.7(c-d).

For both the top and hcp sites, the simulated $\Delta f(z)$ curves are clearly distinct for N and C; Δf_{min} is significantly less negative above N compared to C, in qualitative agreement with our experimental observations for N-doped graphene on both Cu(111) and Ir(111). The value of $\Delta f_{min,C} - \Delta f_{min,N}$ differs between simulation and experiments and also between the experiments, being approximately 10 Hz, 0.5 Hz, 3 Hz, and 1 Hz for the simulation and the Cu(111) and two Ir(111) experiments, respectively. The fact that the experimental values for the difference between N and C (data acquired with different tips) are not identical points to the importance of the chemical composition and geometry of the tip apex. As stated earlier, we only used one tip geometry and composition in the DFT calculations. It is likely that the electrostatic contribution is underestimated. Furthermore, uncertainties in the experimental parameters needed to convert the calculated $E(z)$ curves to $\Delta f(z)$ curves contributes to the observed discrepancy between the experimental and simulated values of the frequency shift. Because of the above, we only focus on qualitative trends in the DFT results.

Note that the z-position of the minimum is shifted towards the surface (smaller z value) for the hcp site, in agreement with the vertical corrugation of the moiré pattern. These findings imply that the surface-graphene interaction has a negligible influence

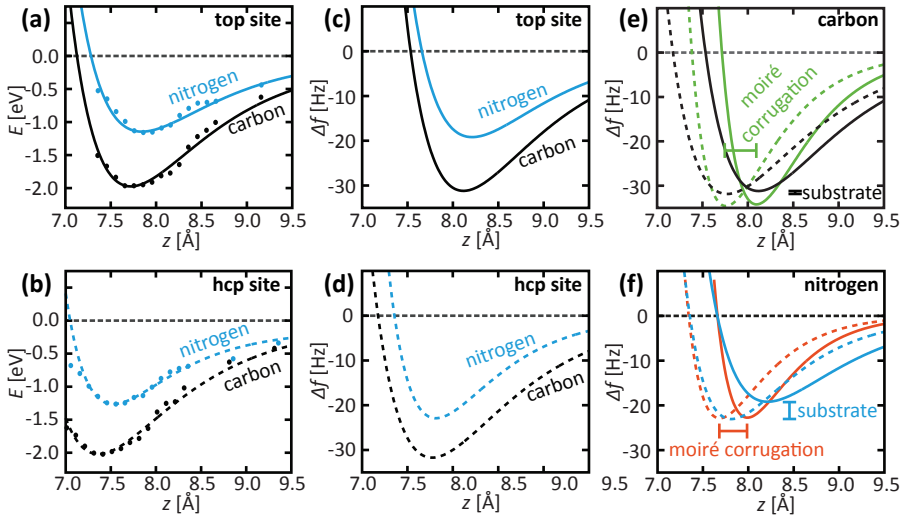

Figure 5.7 Energy-distance DFT calculations for N-doped graphene on Ir(111). *z* is the vertical distance between the average height of the atoms in the top-most Ir layer in the Ir(111) substrate and the height of the top-most Ir atoms of the tip model. **(a)** Comparison between N and C at a top site. **(b)** Comparison between N and C at an hcp site. **(c)** $\Delta f(z)$ curves calculated from the energy-distance curves comparing N and C at a top site. **(d)** $\Delta f(z)$ curves calculated from the energy-distance curves comparing N and C at a hcp site. **(e)** Comparison between C atoms at top (solid lines) and hcp (dashed lines) sites, with Ir(111) substrate (black) and without Ir(111) substrate (green). **(f)** Comparison between N atoms at top (solid lines) and hcp (dashed lines) sites, with Ir(111) substrate (blue) and without Ir(111) substrate (orange).

on the chemical recognition of N-dopants in graphene on Ir(111).

The same trend is found in the simulations and in the copper and iridium experiments, which is a good indication that the observed trend (Δf_{min} is less negative for a N atom than for a C atom) is robust, regardless of location or substrate. We should note that Telychko *et al.* found the reverse relationship;[24] however their experiments employed a silicon carbide surface instead of the metallic surfaces presented in this paper.

We theoretically investigated the effect of the substrate. This was done by performing similar calculations to those described above using a graphene sheet without

underlying substrate, but having the same moiré corrugation as in the case of the simulations including the Ir(111) substrate, and comparing the results to those obtained for the calculations including the substrate.

The resulting curves for the C atom are shown in figure 5.7(e). Black lines correspond to the results obtained from calculations including the substrate, these are reproduced from figure 5.7(c-d), whereas green lines are the results obtained from the simulations without the substrate. Figure 5.7(f) shows the same, but for the N atom, where the blue lines are for calculations that include the Ir(111) substrate, these are again reproduced from figure 5.7(c-d), and the orange curves are calculated without substrate. The solid lines correspond to spectra over atoms at a top site, while the dashed lines correspond to $\Delta f(z)$ curves simulated over an hcp site.

First, we will discuss the results obtained for C, figure 5.7(e). For the calculation including substrate, the z position of the minimum for C atoms in hcp and top sites is shifted to smaller z (compare dashed and solid black lines). As can be inferred from Table I, the difference in z between top and hcp sites is approximately 0.32 Å. This corresponds very well to the shift in z of the minimum (indicated by the green bar). Removing the substrate from the calculation does not affect the position of the minimum in z (compare black and green lines). This implies that the position of the minimum reflects the corrugation of the sample.

The depth of the minimum, *i.e.*, Δf_{min}, is virtually identical for top and hcp sites for simulations with (compare solid and dashed black lines) and without the Ir(111) (compare solid and dashed green lines). The difference in Δf_{min} in the calculations (black bar) is much smaller than what is found experimentally. This is attributed to the underestimation of the vdW contribution by the small Ir_4 cluster used as the model for the tip in the DFT calculation. In the calculations the additional vdW attraction caused by the bulk tip was only accounted for by a homogeneous offset. Note that the absolute value for Δf_{min} does differ for calculations with (black) and without (green) substrate. This offset is due to the vdW interaction between the tip and the Ir atoms of the substrate. From this result, we infer that the interaction between the tip and a C atom in graphene/Ir(111) is (almost) unaffected by the interaction between graphene and the Ir(111).

Table II Corrugation of the N-doped graphene moiré pattern on Ir(111) for different dopant positions. Bold numbers indicate that the atom considered in that specific high-symmetry position is a nitrogen.

N position	Δh_{Ir} (Å)	h_{top} (Å)	h_{fcc} (Å)	h_{hcp} (Å)	h_{bridge} (Å)	$\bar{h}$ (Å)	Δh (Å)
Pristine	0.027	3.633	3.318	3.311	3.323	3.403	0.343
N at top	0.031	**3.633**	3.323	3.311	3.326	3.401	0.345
N at fcc	0.047	3.629	**3.383**	3.321	3.327	3.405	0.341
N at hcp	0.048	3.630	3.330	**3.374**	3.334	3.405	0.332
N at bridge	0.042	3.630	3.331	3.334	**3.382**	3.404	0.332

Next, we turn our attention to the N atom, figure 5.7(f). Again, the moiré corrugation results in a shift of z_{min} between top (solid) and hcp (dashed) sites, indicated by the orange bar. This is observed for calculations with (blue) and without (orange) substrate. Table II gives key heights for the moiré corrugation of graphene with N dopant atoms at various sites. From this table it can be seen that the moiré corrugation is hardly disturbed by the dopant atoms. N dopants at top sites appear at the same height as their C counterparts in pristine graphene. For the other three sites we see that the N dopants protrude a few pm with respect to the original position of C in pristine graphene. Furthermore, the C-N distances are virtually identical to the C-C distances (1% contraction). Hence, we ascribe the shift in z_{min} between top (solid) and hcp (dashed) lines to the moiré corrugation.

Now focus on Δf_{min} for the calculation without substrate (orange curves). The depth of the minimum, *i.e.*, Δf_{min}, is the same for atoms in hcp and top sites. This is consistent with the fact that in the absence of the substrate, the N atoms in the different sites are chemically equivalent and have equal surroundings. As established for C previously, the vertical corrugation of the graphene itself leads to only a very small change in the depth of the minimum.

Turning to the calculation including the substrate (blue lines), the Δf_{min} is significantly less negative for the top site (solid blue), than for the hcp site (dashed blue). Because this difference is only observed for the calculation with substrate, this difference must be due to the interaction between the Ir(111) substrate and the N-dopant atom at the hcp site, an interaction that is absent between a C atom at an hcp

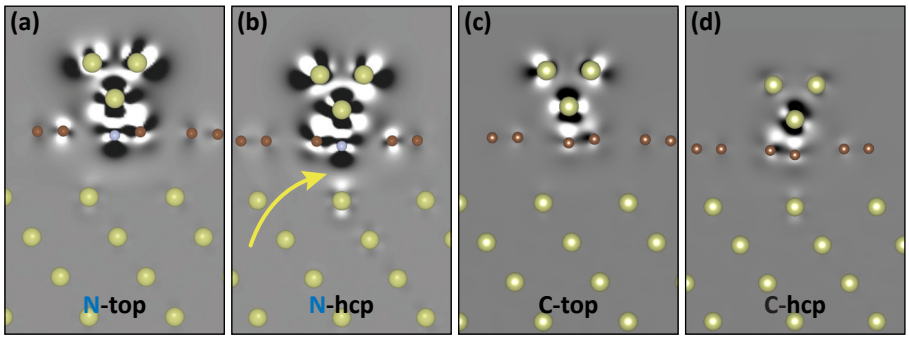

Figure 5.8 Charge density difference $\Delta\rho = \rho_{tip,S} - \rho_{tip} - \rho_{S}$, plotted in (e/Å3), for N at **(a)** top or **(b)** hcp sites, and for pristine graphene at **(c)** top and **(d)** hcp sites. ρ_{S} is the charge density of the isolated (N-doped) graphene/Ir(111) system, ρ_{tip} is the charge density of the isolated model tip, and $\rho_{tip,S}$ is the charge density of the overall system, with the tip at small distance from the surface. The color scale ranges from -0.013 e/Å3 (black; loss in electron density) to 0.013 e/Å3 (white; gain in electron density), passing through zero (gray). The charge densities have been calculated after allowing the tip apex, the probed atom in the graphene layer and its three nearest-neighbors to relax. Ir, C and N atoms are marked in green, brown and blue, respectively. The yellow arrow highlights the relatively stronger chemical bond which is formed between N and Ir(111) at the hcp site.

site and the Ir(111) substrate.

Figure 5.8 shows the electron density difference maps of a side view of the tip (at $z = z_{min}$), the N-doped graphene or pristine graphene, and the Ir substrate. The yellow arrow in figure 5.8(b) points to the area between the N dopant at the hcp site and the Ir substrate. There is a significant redistribution of electron density difference in the area between the N atom in the hcp site and the underlying substrate. In contrast, such a redistribution is not observed for the N atom in a top site of the moiré lattice; see figure 5.8(a). The electron density difference maps of pristine graphene shown in figure 5.8(c-d) confirm our conclusions about the lack of interaction between the Ir(111) substrate and a C atom in both the top and hcp sites.

5.4 Conclusion

In summary, we have explored the capabilities and performance of AFM for the

identification and characterization of N dopants in graphene. Using chemical vapor deposition, we grew graphene on Cu(111) and Ir(111) surfaces using two different N containing precursor molecules. In all cases, clear signatures of N atoms incorporated in the lattice where observed in STM images. These were used as a benchmark for the AFM experiments. For both substrates, the $\Delta f(z)$ curves acquired with metallic tips above N and C located at similar positions with respect to the moiré lattice exhibit significant differences. In particular, the coordinates of the minimum, Δf_{min}, and z_{min} were found to contain information on the chemical nature of the atom above which the curve was acquired. The experimental findings are reproduced using DFT calculations. We expect the method described above to also be applicable to other dopants.

5.5 References

[1] K. S. Novoselov, A. K. Geim, S. V. Morozov, D. Jiang, Y. Zhang, S. V. Dubonos, I. V. Grigorieva, A. A. Firsov, Electric Field Effect in Atomically Thin Carbon Films. *Science.* **306**, 666–669 (2004).

[2] T. Schiros et al., Connecting Dopant Bond Type with Electronic Structure in N-Doped Graphene. *Nano Lett.* **12**, 4025–4031 (2012).

[3] H. Wang, T. Maiyalagan, X. Wang, Review on Recent Progress in Nitrogen-Doped Graphene: Synthesis , Characterization , and Its Potential Applications. *ACS Catal.* **2**, 781–794 (2012).

[4] R. R. Cloke, T. Marangoni, G. D. Nguyen, T. Joshi, D. J. Rizzo, C. Bronner, T. Cao, S. G. Louie, M. F. Crommie, F. R. Fischer, Site-Specific Substitutional Boron Doping of Semiconducting Armchair Graphene Nanoribbons. *J. Am. Chem. Soc.* **137**, 8872–8875 (2015).

[5] S. Kawai, S. Saito, S. Osumi, S. Yamaguchi, A. S. Foster, P. Spijker, E. Meyer, Atomically controlled substitutional boron-doping of graphene nanoribbons. *Nat. Commun.* **6**, 8098 (2015).

[6] S. Stankovich, D. a. Dikin, R. D. Piner, K. a. Kohlhaas, A. Kleinhammes, Y. Jia, Y. Wu, S. T. Nguyen, R. S. Ruoff, Synthesis of graphene-based nanosheets via chemical reduction of exfoliated graphite oxide. *Carbon N. Y.* **45**, 1558–1565 (2007).

[7] A. T. N'Diaye, M. Engler, C. Busse, D. Wall, N. Buckanie, F.-J. Meyer zu Heringdorf, R. van Gastel, B. Poelsema, T. Michely, Growth of graphene on Ir(111). *New J. Phys.* **11**, 23006 (2009).

[8] A. Deshpande, W. Bao, F. Miao, C. N. Lau, B. J. LeRoy, Spatially resolved spectroscopy of monolayer graphene on SiO2. *Phys. Rev. B.* **79**, 205411 (2009).

[9] L. Gao, J. R. Guest, N. P. Guisinger, Epitaxial Graphene on Cu(111). *Nano Lett.* **10**, 3512–3516 (2010).

[10] C. Busse, P. Lazić, R. Djemour, J. Coraux, T. Gerber, N. Atodiresei, V. Caciuc, R. Brako, A. T. N'Diaye, S. Blügel, J. Zegenhagen, T. Michely, Graphene on Ir(111): Physisorption with Chemical Modulation. *Phys. Rev. Lett.* **107**, 36101 (2011).

[11] R. Decker, Y. Wang, V. W. Brar, W. Regan, H. Tsai, Q. Wu, W. Gannett, A. Zettl, M. F. Crommie, Local Electronic Properties of Graphene on a BN Substrate via Scanning Tunneling

Microscopy. *Nano Lett.* **11**, 2291–2295 (2011).
[12] J. Xue, J. Sanchez-Yamagishi, D. Bulmash, P. Jacquod, A. Deshpande, K. Watanabe, T. Taniguchi, P. Jarillo-Herrero, B. J. LeRoy, Scanning tunnelling microscopy and spectroscopy of ultra-flat graphene on hexagonal boron nitride. *Nat. Mater.* **10**, 282–285 (2011).
[13] M. M. Ugeda, D. Fernández-Torre, I. Brihuega, P. Pou, a. J. Martínez-Galera, R. Pérez, J. M. Gómez-Rodríguez, Point defects on graphene on metals. *Phys. Rev. Lett.* **107**, 1–5 (2011).
[14] H. Wang, Q. Wang, Y. Cheng, K. Li, Y. Yao, Q. Zhang, C. Dong, P. Wang, U. Schwingenschlögl, W. Yang, X. X. Zhang, Doping monolayer graphene with single atom substitutions. *Nano Lett.* **12**, 141–144 (2012).
[15] M. P. Boneschanscher, J. Van Der Lit, Z. Sun, I. Swart, P. Liljeroth, D. Vanmaekelbergh, Quantitative atomic resolution force imaging on epitaxial graphene with reactive and nonreactive AFM probes. *ACS Nano.* **6**, 10216–10221 (2012).
[16] N. Néel, J. Kröger, L. Limot, T. Frederiksen, M. Brandbyge, R. Berndt, Controlled Contact to a C60 Molecule. *Phys. Rev. Lett.* **98**, 65502 (2007).
[17] X. Li, X. Wang, L. Zhang, S. Lee, H. Dai, Chemically Derived Ultramooth Graphene Nanoribbon Semiconductors. *Science.* **319**, 1229–1232 (2008).
[18] J. Cai, P. Ruffieux, R. Jaafar, M. Bieri, T. Braun, S. Blankenburg, M. Muoth, A. P. Seitsonen, M. Saleh, X. Feng, K. Müllen, R. Fasel, Atomically precise bottom-up fabrication of graphene nanoribbons. *Nature.* **466**, 470–473 (2010).
[19] S. J. Altenburg, J. Kröger, T. O. Wehling, B. Sachs, A. I. Lichtenstein, R. Berndt, Local Gating of an Ir(111) Surface Resonance by Graphene Islands. *Phys. Rev. Lett.* **108**, 206805 (2012).
[20] Y. C. Chen, D. G. De Oteyza, Z. Pedramrazi, C. Chen, F. R. Fischer, M. F. Crommie, Tuning the band gap of graphene nanoribbons synthesized from molecular precursors. *ACS Nano.* **7**, 6123–6128 (2013).
[21] J. van der Lit, P. H. Jacobse, D. Vanmaekelbergh, I. Swart, Bending and buckling of narrow armchair graphene nanoribbons via STM manipulation. *New J. Phys.* **17**, 53013 (2015).
[22] R. Lv et al., Nitrogen-doped graphene: beyond single substitution and enhanced molecular sensing. *Sci. Rep.* **2**, 1–8 (2012).
[23] M. Telychko, P. Mutombo, M. Ondráček, P. Hapala, F. C. Bocquet, J. Kolorenč, M. Vondráček, P. Jelínek, M. Švec, Achieving High-Quality Single-Atom Nitrogen Doping of Graphene/SiC(0001) by Ion Implantation and Subsequent Thermal Stabilization. *ACS Nano.* **8**, 7318–7324 (2014).
[24] M. Telychko, P. Mutombo, P. Merino, P. Hapala, M. Ondráček, F. C. Bocquet, J. Sforzini, O. Stetsovych, M. Vondráček, P. Jelínek, M. Švec, Electronic and Chemical Properties of Donor, Acceptor Centers in Graphene. *ACS Nano.* **9**, 9180–9187 (2015).
[25] A. Zabet-Khosousi, L. Zhao, L. Pálová, M. S. Hybertsen, D. R. Reichman, A. N. Pasupathy, G. W. Flynn, Segregation of Sublattice Domains in Nitrogen-Doped Graphene. *J. Am. Chem. Soc.* **136**, 1391–1397 (2014).
[26] K. Kim, S. Yang, Y. Park, M. Lee, B. Kim, H. Lee, Annealing Effects after Nitrogen Ion Casting on Monolayer and Multilayer Graphene. *J. Phys. Chem. C.* **117**, 2129–2134 (2013).
[27] H. Hölscher, W. Allers, U. D. Schwarz, A. Schwarz, R. Wiesendanger, Interpretation of "true atomic resolution" images of graphite (0001) in noncontact atomic force microscopy. *Phys. Rev. B.* **62**, 6967–6970 (2000).
[28] S. Hembacher, F. J. Giessibl, J. Mannhart, C. F. Quate, Revealing the hidden atom in graphite by low-temperature atomic force microscopy. *Proc. Natl. Acad. Sci.* **100**, 12539–12542 (2003).

[29] S. Hembacher, F. J. Giessibl, J. Mannhart, C. F. Quate, Local Spectroscopy and Atomic Imaging of Tunneling Current, Forces, and Dissipation on Graphite. *Phys. Rev. Lett.* **94**, 56101 (2005).
[30] B. J. Albers, T. C. Schwendemann, M. Z. Baykara, N. Pilet, M. Liebmann, E. I. Altman, U. D. Schwarz, Three-dimensional imaging of short-range chemical forces with picometre resolution. *Nat. Nanotechnol.* **4**, 307–310 (2009).
[31] M. Ondráček, P. Pou, V. Rozsíval, C. González, P. Jelínek, R. Pérez, Forces and Currents in Carbon Nanostructures: Are We Imaging Atoms? *Phys. Rev. Lett.* **106**, 176101 (2011).
[32] Z. Sun, S. K. Hämäläinen, J. Sainio, J. Lahtinen, D. Vanmaekelbergh, P. Liljeroth, Topographic and electronic contrast of the graphene moiré on Ir(111) probed by scanning tunneling microscopy and noncontact atomic force microscopy. *Phys. Rev. B.* **83**, 81415 (2011).
[33] E. N. Voloshina, E. Fertitta, A. Garhofer, F. Mittendorfer, M. Fonin, A. Thissen, Y. S. Dedkov, Electronic structure and imaging contrast of graphene moiré on metals. *Sci. Rep.* **3**, 1072 (2013).
[34] S. K. Hämäläinen, M. P. Boneschanscher, P. H. Jacobse, I. Swart, K. Pussi, W. Moritz, J. Lahtinen, P. Liljeroth, J. Sainio, Structure and local variations of the graphene moiré on Ir(111). *Phys. Rev. B.* **88**, 201406 (2013).
[35] Y. Sugimoto, P. Pou, M. Abe, P. Jelinek, R. Pérez, S. Morita, O. Custance, Chemical identification of individual surface atoms by atomic force microscopy. *Nature.* **446**, 64–67 (2007).
[36] P. E. Blöchl, Projector augmented-wave method. *Phys. Rev. B.* **50**, 17953–17979 (1994).
[37] G. Kresse, J. Furthmüller, Efficient iterative schemes for ab initio total-energy calculations using a plane-wave basis set. *Phys. Rev. B.* **54**, 11169–11186 (1996).
[38] J. P. Perdew, K. Burke, M. Ernzerhof, Generalized Gradient Approximation Made Simple. *Phys. Rev. Lett.* **77**, 3865–3868 (1996).
[39] D. Vanderbilt, Soft self-consistent pseudopotentials in a generalized eigenvalue formalism. *Phys. Rev. B.* **41**, 7892–7895 (1990).
[40] S. Grimme, Density functional theory with London dispersion corrections. *Wiley Interdiscip. Rev. Comput. Mol. Sci.* **1**, 211–228 (2011).
[41] S. Grimme, J. Antony, S. Ehrlich, H. Krieg, A consistent and accurate ab initio parametrization of density functional dispersion correction (DFT-D) for the 94 elements H-Pu. *J. Chem. Phys.* **132**, 154104 (2010).
[42] D. Z. Gao, J. Grenz, M. B. Watkins, F. Federici Canova, A. Schwarz, R. Wiesendanger, A. L. Shluger, Using Metallic Noncontact Atomic Force Microscope Tips for Imaging Insulators and Polar Molecules: Tip Characterization and Imaging Mechanisms. *ACS Nano.* **8**, 5339–5351 (2014).
[43] F. J. Giessibl, Forces and frequency shifts in atomic-resolution dynamic-force microscopy. *Phys. Rev. B.* **56**, 16010–16015 (1997).
[44] L. Zhao *et al.*, Visualizing Individual Nitrogen Dopants in Monolayer Graphene. *Science.* **333**, 999–1003 (2011).
[45] D. Wei, Y. Liu, Y. Wang, H. Zhang, L. Huang, G. Yu, Synthesis of N-Doped Graphene by Chemical Vapor Deposition and Its Electrical Properties. *Nano Lett.* **9**, 1752–1758 (2009).
[46] J. van der Lit, F. Di Cicco, P. Hapala, P. Jelinek, I. Swart, Submolecular Resolution Imaging of Molecules by Atomic Force Microscopy: The Influence of the Electrostatic Force. *Phys. Rev. Lett.* **116**, 96102 (2016).
[47] P. Hapala, M. Švec, O. Stetsovych, N. J. van der Heijden, M. Ondráček, J. van der Lit, P. Mutombo, I. Swart, P. Jelínek, Mapping the electrostatic force field of single molecules from high-resolution scanning probe images. *Nat. Commun.* **7**, 11560 (2016).

[48] M. P. Boneschanscher, S. K. Hämäläinen, P. Liljeroth, I. Swart, Sample Corrugation Affects the Apparent Bond Lengths in Atomic Force Microscopy. *ACS Nano.* **8**, 3006–3014 (2014)

6

Characteristic contrast in Δf_{min} maps of organic molecules using AFM

abstract

Scanning tunneling microscopy and atomic force microscopy can provide detailed information about the geometric and electronic structure of molecules with sub-molecular spatial resolution. However, an essential capability to realize the full potential of these techniques for chemical applications is missing from the scanning probe toolbox: chemical recognition of organic molecules. Here, we show that maps of the minima of frequency shift-distance curves extracted from 3D data cubes contain characteristic contrast. A detailed theoretical analysis based on density functional theory and molecular mechanics shows that these features are characteristic for the investigated species. Structurally similar but chemically distinct molecules yield significantly different features. We find that the van der Waals and Pauli interaction, together with the specific adsorption geometry of a given molecule on the surface, accounts for the observed contrast.

based on

Nadine J. van der Heijden, Prokop Hapala, Jeroen A. Rombouts, Joost van der Lit, Daniël Smith, Pingo Mutombo, Martin Svec, Pavel Jelinek, and Ingmar Swart, *ACS Nano* **10**, 8517-8525 (2016)

6.1 Introduction

Scanning tunneling microscopy (STM) and atomic force microscopy (AFM) are both capable of imaging molecules with sub-molecular resolution.[1–5] In addition, both techniques can provide quantitative information: STM on the electronic structure and AFM on the charge distribution and the bond orders.[5–8] Hence, both techniques find increasing use in the field of chemistry. To realize the full potential of STM and AFM in studies involving molecules, the ability to identify or recognize molecules is of great value. STM provides chemical recognition capabilities via inelastic electron tunneling spectroscopy via differences in the local density of states and vibration frequencies of bonds.[9–12] Force-distance spectroscopy, combined with density functional theory (DFT) calculations, has been used to chemically identify atoms in surfaces of insulators, alloys, and semiconductors.[13–19] In most cases, the origin of the chemical contrast is due to formation of atom-specific covalent bonds with the tip. However, sub-molecular resolution imaging of molecules requires the use of chemically passivated tips to avoid an accidental pickup of the molecule of interest. Hence, chemical recognition of atoms within an organic molecule has to rely on a different contrast mechanism. Contrast differences in AFM images over various chemical elements in organic molecules have been observed, indicating that elemental identification may be possible.[20–22] Thus far, chemical recognition with AFM has mostly relied on structural arguments.[20–22]

The chemical identification procedure for atoms in an alloy surface[14] cannot be transferred to recognize organic molecules adsorbed on a surface. First, the chemical contrast observed on surfaces is due to the formation of a (partial) covalent bond between the reactive metal tip and the atoms under investigation. This is in direct conflict with the requirement to use chemically passivated tips. Another complication that hampers direct chemical identification of atoms in molecules by comparing frequency shift-distance ($\Delta f(z)$) spectra is the fact that the van der Waals (vdW) force varies strongly over a single molecule on a surface.[23] Hence, $\Delta f(z)$ spectra acquired over identical elements in a molecule, one at the center and the other at the periphery, will be significantly different. This is especially important because for most organic molecules the majority of the atoms reside at the periphery. However, it is important to realize that chemical recognition of molecules does not require each atom in a

molecule to be identified separately. Instead, it is sufficient if the molecule as a whole exhibits some characteristic contrast. Since the overall magnitude and shape of the potential energy landscape experienced by the tip should reflect both the geometry and the chemical composition of the molecule, it may be possible to chemically recognize molecules on surfaces with AFM.

Here, we present a proof-of-concept study that demonstrates that maps of the minima of $\Delta f(z)$ curves, that is, maps of $z_{min}(x,y)$ and of $\Delta f_{min}(x,y)$, acquired over a molecule exhibit characteristic contrast. This contrast is reproduced in simulations based on molecular mechanics (MM) and DFT. We show that the vdW and Pauli interaction, together with the specific adsorption geometry of a given molecule on the surface, accounts for the observed contrast.

6.2 Methods

We synthesized a planar three-fold rotationally symmetric model molecule, 1,5,9-trioxo-13-azatriangulene (TOAT), see figure 6.1(a), that contains H, C, N, and O atoms. The planarity eliminates effects due to vertical corrugation.[24] This molecule was then investigated by STM and AFM techniques including 3D data acquisition. The experimental data was compared to theoretical models to find the robustness of the results and the origin of the contrast.

6.2.1 Synthesis of 1,5,9-trioxo-13-azatriangulene

The synthesis reported herein is based on literature procedures.[25] For the sake of completeness and reproducibility, we describe the procedure and our observations. The first step is the synthesis of tris(ortho-methylbenzoate)-amine (TOMBA). TOMBA was synthesized by refluxing a solution in diphenyl ether of 1:3:2 parts of 2-aminobenzoic acid methyl ester, 2-iodobenzoic acid methyl ester, and potassium carbonate, respectively, in the presence of copper and copper(I)iodide, for 16 h at 210 °C under nitrogen atmosphere. After purification, the yield was 76%. The purified TOMBA was subsequently used to synthesize 1,5,9-trioxo-13-azatriangulene (TOAT). A solution of TOMBA in 98% H_2SO_4 was heated to 105 °C and kept at that temperature for 24 h. After purification, the yield was 7.2% (46.9 mg).

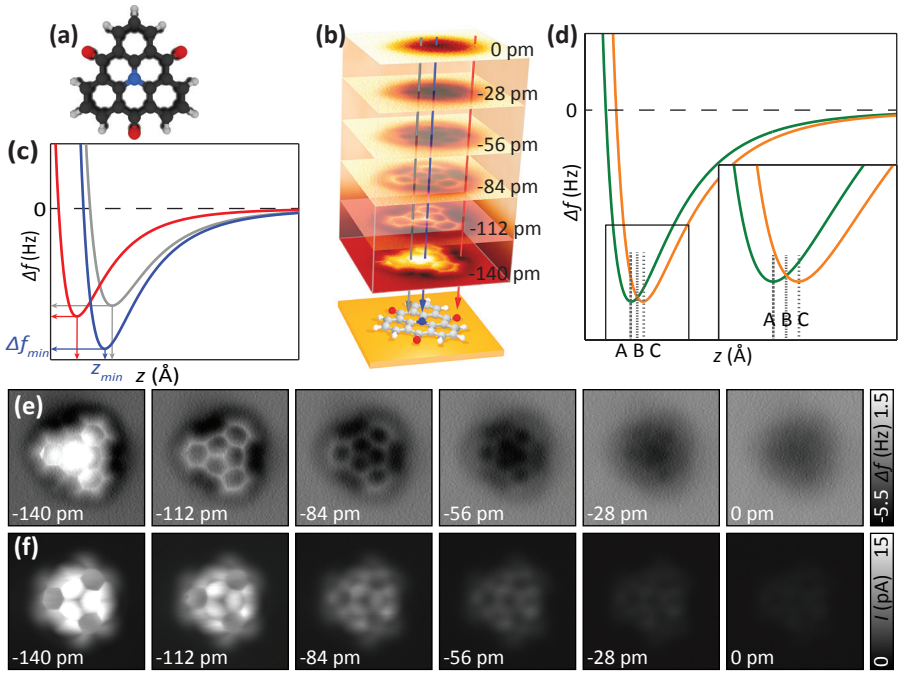

Figure 6.1 Acquisition and analysis of a 3D Δf data cube over a model molecule. **(a)** Model of 1,5,9-trioxo-13-azatriangulene (TOAT), which consists of carbon (black), nitrogen (blue), oxygen (red), and hydrogen (white) atoms. **(b)** $\Delta f(z)$ spectra can be extracted from the stack of constant height images **(c)** Model curves that could be extracted from a 3D data stack as shown in (b). (*i.e.*, the curves shown here do not represent experimental data). **(d)** Schematic curves with an offset in the vertical position of the minimum frequency shift, z_{min}, which may correspond to spectra acquired over different sites in a molecule. **(e)** Selection of constant height AFM images acquired with a CO-terminated tip. Indicated heights are with regard to an STM set point of 10 pA at 100 mV. **(f)** Simultaneously recorded current images.

6.2.2 STM and AFM measurements

We used an Omicron Nanotechnology LT STM/AFM with a commercially available qPlus sensor, operating at approximately 4.6 K in ultrahigh vacuum with an average pressure of 5×10^{-10} mbar. A Cu(111) crystal surface was cleaned with several sputter and anneal cycles before being inserted into the microscope head. The TOAT molecules were thermally evaporated onto the cold surface using a Focus GmbH e-beam evaporator. For STM imaging, the bias voltage was applied to the sample. The

baked qPlus sensor (3 h at 120 °C) had a quality factor of Q ≈ 30 000, a resonance frequency of f_0 = 25 634 Hz, and a peak-to-peak oscillation amplitude of <2 Å. After the tip approached the surface, it often needed some preparation to sharpen the apex and ensure stability. This was accomplished with controlled crashes into the copper surface and bias pulses until the STM resolution was satisfactory. The tip apex was functionalized with a single CO molecule following the standard method.[26] After an appropriate TOAT molecule was located on the surface, the tip was left in tunneling contact (I = 10 pA at V = 0.1 V) and allowed to relax for 12 h to prevent drift and creep. After this time, there was no detectable drift in x- and/or y-directions. To compensate for z-drift, the STM feedback was turned on for 2 s after each constant height AFM image and then turned off again before adjusting the height for the next image. No data analysis procedures such as those described by Albers *et al.*[27] were therefore necessary. The AFM was operated in constant height mode, and AFM images show the frequency shift (Δf) with respect to the resonance frequency.

6.2.3 Theoretical modeling

Simulations were performed using MM calculations using geometries and charge distributions as determined from DFT calculations.

DFT calculations were performed using local basis sets with the FHIaims code to determine the adsorption geometry of TOAT on a Cu(111) surface.[28] Both slab and cluster calculations were carried out. First, a 8×8 supercell was used made of three Cu layers to describe the Cu(111) surface. Second, a cluster calculation was adopted, where the metallic cluster consists of 25 Cu atoms arranged in the Cu(111) surface orientation.

In both cases the molecule was placed on the surface with the N atom located directly above a Cu atom as found experimentally (see below). All the atoms except the bottom two Cu layers were relaxed until the remaining atomic forces and the total energy were below 10^{-2} eV/Å and 10^{-5} eV, respectively. All the calculations were carried out at the GGA-PBE level including the Tkachenko-Scheffler treatment of the vdW interactions.[29,30] The use of vdW interactions is necessary to accurately describe

the molecule-substrate interaction. The scaled zeroth-order regular approximation was applied to take into account relativistic effects.

Both the slab and cluster calculations reveal only a weak coupling of TOAT to the Cu(111) substrate. Indeed, our total energy DFT calculations do not predict any formation of strong chemical bonds between the molecule and the substrate. The molecule adopts an almost planar configuration with the plane of the molecule approximately 2.7 Å and 2.8 Å above the Cu(111) surface for the slab and cluster, respectively. The peripheral O atoms are bent down slightly (by z = -0.15 Å), whereas the central N atom is subtly protruded outward of the molecular plane with respect to the nearest neighbor C atoms, by approximately 0.05 Å. The main difference between the slab and cluster calculations consists of weakly inclined configuration obtain for the slab calculation. One of the peripheral oxygen atoms is shifted down ~0.02 Å more than the others. We attribute this effect to a spurious electrostatic interaction between adjacent unit cells as this tilting is absent in the cluster calculations.

To simulate the high-resolution AFM images, we used the same molecular mechanics probe particle AFM model as described in chapter 3 and 4, in which the CO molecule at the tip is considered as a spherical particle. The probe particle interacts with the substrate via pair-wise Lennard-Jones potentials. In addition, electrostatic forces, based on a convolution of the surface Hartree potential, extracted from the DFT calculations, with an electron density localized on the tip represented by a Gaussian, are taken into account.[31,32] The maps were simulated for different effective tip charge (Q) and lateral stiffness (k) to determine the optimal parameters as described in chapter 4. The frequency shift was computed from simulated $F(z)$-curves using Giessbl's formula using the experimental values of the oscillation amplitude (2.0 Å) and sensor stiffness (k = 1800 N/m).[33]

6.3 Results and discussion

The 3D Δf maps were acquired with CO-terminated tips by measuring stacks of 100 constant height AFM images with an interval of 7 pm over TOAT adsorbed on Cu(111), as visualized by figure 6.1(b). The image at the smallest tip-sample distance was taken

at Δz = -140 pm with respect to an STM set point of I = 10 pA at V = 0.1 V. A selection from the experimental AFM images is shown in figure 6.1(c). In addition, figure 6.1(d) shows the corresponding simultaneously recorded current images. The geometric structure of the molecule is clearly resolved. We extracted experimental $\Delta f(z)$ spectra over the molecule from the 3D data cube, as schematically illustrated in figure 6.1(b) and (e), from which we determined the $z_{min}(x,y)$ and $\Delta f_{min}(x,y)$ maps.

Before discussing these maps, we briefly discuss the advantage of acquiring and analyzing a 3D data grid over regular constant height images. The contrast in constant height AFM images sensitively depends on the height. However, also the difference in the contrast between sites can change as a function of tip-sample distance. For example, consider the two schematic $\Delta f(z)$ curves shown in figure 6.1(f). These could correspond to curves acquired over different sites in the molecule. Constant height images taken at tip-sample distances A and C will show an inverted contrast. Furthermore, if an image is taken at tip-sample distance B, the contrast at the two positions where the curves were acquired is identical. Since $\Delta f(z)$ curves and their spatial variation are not a priori known, it is impossible to know at which tip-sample distance to take an image. In contrast, $z_{min}(x,y)$ and $\Delta f_{min}(x,y)$ maps provide robust information.

The experimental work is complemented by a theoretical analysis. First, the adsorption geometry and charge distribution of TOAT on Cu(111) were calculated using total energy DFT simulations including vdW interactions. The relaxed geometry of the molecule on the surface is shown in figure 6.2. The DFT results (charge distribution, adsorption geometry) were used as input for the MM-based simulation of the full 3D AFM data.[8,31,32,34] The mechanistic model includes the vdW and Pauli forces, as well as the electrostatic interactions between the tip and sample. The two main parameters in the mechanistic model are the lateral stiffness (k) of the probe particle-bulk tip-junction and the effective charge (Q) of the probe particle. The parameters that provide the best agreement with experimental data were determined by comparing a stack of images simulated with different values of k and Q with experimental AFM images acquired at different heights above the molecule. The as-determined values

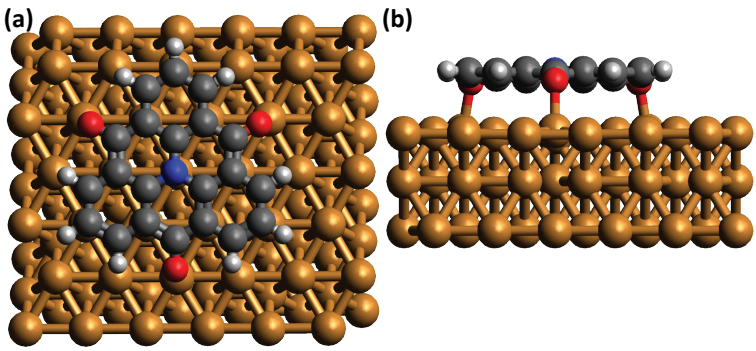

Figure 6.2 Fully relaxed atomic structure of TOAT on Cu(111) obtained from periodic DFT calculations including van der Waals interactions. **(a)** Top view. **(b)** Side view.

are k = 0.24 N/m and Q = 0.0 e. These values are in fair agreement with previously reported values.[7,35,36] We note here that the effective charge of the CO will depend on how the molecule is adsorbed on the tip as well as on the chemical composition of the metallic tip apex to which it is bound. In addition, we added a long-range $\Delta f(z)$ component, estimated from experimental $\Delta f(z)$ spectra taken on the bare Cu(111) surface, to enable a direct comparison between the experimental and theoretical data.

The minima of the experimental and simulated $\Delta f(z)$ curves were found by fitting a parabola to points up to 1 Hz above the most negative Δf value. Over the lower lying Cu(111) substrate, the $\Delta f(z)$ spectra did not reach the minimum, which could therefore not be assigned. Contour plots of the as-determined values of experimental and simulated $z_{min}(x,y)$ and $\Delta f_{min}(x,y)$ maps are plotted in figure 6.3. Using the coordinates of the minimum of the curve to compare experimental data to simulated images enables us to review detailed information and small deviations visually. Extracting the location of the minimum from a $\Delta f(z)$ curve yields information about the effect and interplay of both repulsive and attractive forces. Alternatively, one can extract Lennard-Jones fit parameters from $\Delta f(z)$ spectra, but these are more prone to errors due to tip flexibility, especially at close distance. At distances where $z_{min}(x,y)$ and $\Delta f_{min}(x,y)$ are located, the lateral relaxation of the probe is still negligible.

The experimental and simulated $z_{min}(x,y)$ and $\Delta f_{min}(x,y)$ maps, shown in figure 6.3,

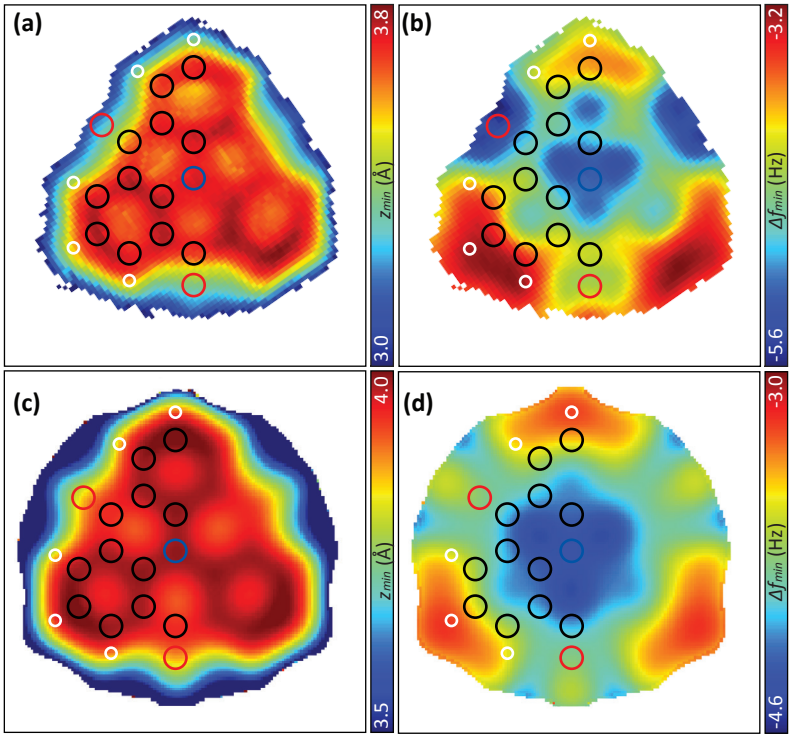

Figure 6.3 (a) Experimental $z_{min}(x,y)$ and **(b)** $\Delta f_{min}(x,y)$ maps, obtained with a CO-terminated tip. **(c)** Calculated $z_{min}(x,y)$ and **(d)** $\Delta f_{min}(x,y)$ maps. Theoretical $\Delta f_{min}(x,y)$ and $z_{min}(x,y)$ maps are calculated using a lateral stiffness k = 0.24 N/m and an effective charge on the CO tip of Q = 0.0 e.

are overall in good agreement. Above bonds/atoms, $z_{min}(x,y)$ is located at larger values of z compared to other positions (values of z refer to the height above the molecular plane). This is expected because, at these positions repulsive interactions become more important at smaller tip-sample distances. Hence, the $z_{min}(x,y)$ maps resemble the structure of the molecule, including the vertical corrugation within the molecule. The $\Delta f_{min}(x,y)$ maps feature more contrast. Above the benzene rings at the periphery, the minimum of the frequency shift is less negative (red) compared to the center of the molecule (blue). This is ascribed to the smaller vdW attraction at the edges. Note that the experimental maps do not extend as far outward from the center of the molecule as the simulated maps. Using an alternative approach, it should be possible to create

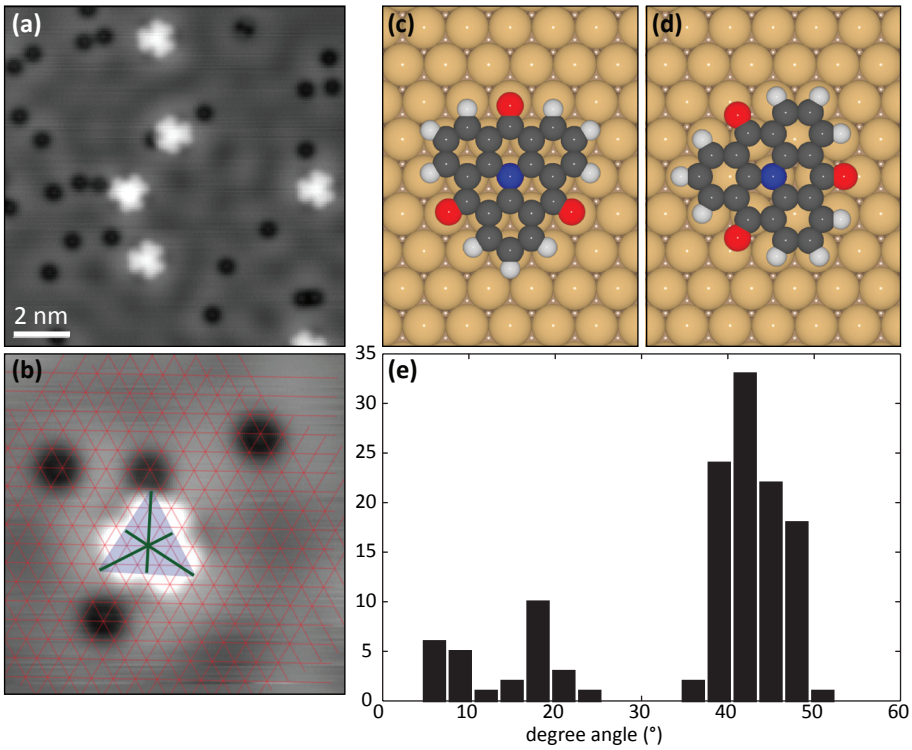

Figure 6.4 Study of adsorption orientation of TOAT on Cu(111). **(a)** STM image of six TOAT molecules and several CO molecules on Cu(111), acquired with a CO-terminated tip. **(b)** STM image of an adsorbed TOAT molecule and surrounding CO molecules, acquired with a CO-terminated tip. The dimensions of the overlaid grid correspond to the atomic configuration of the Cu(111) surface. **(c-d)** Schematic representation of a TOAT molecule adsorbed on Cu(111) between rows and along row orientations, respectively. **(e)** Histogram of relative angles of adsorbed TOAT molecules.

$z_{min}(x,y)$ and $\Delta f_{min}(x,y)$ maps of the entire imaging area.[37] Our total energy calculations indicate a very shallow potential energy with respect to the vertical distortion of the oxygen atoms. The resulting uncertainty in the vertical position of the oxygen atoms will affect the contrast at these positions.

The contrast in the experimental $\Delta f_{min}(x,y)$ map has an imperfect three-fold symmetry. There can be multiple reasons for this. To investigate if this imperfect symmetry in the maps is due to a reduction of the symmetry induced by adsorption on the surface, we

determined the adsorption configurations. We find that TOAT adsorbs on Cu(111) with two different orientations, rotated by 30°; see figure 6.4. The adsorption configuration of both species was determined by using co-evaporated CO molecules as markers since CO molecules are known to be adsorbed on top of Cu atoms.[38] An example is shown in figure 6.4(b). An analysis of multiple molecules consistently shows that in both configurations the N atom is adsorbed on top of a Cu atom. The two configurations correspond to molecules with their O atoms pointing between and along rows of Cu atoms, figure 6.4(c) and (d) respectively. Both of these adsorption geometries are threefold symmetric. The imperfect symmetry in the experimental $\Delta f_{min}(x,y)$ map is therefore attributed to tip flexibility in conjunction with an asymmetric tip on the mesoscopic scale.[19,31,39] This is further supported by the fact that maps acquired with a different CO-terminated tip on a different molecule exhibit a different symmetry.

To further investigate if the observed contrast in the $\Delta f_{min}(x,y)$ and $z_{min}(x,y)$ maps are molecule-specific, we take advantage of the good agreement of the simulated and experimental data. We calculated $\Delta f_{min}(x,y)$ and $z_{min}(x,y)$ maps with a CO tip for molecules with a different chemical composition but a similar structure. Specifically, we replaced the ketone groups by an ether (TOAT-ether) or a secondary amine (TOAT-amine), or we replaced the central N with a C (TOAT-C); see figure 6.5(a–c). In the latter case, one of the O atoms is changed into a hydroxyl group (OH) to maintain charge neutrality. Note that these molecules all have the same skeleton of conjugated carbon rings. However, each molecule has a distinct contrast in the $\Delta f_{min}(x,y)$ and $z_{min}(x,y)$ maps, and they are different from the maps of TOAT shown in figure 6.3. Our DFT calculations revealed that these differences originate from different vdW interactions, as well as from changes in the atomic relaxation of the molecules on the surface. This is in agreement with the observation of Schuler *et al.* that polycyclic aromatic hydrocarbons that have a different functional group have a different adsorption height.[40]

The $\Delta f_{min}(x,y)$ maps also exhibit clear differences, especially at the periphery, where the different functional groups are located. In particular, there is a shift in location and depth of the well, indicated by green arrows in figure 6.5(g–i). The calculated $\Delta f_{min}(x,y)$ of TOAT-C, figure 6.4(f), contains an asymmetry caused by the OH group on

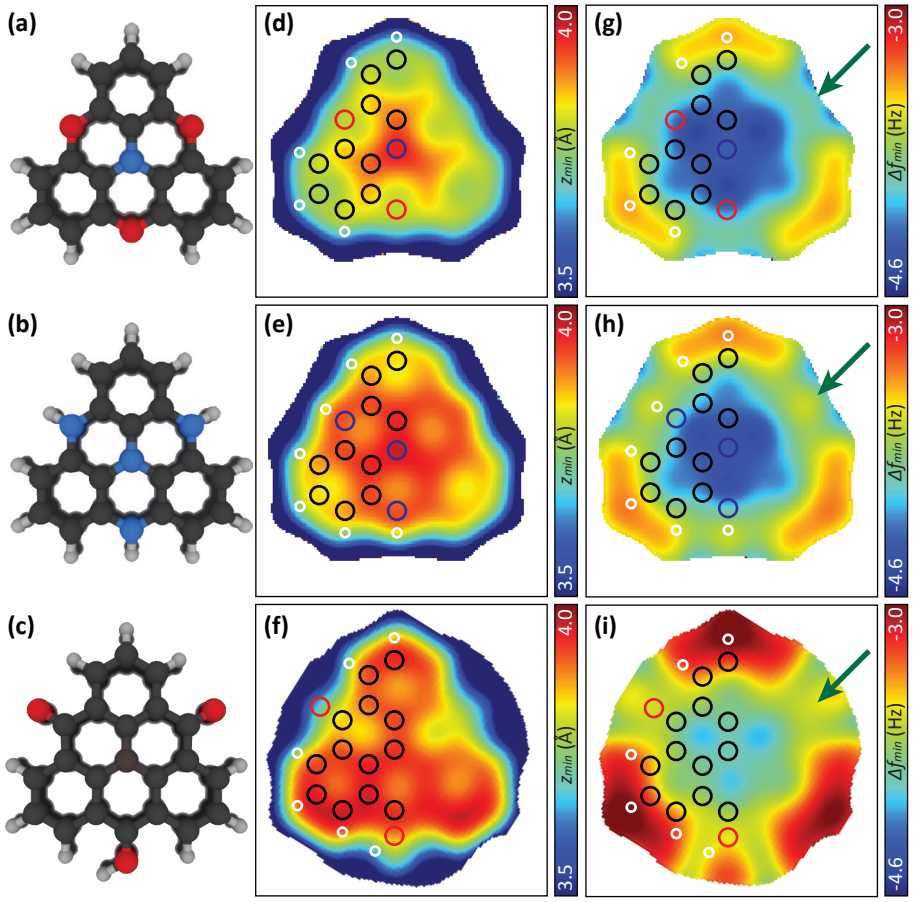

Figure 6.5 Schematic representations of theoretically investigated molecules, where ketone groups in TOAT are replaced by **(a)** an ether (TOAT-ether), **(b)** a secondary amine (TOAT-amine), **(c)** the central N with a C (TOAT-C). Calculated $z_{min}(x,y)$ maps for **(d)** TOAT-ether, **(e)** TOAT-amine, **(f)** TOAT-C. Calculated $\Delta f_{min}(x,y)$ maps for **(g)** TOAT-ether, **(h)** TOAT-amine, **(i)** TOAT-C. Theoretical $\Delta f_{min}(x,y)$ and $z_{min}(x,y)$ are calculated with a lateral stiffness of k = 0.24 N/m and an effective charge on the CO tip of Q = 0.0e.

the periphery. From this comparison, it is evident that $\Delta f_{min}(x,y)$ and $z_{min}(x,y)$ maps can be used to discriminate between molecules.

We now turn our attention to the origin of the characteristic contrast. Since the simulations without including electrostatic forces (the effective charge Q on the tip

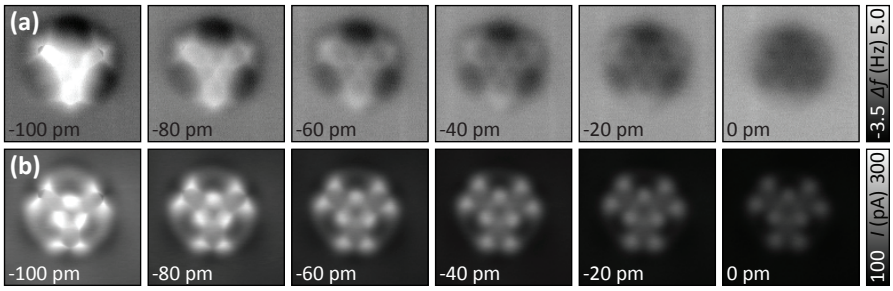

Figure 6.6 Selection of images from 3D mapping, recorded with a Xe-terminated tip. **(a)** Selection of constant height AFM images. **(b)** Simultaneously recorded *I* images. Indicated heights are with regard to STM set point of 500 pA at 200 mV.

is zero) can reproduce the experimental observations very well, electrostatic forces cannot be responsible for the characteristic contrast. Hence, the vdW and Pauli interaction, together with the specific adsorption geometry of a given molecule on the surface, must therefore account for the contrast. At the distance of most negative frequency shift, that is, at z_{min}, the vdW component is dominant.

Considering the above, the contrast in the $z_{min}(x,y)$ and $\Delta f_{min}(x,y)$ maps may be blurred for probes with a large atomic radius (*e.g.*, Xe) and/or a significant charge. A larger probe radius leads to increased interactions with neighboring atoms, resulting in an averaging effect. Charged tips may not be suitable since the charge distribution in molecules typically varies rather slowly, and regions of increased charge density are not necessarily localized on atoms. We note here that the large majority of the molecules have a nonhomogeneous charge distribution.

To support this interpretation of the contrast mechanism, we repeated the experiment and simulations with a positively charged Xe-terminated tip (parameters: Q = +0.3 e and k = 0.24 N/m).[8] A selection from the constant height AFM images and the corresponding *I* images is shown in figure 6.6.

Figure 6.7 shows the experimental and theoretical $z_{min}(x,y)$ and $\Delta f_{min}(x,y)$ maps extracted from the 3D data. The simulated and experimental maps show, just like for the CO tip, very good agreement. However, in contrast to the maps acquired with CO tips, both $\Delta f_{min}(x,y)$ and $z_{min}(x,y)$ maps acquired with Xe-terminated tips show very little features. Our theoretical analysis shows that the loss of resolution is driven by both

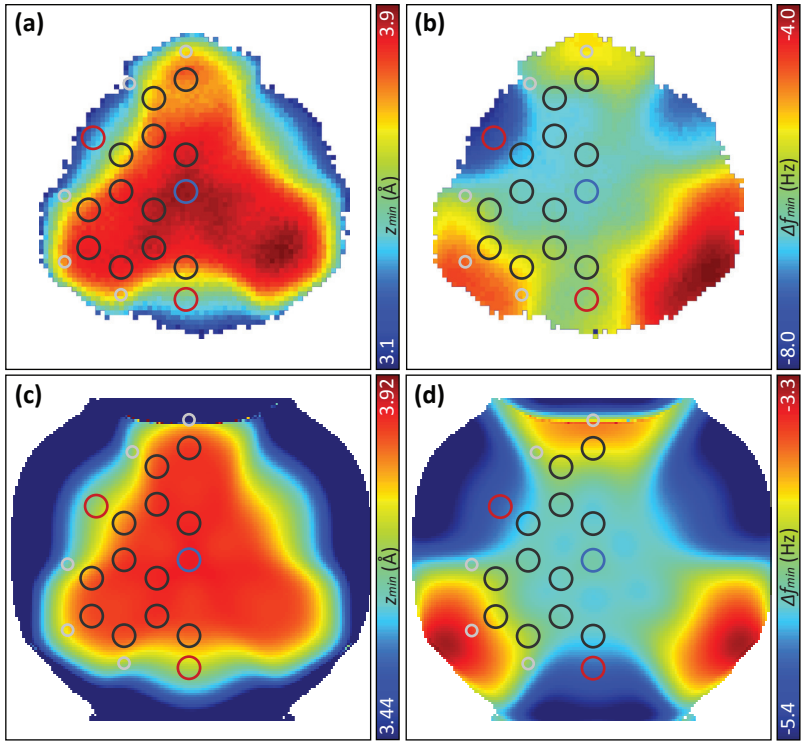

Figure 6.7 (a) Experimental $z_{min}(x,y)$ and **(b)** $\Delta f_{min}(x,y)$ maps, obtained with a Xe-terminated tip. **(c)** Calculated $z_{min}(x,y)$ and **(d)** $\Delta f_{min}(x,y)$ maps. Theoretical $\Delta f_{min}(x,y)$ and $z_{min}(x,y)$ are calculated with a lateral stiffness of k = 0.24 N/m and an effective charge on the Xe tip of Q = +0.3e.

the large atomic radius of Xe and the pronounced electrostatic interaction between the charged probe and the molecule. Because of these two reasons, Xe-terminated tips are less suitable for chemical recognition of molecules.

The C and N atoms in the center of the molecule have a similar chemical and geometric environment. In addition, the gradient of the underlying vdW background is small in the interior of the molecule. Furthermore, their central location is important to minimize the influence of tip relaxations (*i.e.*, bending of the CO).[24] Hence, for this molecule, $\Delta f(z)$ spectra acquired above C and N in the center can be compared on (almost) equal footing. Figure 6.8(a) shows $\Delta f(z)$ spectra extracted from the same 3D

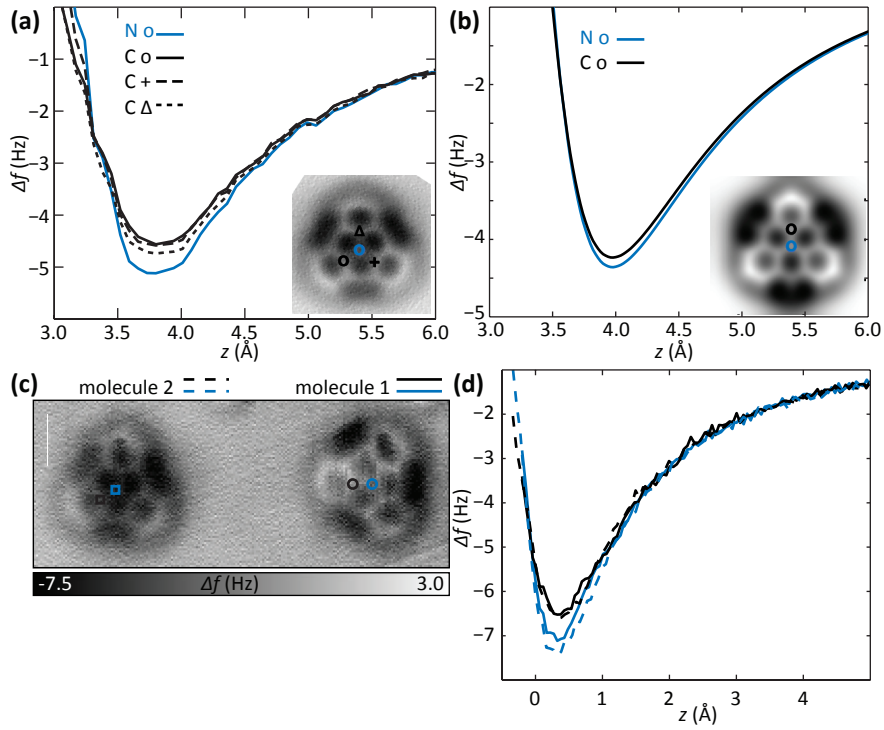

Figure 6.8 Additional $\Delta f(z)$ spectra over TOAT molecules a CO-terminated tip. **(a)** $\Delta f(z)$ spectra extracted from the 3D data grid over positions on TOAT, indicated in the inset. The $\Delta f(z)$ spectra are the average of nine curves of a 3×3 pixel area. **(b)** Simulated $\Delta f(z)$ spectra extracted over positions on TOAT, indicated in the inset. **(c)** Constant height AFM image of two molecules in different orientation, at −130 pm w.r.t. STM set point 10 pA at 100 mV. Molecule **1** and molecule **2** lie with their peripheral O atoms between and along atomic rows, respectively. **(d)** Individual $\Delta f(z)$ spectra acquired above the two molecules in (c), where z = 0 Å corresponds to the imaging height of (c). The z values of molecule **1** are corrected for z-drift as follows: immediately prior to the AFM experiment, an $I(z)$ curve was acquired (with the same oscillation amplitude and bias), which was used to convert the observed changes in the tunnel current during the constant height experiment to a change in tip-sample distance. The z-drift between acquisition of the two $\Delta f(z)$ spectra was 0.35 Å.

data set as was used to compile the $\Delta f_{min}(x,y)$ and $z_{min}(x,y)$ maps in figure 6.3. The (x,y) positions approximately correspond to the location of a N (blue) and three equivalent C (black) atoms, respectively (see inset). The coordinates of the minimum are distinctly different for the different atoms: the well above the central N atom (blue curve) is

deeper than that above a C atom (black curve). The value of z_{min} for both atoms is the same within experimental error, indicating that they have the same adsorption height to within a few picometers. This is in good agreement with the DFT calculations. The differences between the chemically and geometrically equivalent C atoms are much smaller than the difference between C and N. The calculated $\Delta f(z)$ spectra over these atoms are shown in figure 6.8(b) and reproduce the experimentally observed trend.

To examine the influence of the adsorption site on the $\Delta f(z)$ curves, spectra were simultaneously acquired above molecules in both configurations. Figure 6.8(c) shows a constant height AFM image of two molecules with different adsorption configuration. As shown in figure 6.8(d), spectra acquired over equivalent positions over the two molecules overlap within experimental error. Note that the trend is the same as observed in the spectra extracted from the 3D data cube: Δf_{min} is significantly more negative for N than for the neighboring C atoms. This trend should hold for all tertiary amines (N atom coordinated to three C atoms) and C atoms that have a similar geometric and chemical environment (including adsorption height and interaction with the surface). The absolute values differ between experiments due to different macroscopic atomic tip clusters, resulting in different vdW contributions.

6.4 Conclusion

In summary, we showed that maps of $z_{min}(x,y)$ and $\Delta f_{min}(x,y)$ acquired with CO-terminated tips have distinct characteristics that can differentiate between structurally similar molecules on surfaces. The characteristic contrast in these maps originates from the vdW interactions between tip and molecule, as well as from the adsorption geometry of the molecule on the surface. Since the adsorption height, and its variations within a molecule, strongly depend on the interaction between the molecule and the substrate, the $z_{min}(x,y)$ and $\Delta f_{min}(x,y)$ maps of a particular molecule should be substrate-dependent. The trends in z-position and the depth of the minimum are the same for all CO-terminated tips, while the absolute values differ from tip to tip. Tips employing larger atoms and/or tips with a significant charge (like Xe) are less suitable for chemical recognition of molecules.

The force resolution required to apply the procedure outlined here is on the order

of 1 pN/100 mHz(for a typical qPlus sensor). This criterion is typically fulfilled in cases where sub-molecular resolution imaging of molecules has been reported.

6.5 References

[1] J. Repp, G. Meyer, S. M. Stojković, A. Gourdon, C. Joachim, Molecules on Insulating Films: Scanning-Tunneling Microscopy Imaging of Individual Molecular Orbitals. *Phys. Rev. Lett.* **94**, 26803 (2005).

[2] L. Gross, F. Mohn, N. Moll, P. Liljeroth, G. Meyer, The Chemical Structure of a Molecule Resolved by Atomic Force Microscopy. *Science.* **325**, 1110–1114 (2009).

[3] C. Weiss, C. Wagner, R. Temirov, F. S. Tautz, Direct Imaging of Intermolecular Bonds in Scanning Tunneling Microscopy. *J. Am. Chem. Soc.* **132**, 11864–11865 (2010).

[4] C. -l. Chiang, C. Xu, Z. Han, W. Ho, Real-space imaging of molecular structure and chemical bonding by single-molecule inelastic tunneling probe. *Science.* **344**, 885–888 (2014).

[5] F. Mohn, L. Gross, N. Moll, G. Meyer, Imaging the charge distribution within a single molecule. *Nat. Nanotechnol.* **7**, 227–231 (2012).

[6] L. Gross, N. Moll, F. Mohn, A. Curioni, G. Meyer, F. Hanke, M. Persson, High-Resolution Molecular Orbital Imaging Using a p-Wave STM Tip. *Phys. Rev. Lett.* **107**, 86101 (2011).

[7] L. Gross, F. Mohn, N. Moll, B. Schuler, A. Criado, E. Guitian, D. Pena, A. Gourdon, G. Meyer, Bond-Order Discrimination by Atomic Force Microscopy. *Science.* **337**, 1326–1329 (2012).

[8] P. Hapala, M. Švec, O. Stetsovych, N. J. van der Heijden, M. Ondráček, J. van der Lit, P. Mutombo, I. Swart, P. Jelínek, Mapping the electrostatic force field of single molecules from high-resolution scanning probe images. *Nat. Commun.* **7**, 11560 (2016).

[9] B. C. Stipe, Single-Molecule Vibrational Spectroscopy and Microscopy. *Science.* **280**, 1732–1735 (1998).

[10] M. Schmid, H. Stadler, P. Varga, Direct observation of surface chemical order by scanning tunneling microscopy. *Phys. Rev. Lett.* **70**, 1441–1444 (1993).

[11] P. Varga, M. Schmid, Chemical discrimination on atomic level by STM. *Appl. Surf. Sci.* **141**, 287–293 (1999).

[12] J. Jiang, M. Kula, Y. Luo, Molecular modeling of inelastic electron transport in molecular junctions. *J. Phys. Condens. Matter.* **20**, 374110 (2008).

[13] M. a Lantz, Quantitative Measurement of Short-Range Chemical Bonding Forces. *Science.* **291**, 2580–2583 (2001).

[14] Y. Sugimoto, P. Pou, M. Abe, P. Jelinek, R. Pérez, S. Morita, O. Custance, Chemical identification of individual surface atoms by atomic force microscopy. *Nature.* **446**, 64–67 (2007).

[15] M. Setvín, P. Mutombo, M. Ondráček, Z. Majzik, M. Švec, V. Cháb, I. Ošťádal, P. Sobotík, P. Jelínek, Chemical Identification of Single Atoms in Heterogeneous III–IV Chains on Si(100) Surface by Means of nc-AFM and DFT Calculations. *ACS Nano.* **6**, 6969–6976 (2012).

[16] G. Teobaldi, K. Lämmle, T. Trevethan, M. Watkins, A. Schwarz, R. Wiesendanger, a. L. Shluger, Chemical resolution at ionic crystal surfaces using dynamic atomic force microscopy with metallic tips. *Phys. Rev. Lett.* **106**, 216102 (2011).

[17] J. Welker, A. J. Weymouth, F. J. Giessibl, The Influence of Chemical Bonding Configuration on Atomic Identification by Force Spectroscopy. *ACS Nano.* **7**, 7377–7382 (2013).

[18] M. Z. Baykara, M. Todorović, H. Mönig, T. C. Schwendemann, Ö. Ünverdi, L. Rodrigo, E. I. Altman, R. Pérez, U. D. Schwarz, Atom-specific forces and defect identification on surface-

oxidized Cu(100) with combined 3D-AFM and STM measurements. *Phys. Rev. B.* **87**, 155414 (2013).
[19] H. Hölscher, S. M. Langkat, A. Schwarz, R. Wiesendanger, Measurement of three-dimensional force fields with atomic resolution using dynamic force spectroscopy. *Appl. Phys. Lett.* **81**, 4428 (2002).
[20] L. Gross, F. Mohn, N. Moll, G. Meyer, R. Ebel, W. M. Abdel-Mageed, M. Jaspars, Organic structure determination using atomic-resolution scanning probe microscopy. *Nat. Chem.* **2**, 821–825 (2010).
[21] B. Schuler, G. Meyer, D. Peña, O. C. Mullins, L. Gross, Unraveling the Molecular Structures of Asphaltenes by Atomic Force Microscopy. *J. Am. Chem. Soc.* **137**, 9870–9876 (2015).
[22] S. Kawai, S. Saito, S. Osumi, S. Yamaguchi, A. S. Foster, P. Spijker, E. Meyer, Atomically controlled substitutional boron-doping of graphene nanoribbons. *Nat. Commun.* **6**, 8098 (2015).
[23] N. Moll, L. Gross, F. Mohn, A. Curioni, G. Meyer, The mechanisms underlying the enhanced resolution of atomic force microscopy with functionalized tips. *New J. Phys.* **12**, 125020 (2010).
[24] M. P. Boneschanscher, S. K. Hämäläinen, P. Liljeroth, I. Swart, Sample Corrugation Affects the Apparent Bond Lengths in Atomic Force Microscopy. *ACS Nano.* **8**, 3006–3014 (2014).
[25] D. Hellwinkel, M. Melan, Heteropolycyclen vom Triangulen-Typ, I. 8.12-Dihydro-4H-benzo[1.9]chinolizino[3.4.5.6.7-defg]acridin-trion-(4.8.12) und 5.9-Dihydro-chino[3.2.1-de]acridin-dion-(5.9). *Chem. Ber.* **104**, 1001–1016 (1971).
[26] L. Bartels, G. Meyer, K.-H. Rieder, Controlled vertical manipulation of single CO molecules with the scanning tunneling microscope: A route to chemical contrast. *Appl. Phys. Lett.* **71**, 213 (1997).
[27] B. J. Albers, T. C. Schwendemann, M. Z. Baykara, N. Pilet, M. Liebmann, E. I. Altman, U. D. Schwarz, Data acquisition and analysis procedures for high-resolution atomic force microscopy in three dimensions. *Nanotechnology.* **20**, 264002 (2009).
[28] V. Blum, R. Gehrke, F. Hanke, P. Havu, V. Havu, X. Ren, K. Reuter, M. Scheffler, Ab initio molecular simulations with numeric atom-centered orbitals. Comput. *Phys. Commun.* **180**, 2175–2196 (2009).
[29] A. Tkatchenko, M. Scheffler, Accurate Molecular Van Der Waals Interactions from Ground-State Electron Density and Free-Atom Reference Data. *Phys. Rev. Lett.* **102**, 73005 (2009).
[30] S. Grimme, Semiempirical GGA-type density functional constructed with a long-range dispersion correction. *J. Comput. Chem.* **27**, 1787–1799 (2006).
[31] P. Hapala, G. Kichin, C. Wagner, F. S. Tautz, R. Temirov, P. Jelínek, Mechanism of high-resolution STM/AFM imaging with functionalized tips. *Phys. Rev. B.* **90**, 85421 (2014).
[32] P. Hapala, R. Temirov, F. S. Tautz, P. Jelínek, Origin of High-Resolution IETS-STM Images of Organic Molecules with Functionalized Tips. *Phys. Rev. Lett.* **113**, 226101 (2014).
[33] F. J. Giessibl, A direct method to calculate tip–sample forces from frequency shifts in frequency-modulation atomic force microscopy. *Appl. Phys. Lett.* **78**, 123 (2001).
[34] S. K. Hämäläinen, N. van der Heijden, J. van der Lit, S. den Hartog, P. Liljeroth, I. Swart, Intermolecular Contrast in Atomic Force Microscopy Images without Intermolecular Bonds. *Phys. Rev. Lett.* **113**, 186102 (2014).
[35] A. J. Weymouth, T. Hofmann, F. J. Giessibl, Quantifying Molecular Stiffness and Interaction with Lateral Force Microscopy. *Science.* **343**, 1120–1122 (2014).
[36] J. van der Lit, F. Di Cicco, P. Hapala, P. Jelinek, I. Swart, Submolecular Resolution Imaging of

Molecules by Atomic Force Microscopy: The Influence of the Electrostatic Force. *Phys. Rev. Lett.* **116**, 96102 (2016).

[37] F. Mohn, L. Gross, G. Meyer, Measuring the short-range force field above a single molecule with atomic resolution. *Appl. Phys. Lett.* **99**, 53106 (2011).

[38] S. Ishi, Y. Ohno, B. Viswanathan, An overview on the electronic and vibrational properties of adsorbed CO. *Surf. Sci.* **161**, 349–372 (1985).

[39] D. Z. Gao, J. Grenz, M. B. Watkins, F. Federici Canova, A. Schwarz, R. Wiesendanger, A. L. Shluger, Using Metallic Noncontact Atomic Force Microscope Tips for Imaging Insulators and Polar Molecules: Tip Characterization and Imaging Mechanisms. *ACS Nano.* **8**, 5339–5351 (2014).

[40] B. Schuler, W. Liu, A. Tkatchenko, N. Moll, G. Meyer, A. Mistry, D. Fox, L. Gross, Adsorption Geometry Determination of Single Molecules by Atomic Force Microscopy. *Phys. Rev. Lett.* **111**, 106103 (2013).

7

Adsorption geometry of single molecules on Cu(111) resolved with sub-molecular resolution using atomic force microscopy

abstract

How molecules adsorb on surfaces can strongly influence their electronic and geometric structure, affecting for example the density of states, π-conjugation and charge distribution. However, establishing experimentally how the geometry of a molecule changes upon adsorption represents a significant challenge, especially in the case of low molecular coverage and/or for molecules in disordered phases.

Here, we show how high-resolution AFM can be used to investigate relaxations within a molecule upon adsorption on a surface with pico-meter accuracy. Specifically, we investigated two molecular isomers, one of which exhibits a strong interaction with a Cu(111) surface whereas the other isomer is bound only via van der Waals forces. By correlating the experimental results to density functional theory calculations, we show that changes in the molecular geometry can be extracted from 3D force maps.

based on

Nadine J. van der Heijden, B. Klein, M. Gottfried, and I Swart, *in preparation* (2017)

7.1 Introduction

The adsorption geometry of molecules on metal surfaces is essential for the investigation and understanding of catalytic processes.[1,2] When a molecule adsorbs onto a surface its electronic and geometric structure can be strongly altered, depending on how strong the interaction with the substrate is. For example, the dipole moment and/or charge state of a species will be affected by charge transfer within the molecule or to/from the surface. In addition, the geometric structure of the molecule might change with respect to its structure in the gas phase. Some areas in a molecule might interact more strongly with the surface than others, resulting in changes in bond lengths and bond angles within the molecule. Such effects can affect the chemical reactivity of the molecule.

Changes in adsorption heights upon self-assembly of molecules have been studied by low energy electron diffraction (LEED).[3,4] For the investigation and better understanding of chemical reactions it is essential to be able to study how individual molecules change upon adsorption. With atomic force microscopy (AFM) one can image single molecules with sub-molecular resolution.[2,5–8] From these images bond orders can be extracted.[9] Furthermore, AFM can be used to investigate the charge distribution and dipole moment of individual molecules.[10]

It is well established that sub-molecular resolution AFM images of molecules suffer from image distortions, see chapters 3 and 4. Thus far, the interest was on in-plane distortions.[8,11] At present, the AFM community is beginning to explore how the technique can be used to extract quantitative information also from non-planar systems. It has been shown that the vertical corrugation of the sample will affect the apparent bond lengths, and therefore bond orders.[12] Schuler *et al.* showed that adsorption angles and heights can be determined from zmin maps.[13] The tip-height at minimal Δf has been used to study the displacement of a Cu atom in a copper-metalated tetraphenylporphyrin molecule upon conformational switching.[14] These latter findings suggest that $z_{min}(x,y)$ maps can be used to determine vertical displacements within single molecules upon adsorption on a surface.

In order to establish the changes upon adsorption, it is beneficial to compare two similar molecules: one which is expected to be unperturbed by adsorption and one

where adsorption results in distortions. Here, we study the adsorption of azulene and naphthalene on Cu(111). The structures of these molecules are shown in figure 7.1. Both molecules contain 10 carbon and 8 hydrogen atoms, either arranged in 2 six membered rings (napthalene), or in a 5- and 7-membered ring (azulene). The van der Waals (vdW) interaction with the surface is therefore similar for both molecules. In contrast, the electronic structure of the two molecules is very different. Naphthalene is a symmetric molecule, does not have a dipole moment and its frontier molecular orbitals are far away from the Fermi-level of the substrate. Azulene has a dipole moment of 1.08 D and the lowest unoccupied molecular orbital has an energy close to the Fermi level of Cu(111).[15,16] As a result, azulene chemisorbs whereas naphthalene physisorbs on Cu(111).

In this chapter 3D force maps as a function of tip-sample distance z and gap voltage V were obtained over azulene and naphthalene. From these, characteristic z_{min} and kelvin probe force microscopy (KPFM) maps were constructed. The experimental z_{min} map exhibits variations that match the distortions in the molecule as calculated with density functional theory (DFT). The KPFM map indicates that despite the strong interaction with the surface, azulene retains a dipole moment upon adsorption on Cu(111).

7.2 Methods

7.2.1 STM and AFM measurements

For AFM and STM measurements a combined AFM/STM (Omicron GmbH) was used, operating at 4.6 K. The z_{min} and KPFM maps were obtained by analysis of subsequent constant height frequency shift maps with increasing height or gap voltage respectively.[17,18] The qPlus sensor was operated with a Q-factor ≈ 30,000 and at a resonance frequency of f_0 = 21 922 Hz, with an amplitude of A < 1 Å. The tip was functionalized with a CO molecule for the azulene experiments,[19] and with an unconfirmed species, possibly an azulene molecule, for the naphthalene experiments.

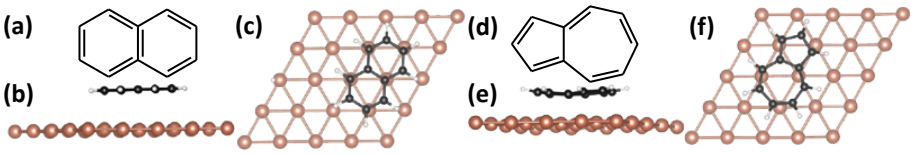

Figure 7.1 (a) Schematic of a naphthalene molecule. **(b-c)** Side- and top-view of naphthalane relaxed adsorption geometry as calculated by DFT. Only one of the four layers of Cu atoms is shown. **(d)** Schematic of an azulene molecule. **(e-f)** Relaxed adsorption geometry side- and top-view of azulene as calculated by DFT. Only one of the four layers of Cu atoms is shown.

7.2.2 Density functional theory

For the DFT calculations the VASP 5.4.1 package was used,[20–22] with a PBE functional,[23] and a D3 dispersion correction with BJ-damping,[24] using the projector augmented wave method with an energy cut-off of 350 eV.[20,25] A Γ-centered (24×24×1) *k*-point mesh was sampled. The substrate was modelled by four layers of copper atoms, where the atomic positions in the bottom two layers were fixed during optimization. The unit cell contained one naphthalene or azulene molecule and 30 Å vacuum. The energetically most favorable adsorption site was found to be where the molecule is oriented along one of the close-packed directions with each ring above a hcp-hollow site, see figure 7.1.

7.3 Results and discussion

7.3.1 Adsorption height difference

Physisorbed molecules typically have a larger adsorption height than chemisorbed molecules. DFT calculations predict that naphthalene, having a weaker interaction with the Cu(111) surface, will have a higher adsorption height than azulene, specifically naphthalene has a predicted adsorption height of 2.81 Å, while for azulene the adsorption height is 2.33 Å according to DFT.

As shown by Schuler *et al.*, the minimum of a frequency shift-distance $\Delta f(z)$ curve contains information about adsorption height.[13] The position of the minimum in Δf is the height at which the Pauli repulsion starts to have a significant contribution to the

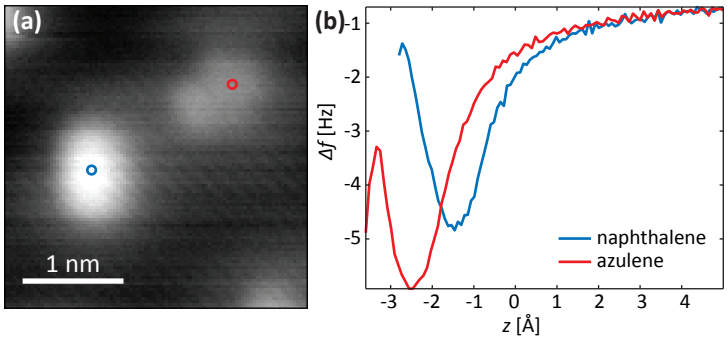

Figure 7.2 (a) STM image of a naphthalene and an azulene molecule on Cu(111), where the blue and red dots indicate the position of the $\Delta f(z)$ spectra in (b). STM settings: 10 pA at 100 mV. **(b)** $\Delta f(z)$ spectra over azulene and naphthalene molecules illustrating the difference in z_{min} is indicative of difference in adsorption height.

total energy. Logically; if two molecules have a different adsorption height we expect the minimum of the well in z (z_{min}) to occur a different tip-sample distances.

The inset of figure 7.2 shows an STM image of co-evaporated azulene and naphthalene molecules on Cu(111). The object with the larger apparent height (indicated by the blue dot) was identified from sub-molecular resolution AFM images to be naphthalene, while the molecule with lower apparent height (red dot) is azulene. $\Delta f(z)$ spectra above the molecules were acquired using the following procedure: first, the tip was positioned above the clean Cu(111) substrate with STM feedback parameters: 100 mV and 10 pA. This corresponds to z = 0 Å. After interrupting the feedback loop, the tip was positioned above the species of interest (taking into account the plane of the sample) and Δf was recorded as a function of tip-sample distance. This allows us to plot the spectra on the same, directly comparable, height scale on the x-axis, see figure 7.2. The z_{min} positions differ by 0.92±0.08 Å, with the azulene being closer to the surface. This difference is highly reproducible for different tip terminations and molecules. With this, we confirm the finding of Schuler *et al.*[13] that z_{min} can be used to determine relative adsorption heights. Additionally, from the reproducibility it can be concluded that single $\Delta f(z)$ spectra are sufficient to accurately determine an adsorption height difference between molecules. The adsorption height difference at the measured positions over the molecules according to DFT calculations

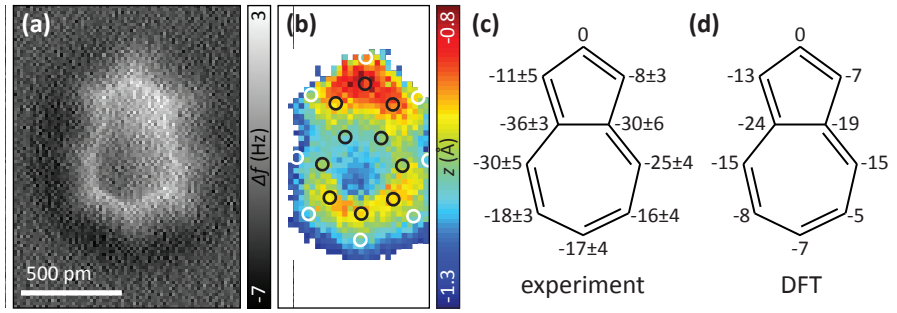

Figure 7.3 (a) Constant height AFM image of a single azulene molecule at -180 pm w.r.t. an STM set-point of 10 pA at 100 mV. **(b)** z_{min} map of azulene, overlaid with carbon (black) and hydrogen (white) atom positions. **(c)** Experimentally obtained z_{min} height of all C atoms with respect to the nose-C-atom of the 5-ring, in pm. **(d)** z_{min} heights of all C atoms with respect to the nose-C-atom calculated by DFT, in pm.

is 0.59 Å. We note here that accurately calculating adsorption heights of molecules on transition metal surfaces using DFT is difficult, especially for cases where van der Waals interactions are dominant. The experimental result presented here may provide a benchmark to test the performance of various functionals.

7.3.2 Azulene adsorption

After establishing that z_{min} can be used to determine relative adsorption heights of molecules, it is interesting to explore the accuracy and resolution on the sub-molecular scale. Figure 7.3(a) shows a constant height AFM image of azulene, where the 5- and 7-membered ring structure is clearly resolved. Figure 7.3(b) shows a z_{min} map of the molecule. Overall, the molecule has a distorted V-shape. The outermost C atom of the 5-ring is the highest point, while the 'tail' of the 7-ring is also higher than the region where the two rings are connected. This V-shaped conformation was also predicted by DFT, as can be seen from figure 7.1(e).

In figure 7.3(c-d) the experimental and DFT data is compared. The experimental values for the atom heights are found from averaging over 9 pixels closest to the atom position as indicated by the circles in figure 7.3(b). The apex of the 5-ring is indeed in both cases the highest point, and is thus set to 0 as the reference for the measured

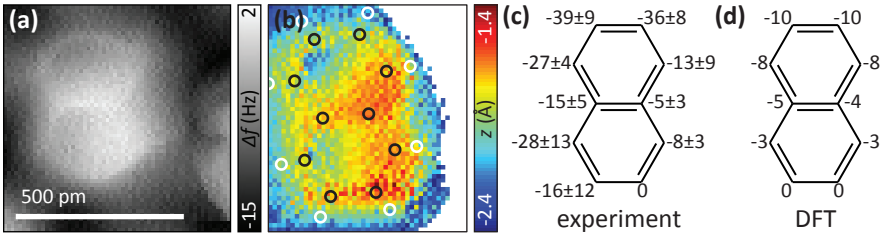

Figure 7.4 (a) Constant height AFM image of a naphthalene molecule in a self-assembly, at -300 pm w.r.t. an STM set-point of 10 pA at 100 mV. **(b)** z_{min} map of naphthalene, overlaid with carbon (black) and hydrogen (white) atom positions. **(c)** Experimentally obtained z_{min} height of all C atoms with respect to the bottom-right C-atom of the bottom ring, in pm. **(d)** z_{min} heights of all C atoms with respect to the bottom-right C-atom of the bottom ring calculated by DFT, in pm.

relative heights. Furthermore, the center bond is the lowest point, with the tail of the 7-ring protruding up again. Looking more closely at the numbers, it can be seen that both in experiment and theory one side of the molecule is still a bit lower than the other side, specifically the left side of the molecule is tilted downward. We tentatively ascribe the differences in the absolute numbers to a combination of different vdW forces in the center of the molecule and to inaccuracies in the DFT calculations. It is remarkable that the differences between experiment and simulation are on the order of a few pico-meters only. Hence, this method can be used to determine vertical relaxations within single molecules with an accuracy on the order of a few pico-meters.

7.3.3 Naphthalene adsorption

In the following, a similar set of results will be presented for naphthalene. Figure 7.4(a) shows a constant height AFM image of a naphthalene molecule that is part of a closely packed self-assembly of naphthalene molecules. The weak interaction with the surface caused naphthalene molecules to be too mobile to image isolated molecules without laterally moving them while imaging. The imaged naphthalene looks lob-sided; the right part of the rings seem more bright than the left side and is has a shadow extending to the right of the molecule. This can be caused by a mesoscopic tip asymmetry, or by a spatial variations in the bending of the probe particle.[26]

Figure 7.4(b) is the z_{min} map of the naphthalene molecule in (a). Again, the asymmetry is evident; the bottom right of both rings appear higher than the top left sides. Looking at the numerical values of the relative heights in figure 7.4(c-d) it is apparent that the entire molecule is adsorbed under an angle along its long axis. DFT calculations show the edge of the top ring to be 10 pm lower than the bottom edge, indicating a tilt of the molecular plane of 1.2° with respect to the Cu(111) surface. In the experimental data this angle is considerably larger: 3.5°.

The imperfect match between the DFT calculations and the experiment can be caused the previously mentioned tip asymmetry, additionally the DFT calculations were performed on an isolated naphthalene molecule, while it was not experimentally possible to obtain a zmin map on a molecule that was not in a self-assembled layer.

7.3.4 Azulene dipole

The dipole of azulene results in a smaller adsorption height than for its isomer naphthalene. The z_{min} maps show that the interaction with the surface is significant enough to change the shape of the molecule; it adsorbs in a V-shape. By adsorbing in a V-shape the bond angles around the two bridge C-atoms change, which affects the conjugated π-system. In addition, from UPS and XPS experiments it is known that the LUMO level of azulene hybridizes with states on the Cu surface, leading to charge transfer.[16] Both these factors could change the dipole of the molecule. KPFM is an AFM-based technique that can be used to measure the local contact potential difference (LCPD).[27] This quantity measures the potential that needs to be applied to minimize the electrostatic force between tip and sample. In regions of excess negative/positive charge, a larger/smaller positive voltage needs to be applied. From this, it can be understood that the LCPD signal can provide information about the dipole moment of molecules.[18] The KPFM maps presented here are obtained from finding the maximum (V^*) of $\Delta f(V)$ curves extracted from a set of constant height AFM images at increasing bias.[28]

The V* map is shown in figure 7.5. There is considerable contrast in this map. The LCPD in the region corresponding to the 5-ring is more positive than in the region of the 7-ring, indicating that the former has access negative charge. From the KPFM map

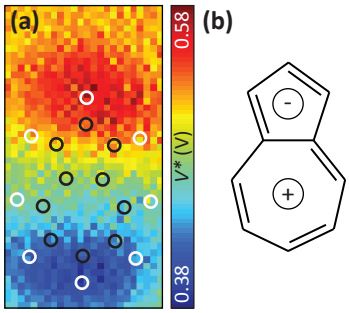

Figure 7.5 (a) KPFM map of a single azulene molecule, overlaid with carbon (black) and hydrogen (white) atom positions. **(b)** Model of azulene molecule indicating the direction of the dipole moment.

it is evident that the azulene molecule has retained a dipole moment upon adsorption. The direction is the same as in the gas-phase, the magnitude of the dipole can not be extracted from KPFM data.[10]

7.4 Conclusion

By measuring the vertical tip position as a function of Δf over all positions in the molecule, height differences within a molecule can be measured with pico-meter resolution, resulting in accurate representations of adsorption geometries in 3 dimensions. Not only molecular planes after adsorption can be measured, but z_{min} maps also reveal a difference in the 3D structure of azulene within the molecule: the V-shaped adsorption geometry could be clearly resolved. In addition we found that the dipole of azulene is still present after adsorption. AFM is therefore a technique that is uniquely suited to investigate the adsorption geometries of single molecules with sub-molecular resolution.

7.5 References

[1] E. I. Altman, M. Z. Baykara, U. D. Schwarz, Noncontact Atomic Force Microscopy: An Emerging Tool for Fundamental Catalysis Research. *Acc. Chem. Res.* **48**, 2640–2648 (2015).

[2] D. G. de Oteyza, P. Gorman, Y.-C. Chen, S. Wickenburg, A. Riss, D. J. Mowbray, G. Etkin, Z. Pedramrazi, H.-Z. Tsai, A. Rubio, M. F. Crommie, F. R. Fischer, Direct Imaging of Covalent Bond Structure in Single-Molecule Chemical Reactions. *Science.* **340**, 1434–1437 (2013).

[3] T. Sirtl, J. Jelic, J. Meyer, K. Das, W. M. Heckl, W. Moritz, J. Rundgren, M. Schmittel, K. Reuter, M. Lackinger, Adsorption structure determination of a large polyaromatic trithiolate on Cu(111): combination of LEED-I(V) and DFT-vdW. *Phys. Chem. Chem. Phys.* **15**, 11054 (2013).

[4] E. Goiri, M. Matena, A. El-Sayed, J. Lobo-Checa, P. Borghetti, C. Rogero, B. Detlefs, J.

Duvernay, J. E. Ortega, D. G. de Oteyza, Changes in adsorption heights upon self-assembly of bicomponent supramolecular networks, *arxiv.org/abs/1309.6440* (2013).

[5] L. Gross, F. Mohn, N. Moll, P. Liljeroth, G. Meyer, The Chemical Structure of a Molecule Resolved by Atomic Force Microscopy. *Science.* **325**, 1110–1114 (2009).

[6] K. O. Hanssen et al., A combined atomic force microscopy and computational approach for the structural elucidation of breitfussin A and B: Highly modified halogenated dipeptides from thuiaria breitfussi. *Angew. Chemie* **51**, 12238–12241 (2012).

[7] N. Pavliček, B. Fleury, M. Neu, J. Niedenfu, C. Herranz-lancho, M. Ruben, J. Repp, Atomic Force Microscopy Reveals Bistable Configurations of Dibenzo[a,h] thianthrene and their Interconversion Pathway. *Phys. Rev. Lett.* **108**, 86101 (2012).

[8] H. Mönig, D. R. Hermoso, O. Díaz Arado, M. Todorović, A. Timmer, S. Schüer, G. Langewisch, R. Pérez, H. Fuchs, Submolecular Imaging by Noncontact Atomic Force Microscopy with an Oxygen Atom Rigidly Connected to a Metallic Probe. *ACS Nano.* **10**, 1201–1209 (2016).

[9] L. Gross, F. Mohn, N. Moll, B. Schuler, A. Criado, E. Guitian, D. Pena, A. Gourdon, G. Meyer, Bond-Order Discrimination by Atomic Force Microscopy. *Science.* **337**, 1326–1329 (2012).

[10] B. Schuler, S. Liu, Y. Geng, S. Decurtins, Contrast formation in Kelvin probe force microscopy of single π-conjugated molecules. *Nano Lett.* **14**, 3342–6 (2014).

[11] N. Moll, B. Schuler, S. Kawai, F. Xu, L. Peng, A. Orita, J. Otera, A. Curioni, M. Neu, J. Repp, G. Meyer, L. Gross, Image Distortions of a Partially Fluorinated Hydrocarbon Molecule in Atomic Force Microscopy with Carbon Monoxide Terminated Tips. *Nano Lett.* **14**, 6127–6131 (2014).

[12] M. P. Boneschanscher, S. K. Hämäläinen, P. Liljeroth, I. Swart, Sample Corrugation Affects the Apparent Bond Lengths in Atomic Force Microscopy. *ACS Nano.* **8**, 3006–3014 (2014).

[13] B. Schuler, W. Liu, A. Tkatchenko, N. Moll, G. Meyer, A. Mistry, D. Fox, L. Gross, Adsorption Geometry Determination of Single Molecules by Atomic Force Microscopy. *Phys. Rev. Lett.* **111**, 106103 (2013).

[14] F. Albrecht, F. Bischoff, W. Auwärter, J. V Barth, J. Repp, Direct Identification and Determination of Conformational Response in Adsorbed Individual Nonplanar Molecular Species Using Noncontact Atomic Force Microscopy. *Nano Lett.* **16**, 7703–7709 (2016).

[15] A. G. Anderson, B. M. Steckler, Azulene. VIII. A Study of the Visible Absorption Spectra and Dipole Moments of Some 1- and 1,3-Substituted Azulenes 1,2. *J. Am. Chem. Soc.* **81**, 4941–4946 (1959).

[16] B. P. Klein, N. J. van der Heijden, C. K. Krug, M. Schöniger, P. Rosenow, M. Schmid, R. Tonner, I. Swart, J. M. Gottfried, Molecular Topology and Surface Chemical Bond: Alternate vs Non-Alternate Aromatic Molecules. *in preparation.*

[17] P. Hapala, M. Švec, O. Stetsovych, N. J. van der Heijden, M. Ondráček, J. van der Lit, P. Mutombo, I. Swart, P. Jelínek, Mapping the electrostatic force field of single molecules from high-resolution scanning probe images. *Nat. Commun.* **7**, 11560 (2016).

[18] F. Mohn, L. Gross, N. Moll, G. Meyer, Imaging the charge distribution within a single molecule. *Nat. Nanotechnol.* **7**, 227–231 (2012).

[19] L. Bartels, G. Meyer, K.-H. Rieder, Controlled vertical manipulation of single CO molecules with the scanning tunneling microscope: A route to chemical contrast. *Appl. Phys. Lett.* **71**, 213 (1997).

[20] G. Kresse, J. Furthmüller, Efficient iterative schemes for ab initio total-energy calculations using a plane-wave basis set. *Phys. Rev. B.* **54**, 11169–11186 (1996).

[21] D. Vanderbilt, Soft self-consistent pseudopotentials in a generalized eigenvalue formalism.

Phys. Rev. B. **41**, 7892–7895 (1990).
[22] S. Grimme, Density functional theory with London dispersion corrections. *Wiley Interdiscip. Rev. Comput. Mol. Sci.* **1**, 211–228 (2011).
[23] J. P. Perdew, K. Burke, M. Ernzerhof, Generalized Gradient Approximation Made Simple. *Phys. Rev. Lett.* **77**, 3865–3868 (1996).
[24] S. Grimme, J. Antony, S. Ehrlich, H. Krieg, A consistent and accurate ab initio parametrization of density functional dispersion correction (DFT-D) for the 94 elements H-Pu. *J. Chem. Phys.* **132**, 154104 (2010).
[25] P. E. Blöchl, Projector augmented-wave method. *Phys. Rev. B.* **50**, 17953–17979 (1994).
[26] Nadine J. van der Heijden, Prokop Hapala, Jeroen A. Rombouts, Joost van der Lit, Daniël Smith, Pingo Mutombo, Martin Švec, Pavel Jelinek, and Ingmar Swart, *ACS Nano.* **10**, 8517-8525 (2016)
[27] M. Nonnenmacher, M. P. O'Boyle, H. K. Wickramasinghe, Kelvin probe force microscopy. *Appl. Phys. Lett.* **58**, 2921 (1991).
[28] L. Gross, F. Mohn, P. Liljeroth, J. Repp, F. J. Giessibl, G. Meyer, Measuring the Charge State of an Adatom with Noncontact Atomic Force Microscopy. *Science.* **324**, 1428–1431 (2009).

A

Appendix

contents

Samenvatting in het Nederlands
Gearfetting yn it Frysk
List of presentations
List of publications
About the author
Acknowledgements

Samenvatting in het Nederlands

Het streven naar steeds kleinere elektronica, evenals de behoefte aan meer inzicht in de werking van katalysatoren voor energie-efficiënte fabrieken vereist een beter begrip van oppervlakken op de atomaire schaal. Met een atomaire-krachtmicroscoop (Engels: Atomic Force Microscope, AFM) kunnen oppervlakken en de moleculen die daarop liggen, vergroot worden afgebeeld. Hiermee kunnen de drijfveren van chemische reacties en elektrische eigenschappen van individuele moleculen en oppervlakken beter worden begrepen. Dit proefschrift beschrijft nieuwe inzichten in data interpretatie en verbreedt de blik op het type vragen dat beantwoord kan worden met AFM.

De titel van dit proefschrift "Opstapelen: Verkenning van de grenzen van ultra hoge resolutie atomaire kracht microscopie" verwijst naar de letterlijke stapels data die gebruikt zijn om de mogelijkheden van AFM te vergroten. In veel hoofdstukken in dit proefschrift is gebruik gemaakt van driedimensionale data die verkregen wordt door afbeeldingen letterlijk op elkaar te stapelen tot er een 3D blok ontstaat, waar meer informatie uit te halen is dan uit de individuele afbeeldingen.

Hoe werkt AFM?

De afbeelding wordt niet, zoals bij een foto of gewone microscoop, met licht gemaakt maar door een scherp naaldje over het oppervlak te scannen. De kracht tussen het naaldje en het oppervlak wordt gedetecteerd en afgebeeld.

Voor dit proefschrift werd de kracht tussen het oppervlak en de naald gemeten door een naaldje te bevestigen aan een kleine stemvork, zoals te zien is in afbeelding 2.4 op pagina 21. De stemvork is gemaakt van kwartsglas en heeft gouden electroden waarmee de beweging van de stemvork gemeten kan worden. De resonantie frequentie van de stemvork is ongeveer 25 kHz. Als de stemvork wordt aangeslagen beweegt de naald die eraan vast zit dus 25000 keer per seconde op en neer, met een uitwijking van 0.1 nm (1×10^{-10} m).

Als er een kracht is tussen de naald en het oppervlak verandert de frequentie van de trilling van de stemvork. Dit is te begrijpen met een gedachtenexperiment met

een magneet die aan een veer hangt. De magneet stelt de naald voor, en de veer is de stemvork. Als je de magneet naar beneden trekt en loslaat zal deze aan de veer hangend op en neer bewegen met een bepaalde frequentie. Je kunt nu deze op en neer bewegende magneet boven een magneet houden die op de grond ligt, zonder dat de magneten elkaar raken op het laagste punt. De tweede magneet stelt nu het oppervlak voor. De kracht tussen de twee magneten zal ervoor zorgen dat de frequentie van de oscillatie (trilling) van de bewegende magneet verandert. Als de magneet op de grond de bewegende magneet aantrekt zal deze langer beneden blijven; de frequentie van de oscillatie wordt dus iets lager. Andersom, als de magneet op de grond de bewegende magneet afstoot zal die korter laag blijven en dus zal de oscillatie frequentie omhoog gaan. Veranderingen in frequentie zijn zeer nauwkeurig te bepalen, zodat de krachten die gemeten kunnen worden met de meest geavanceerde moderne AFM's van de orde grootte van pico-Newtons (10^{-12} N) zijn. Ter vergelijking, dat is minder dan de kracht die je voelt onder het gewicht van één stuifmeel deeltje.

Wat kun je met AFM afbeeldingen?

Met de nauwkeurigheid waarmee krachten gemeten kunnen worden, samen met een ruimtelijke resolutie van pico-meters (10^{-12} m), is het mogelijk om met AFM moleculen af te beelden met atomaire resolutie. Plaatjes van moleculen gemaakt met AFM zien eruit zoals je ze uit een scheikundeboek kent: de atomen met de bindingen daartussen zijn goed te zien. Bekijk bijvoorbeeld afbeelding 2.8 op pagina 27 of een van de vele andere AFM plaatjes in dit proefschrift.

Bij nadere beschouwing van de AFM plaatjes is vaak te zien dat sommige delen van moleculen meer of minder oplichten dan de chemische structuur zou doen vermoeden, of dan de hexagonale ringen niet meer perfect hexagonaal zijn maar samengedrukt, uitgerekt of anders misvormd.

Vervormingen en contrast verschillen in afbeeldingen zijn vaak ongewenst, maar in dit proefschrift laat ik zien wat de oorzaak is van een aantal van deze artefacten (misvormingen) en hoe we ze juist kunnen gebruiken om meer informatie te verkrijgen.

Hoofdstuk 1 begint met een algemene introductie, daarna gaat hoofdstuk 2 in op de theorie en de huidige mogelijkheden van AFM toegepast op moleculen. Hoofdstuk 3 beschrijft hoe het door een vervorming lijkt alsof er een chemische binding bestaat tussen twee atomen waar die chemisch gezien niet is. Hoofdstuk 4 gebruikt de inzichten uit hoofdstuk 3 door uit de vervormingen in AFM plaatjes de elektrische ladingsverdeling te meten. Hoofdstuk 5 en 6 laten zien hoe je het verschil tussen chemische elementen zichtbaar kunt maken in AFM afbeeldingen door het stapelen van afbeeldingen. Tot slot laat hoofdstuk 7 zien dat het stapelen van afbeeldingen ook inzicht geeft in de geometrische structuur van moleculen op oppervlakken.

Gearfetting yn it Frysk

It stribjen nei hieltiid lytsere elektronika, lykas it ferlet fan ynsjoch yn de wurking fan katalisatoaren foar enerzjyeffisjinte fabriken fereasket in better begryp fan oerflakken op de atomêre skaal. Mei in atomêre krêftmikroskoop (Ingelsk: Atomic Force Microscope, AFM) kinne oerflakken en de molekulen dy't dêrop lizze, fergrutte ôfbylde wurde. Hjirmei kinne de driuwfearren fan gemyske reaksjes en elektryske eigenskippen fan yndividuele molekulen en oerflakken better begrepen wurde. Dit proefskrift beskriuwt nije ynsichten yn data ynterpretaasje en ferbredet de blik op it type fragen dat mei AFM beantwurde wurde kin.

De titel fan dit proefskrift "Opsteapelje: Ferkenning fan de grinzen fan ultra hege resolúsje atomêre krêft mikroskopy" ferwiist nei de letterlike steapels data dy't brûkt binne om de mooglikheden fan AFM te fergrutsjen. Yn de measte haadstikken fan dit proefskrift is gebrûk makke fan trijediminsjonale data dy't krigen wurdt troch it letterlik opinoar steapeljen fan ôfbyldings oant der in 3D blok ûntstiet, wêr't mear ynformaasje út te heljen is as út de yndividuele ôfbyldings.

Hoe wurket AFM?

De ôfbylding wurdt net lykas in gewoane foto mei ljocht makke mar troch it skennen fan it oerflak mei in skerpe nulle. De krêft tusken de nulle en it oerflak wurdt detektearre en ôfbylde.

Foar dit proefskrift waard de krêft tusken it oerflak en de nulle metten troch in nulle te befêstigjen oan in lytse stimfoarke, lykas te sjen is op ôfbylding 2.4 (side 21). De stimfoarke is makke fan kwartsglês en hat gouden elektroades wêrmei't de beweging fan de stimfoarke metten wurde kin. De resonânsjefrekwinsje fan de stimfoarke is likernôch 25 kHz. At de stimfoarke oanslein wurdt beweegt de nulle dy't deroan fêst sit dus 25.000 kear per sekonde op en del, mei in útwiking fan 0.1 nanometer (1×10^{-10} m).

At der in krêft is tusken de nulle en it oerflak feroaret de frekwinsje fan de trilling fan de stimfoarke. Dit is te begripen mei in tinzen-eksperimint mei in magneet dy't oan in fear hinget. De magneet stelt de nulle foar, de fear is de stimfoarke en de magneet sit

ûnderoan de fear fêst. Asto de magneet no nei ûnder lûkst en wer loslitst sil dizze op en del bewege mei in bepaalde frekwinsje. Do kinst no dizze op en del beweegjende magneet boppe in magneet hâlde dy't op de grûn leit, sûnder dat de magneten inoar reitsje op it leechste punt. De twadde magneet stelt no it oerflak foar. De krêft tusken de twa magneten sil derfoar soargje dat de frekwinsje fan de trilling fan de beweegjende magneet feroaret. At de magneet op de grûn de beweegjende magneet oanlûkt sil dizze langer ûnder bliuwe; de frekwinsje fan de trilling wurdt dus wat leger. Oarsom, at de magneet op de grûn de beweegjende magneet ôfstjit sil dy koarter leech bliuwe en dus sil de trillingsfrekwinsje omheech gean. Feroarings yn frekwinsje binne tige krekt te bepalen, sadat de krêften dy't metten wurde kinne mei de meast avansearre moderne AFM's yn de oardergrutte fan pico-Newtons (10^{-12} N) lizze. Ta fergelyk, dat is minder dan de krêft dy'tsto fielst ûnder it gewicht fan ien stomoalkerl.

Wat kinsto mei AFM ôfbyldings?

Mei de krektens wêrmei't krêften metten wurde kinne, tegearre mei in romtlike resolúsje fan pico-meters (10^{-12} m), is it mooglik om mei AFM molekulen ôf te byldzjen mei atomêre resolúsje. Plaatsjes fan molekulen makke mei AFM sjogge derút lykasto sy út in skiekundeboek kinst: de atomen mei de ferbinings dêrtusken binne goed te sjen. Sjoch bygelyks ôfbylding 2.8 (side 27), of ien fan de oare AFM plaatsjes yn dit proefskrift.

By neiere ynspeksje fan de AFM plaatsjes is faak te sjen dat guon parten fan molekulen mear of minder opljochtsje dan de gemyske struktuer tinken dwaan soe of dat de heksagonale ringen net mear perfekt heksagonaal binne mar yndrukt, útstrekt of oars ferfoarme binne.

Ferfoarmings en kontrastferskillen yn ôfbyldings binne faak net winske, mar yn dit proefskrift lit ik sjen wat de oarsaak is fan in oantal fan dizze artefakten (ferfoarmings) en hoe't wy har krekt brûke kinne om mear ynformaasje te krijen.

Haadstik 1 begjint mei in algemiene yntroduksje, dêrnei giet haadstik 2 yn op de teory en de hjoeddeiske mooglikheden fan AFM tapast op molekulen. Haadstik 3 beskriuwt hoe't it troch in ferfoarming liket as soe der in gemyske ferbining tusken twa atomen

wêze wêr't dy gemysk sjoen net is. Haadstik 4 brûkt de ynsichten út haadstik 3 troch út de ferfoarme AFM plaatsjes de elektryske ladingsdistribúsje te mjitten. Haadstik 5 en 6 litte sjen hoe'sto it ferskil tusken gemyske eleminten yn AFM ôfbyldings sichtber meitsje kinst troch it steapeljen fan ôfbyldings. Ta einbeslút lit haadstik 7 sjen dat it steapeljen fan ôfbyldings ek ynsjoch jout yn de geometryske struktuer fan molekulen op oerflakken.

List of presentations

Oct 2014	*Chemical identification of atoms in organic molecules with AFM* Dutch SPM Day, Delft (oral)
Jan 2015	*Chemical identification of atoms in organic molecules with AFM* Physics@FOM, Veldhoven (oral)
Feb 2015	*Towards Chemical identification of atoms in organic molecules* Workshop HR AFM/STM imaging, Prague, Czech Republic (oral)
Mar 2015	*Chemical identification of atoms in organic molecules with AFM* DPG-Frühjahrstagung, Berlin, Germany (oral)
Jun 2015	*Chemical identification of atoms in organic molecules using AFM* Utrecht Chemistry Day, Utrecht (poster)
Sep 2015	*Chemical identification of dopant atoms in graphene with AFM* nc-AFM, Cassis, France (poster)
Jan 2016	*The influence of the substrate on chemical identification of dopant atoms in graphene with AFM* Physics@FOM, Veldhoven (poster)
Mar 2016	*Sub-molecular contrast: Pauli vs Coulomb* DPG-Frühjahrstagung, Regensburg, Germany (oral)
Jul 2016	*Mapping the electrostatic force field of single molecules with AFM* nc-AFM, Nottingham, United Kingdom (poster, won second prize)
Oct 2016	*Mapping the electrostatic force field of single molecules from high-resolution scanning probe images* Dutch SPM Day, Nijmegen (oral)
Jan 2017	*Adsorption geometry of single molecules resolved with AFM* Physics@FOM, Veldhoven (oral)

List of publications

S.K. Hämäläinen, N.J. van der Heijden, J. van der Lit, S. den Hartog, P. Liljeroth, and I. Swart, Intermolecular contrast in atomic force microscopy images without intermolecular bonds, *Physical Review Letters* **113**, 186102 (2014)

J. van der Lit, J.L.Marsman, R.S. Koster, P.H. Jacobse, S.A. den Hartog, N.J. van der Heijden, D. Vanmaekelbergh, R.J.M. Klein Gebbink, L. Filion, I. Swart, Modelling the self-assembly of organic molecules on weakly interacting surfaces, *Journal of Physical Chemistry C* **17**, 052013 (2015)

P. Hapala, M. Švec, O. Stetsovych, N.J. van der Heijden, M. Ondráček, J. van der Lit, P. Mutombo, I. Swart, and P. Jelínek, Mapping the electrostatic force field of single molecules from high-resolution scanning probe images, *Nature Communications* **7**, 11560 (2016)

N.J. van der Heijden, D. Smith, G. Calogero, R.S. Koster, D. Vanmaekelbergh, M.A. van Huis, and I. Swart, Recognizing nitrogen dopant atoms in graphene using atomic force microscopy, *Physical Review B* **93**, 245430 (2016)

N.J. van der Heijden, P. Hapala, J.A. Rombouts, J. van der Lit, D. Smith, P. Mutombo, M. Švec, P. Jelínek, and I. Swart, Characteristic contrast in Δf_{min} maps of organic molecules using atomic force microscopy, *ACS Nano* **10**, 8517-8525 (2016)

About the author

Nadine Jacoba van der Heijden was born in Delft on the 9th of July in 1989. In 2007 she graduated from the St.-Bonifatius college in Utrecht and started her chemistry studies at Utrecht University. After obtaining her BSc in Chemical Sciences she followed it up by a MSc in Nanomaterials at Utrecht University. As part of this degree she spent four months as a research intern at City University of Hong Kong. Her master thesis titled "Diffusion behavior in superconducting Ti/Au bilayers for transition edge sensors to be applied in satellite detectors" she carried out at SRON Netherlands Institute for Space Research.

In 2013 Nadine started her PhD research at the Condesed Matter and Inferfaces group under the supervision of Ingmar Swart and Daniël Vanmaeklebergh. The main results of her work are described in this thesis, have been published in peer-reviewed journals and have been presented at (inter)national conferences. During her PhD she supervised a MSc student thesis project, and bachelor students for both practicum and theory courses.

Next to hiking and travelling, Nadine enjoys reading sci-fi classics and puzzle games.

Acknowledgements

Na vier jaar werken aan dit proefschrift, met mijn naam erop, ben ik me er ten zeerste van bewust dat het niet alleen mijn verdienste is. Hierbij wil ik alle mensen bedanken die hebben bijgedragen aan het tot stand komen van dit proefschrift: dankzij jullie hulp, steun, motivatie, ideeën, enthousiasme, en supervisie heb ik de afgelopen jaren met veel plezier gewerkt aan het wetenschappelijk onderzoek en het proefschrift dat nu voor je ligt.

Hierbij wil ik graag noemen: *Ingmar Swart*, mijn co-promotor bij wie ik binnen kon lopen voor de kleinste vragen en die ook vaak het lab opkwam, vol nieuwe ideeën. De keuze om mijn promotie op dit onderwerp te doen was niet alleen fantastisch door het onderwerp zelf, want hoge resolutie AFM is écht heel cool, maar zeker ook door de co-promotor die eraan vast zat. Ingmar, tige dank foar het luisteren, het advies, de uitleg en alles wat ik dankzij jou geleerd heb over mezelf, de wereld, en de wetenschap.

Mijn andere team kelder-genoten: *Joost van der Lit* voor de goede samenwerking, nuchtere blik, een repertoire aan efficiënt nieuw vakjargon, eerlijkheid, hulp bij het losdraaien van weerbarstige boutjes en moertjes (die jij waarschijnlijk zo strak had vastgedraaid), en bizarre muziek.

Marlou Slot voor geduldig luisteren en daarna een fantastische uitleg geven, dag en nacht klaar staan om helium te vullen, een meting te starten, of voor iets kleins op en neer te fietsen, en voor onze discussies en gesprekken over identiteit, leven en de maatschappij. Heel leuk dat jij mijn paranimf wilt zijn!

Saoirsé Freeney for being a great new addition to the team, I wish we could have spent some more time working together. Thanks for your (not) funny bicycle adventures and teaching me not say “have a nice meal” to anyone walking by around lunch time. *Daniël Smith* voor je werk aan stikstof gedoteerd grafeen en de levendigheid die jij meenam het lab op tijdens je masteronderzoek. *Peter Jacobse* voor je onverstoorbare team-kelder propaganda en wetenschappelijke bijdrage aan tekeningen op het whiteboard. *Jaco Geuchies* voor je aanhoudende belangstelling en betrouwbaarheid. *Daniël Vanmaekelbergh* voor je interesse en het delen van je ervaring.

Mijn kamergenoten *Mathijs de Jong* en *Joep Peters* voor de gesprekken over alles behalve wetenschap als ik afleiding nodig had en voor het me met rust laten als ik met een koptelefoon op naar m'n beeldscherm aan het staren was. De technici van onze vakgroep *Hans Ligthart* en *Peter van den Beld*, zonder jullie zouden we nooit kleine vertragingen door technische mankementen hebben, maar onoplosbare problemen die de wetenschap tot stilstand brengen.

My collegues over the years, for they made the CMI borrels and group outings a lot of fun: *Maryam Alimoradi Jazi*, *Anne Berends*, *Annelies van der Bok*, *Mark Boneschanscher*, *Annalisa Brodu*, *Sophia Buhbut-Sinai*, *Serena Busatto*, *Joren Eilers*, *Thomas Gardenier*, *Robin Geitenbeek*, *Elleke van Harten*, *Jacobine van Hest*, *John Kelly*. *Zachar Krumer*, *Linda Kumeling*, *Andries Meijerink*, *Celso de Mello Donegá*, *Federico Montanarella*, *Carlo van Overbeek*, *Christa van Oversteeg*, *Francesca Pietra*, *Christiaan Post*, *Tim Prins*, *Freddy Rabouw*, *Tim Senden*, *Kelly Sowers*, *Ward van der Stam*, *Pedro Villanueva-Delgado*, *Winston Wang*, *Harold de Wijn*, *Weiwei Wu*, *Chenghui Xia*, *Allan Xu*, *Wenjin Xu*, *Ting Yu*, and *Stephan Zevenhuizen*.

My co-authors and collaborators for their help, input and fruitful colaborations: *Gaetano Calogero*, *Michael Gottfried*, *Sampsa Hämaläinen*, *Prokop Hapala*, *Stephan den Hartog*, *Marijn van Huis*, *Pavel Jelínek*, *Florian Klappenberger*, *Benedikt Klein*, *Rik Koster*, *Peter Liljeroth*, *Pingo Mutombo*, *Martin Ondráček*, *Mateusz Paszkiewicz*, *Jeroen Rombouts*, *Oleksandr Stetsovych*, and *Martin Švec*.

Buiten de wetenschap, maar zeker niet op de achtergrond: *Annika* voor je vriendschap en steun, voor je luisterend oor en verhelderende frisse blik op mijn cirkel-gedachten.

Andere vrienden en mijn familie voor advies en steun en voor het aanhoren van telkens dezelfde uitleg over AFM en altijd geïnteresseerd overkomen en meegaan in mijn enthousiasme: *Anne*, *Sara*, *Hedwich*, *Robert*, *Maarten*, *Zonne*, *Sander*, *Arne*, *Johan*, *Gruson*, *Eva*, *Jan-Peke*, *Bernardine*, *Marike*, *Koen*, *Bram*, *Jip*, *Luuk*, *Reinder*, *Marjolein*, *Ettje*, *Eibert*, *Nynke*, mijn ooms, tantes, neven en nichten, (achter)neefjes en (achter) nichtjes en muoikesizzers.

Heit en *mem* foar jimme stipe en it altyd waarme ûnthaal. Tige dank foar it oanskerpje fan myn harsens mei boerdspultsjes en wiskundige patroanen om te breidzje.

Papa voor het opwekken van mijn nieuwsgierigheid voor hoe de wereld precies werkt nog voordat ik goed kon lopen. Jouw vele achterkant-van-envelop-lessen over speciale relativiteit, goniometrie en vele andere onderwerpen hebben mijn interesse mijn hele leven lang aangewakkerd. Bedankt ook voor de gesprekken uit mijn volwassenjaren en de daaruit voortvloeiende inzichten over werk en leven.

Mama voor altijd in mijn ongebreidelde mogelijkheden geloven en mij niet alleen toestaan, maar aan te moedigen om de hoogste bomen en klimrekken te beklimmen. Samen hebben we veel pieken en dalen van de Alpen en in ons leven bewandelt, met jou voor altijd in mijn team voel ik me sterk. Bedankt voor het lezen van al mijn wetenschappelijke schrijfsels en vaak ook mijn gedachtepatronen, en je advies over beiden.

Jelmer voor alle pyjamadagen, kietels en het om-dinoën. Tige dank foar het luisteren naar mijn twijfels en het uitdagen van mijn overtuigingen. Bestest.